

Biophysical investigations of different DNA origami nanostructures in various molecular and ionic environments

Dissertation zur Erlangung des akademischen Grades

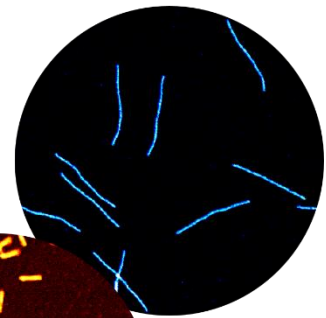
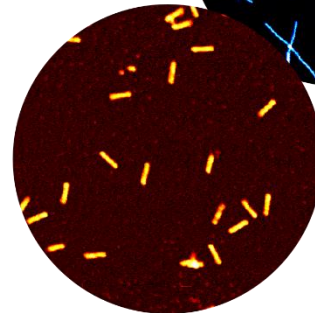
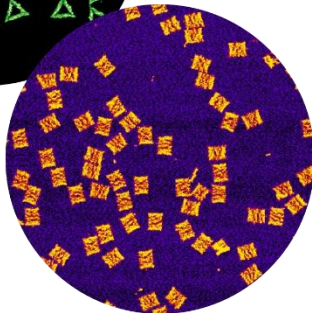
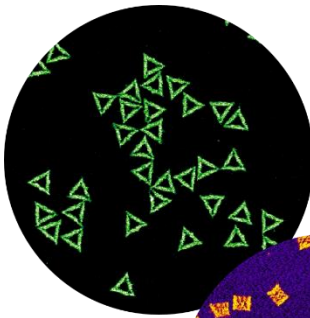
Dr. rer. Nat.

eingereicht an der Universität Paderborn in der Fakultät für Naturwissenschaften

von

Marcel Hanke

geboren am 23.03.1993 in Detmold.



Erstgutachter: PD Dr. Adrian Keller

Zweitgutachter: Assoz. Prof. Dr. Veikko Linko

Drittgutachter: Prof. Dr. Guido Grundmeier

Datum der Promotionsprüfung: 12.12.2023

Abstract

DNA origami as a bottom-up concept for DNA nanostructure assembly of well-defined arbitrary nanostructures through a one pot reaction with high simplicity, relatively short reaction times, and feasibility of high yields provides a high application potential in numerous fields, e.g., biomedicine, biosensing, biophysics, nanoelectronics, and nanopatterning. However, structural stability, integrity, and functionality of DNA origami nanostructures under various molecular and ionic conditions are required in many application aspects. Studies of DNA origami nanostructure stability in presence of chaotropic agents and their interaction, for instance, are not sufficiently understood, yet. Therefore, the first part of this work addresses the role of chaotropic agents, i.e., guanidinium- (Gdm) and tetrapropylammonium (TPA) salts, in DNA origami nanostructure stability. This part of the work tremendously illustrated the complexity of DNA origami nanostructures interaction under different chaotropic conditions. It could be shown that various factors, i.e., incubation temperature, and time, as well as the type of chaotropic agent, its counterions, and the DNA origami design itself have an interdependent effect on the stability of DNA origami nanostructures. Furthermore, besides chemical interaction between DNA origami nanostructures and chaotropic denaturants, the next part of this work addresses the effect of the ionic strength on the thermal stability of different DNA origami nanostructures. It is known that the structural stability of DNA origami nanostructures is modulated by the presence of the cationic species, in particular by the divalent cation Mg^{2+} , but also by its present concentration. Therefore, the melting temperature of different DNA origami nanostructure designs were experimentally investigated under different Mg^{2+} concentrations by fluorimetry and compared with calculated melting temperature values. The results revealed substantial deviations of the measured melting temperatures of different DNA origami nanostructures compared to the calculated melting temperature values. The measured melting temperatures of the different DNA origami nanostructures saturates at high ionic concentrations and thus become independent of the ionic strength suggesting that the thermal stability of DNA origami at high ionic strength is limited by mechanical strain other than by inter-helix repulsion.

The final part of this work addresses the visualization of efficient drug loading of single DNA origami nanostructures. Conventional methods for drug loading detection as UV/VIS spectroscopy or fluorescence spectroscopy might under- or overestimate the efficient drug

loading of complex nanostructures as DNA origami. In this work, the efficient drug loading of single DNA origami nanostructures with the minor groove-binder methylene blue (MB) was visualized by AFM-IR nanospectroscopy for the first time. IR spectra of the gold surface with drug-loaded DNA origami triangles with different MB concentration could be obtained with IR peaks that correlate with MB concentration. In addition, IR imaging at 1650 cm^{-1} resolved MB-loaded DNA origami triangles. Moreover, IR imaging at 1650 cm^{-1} of three different DNA origami nanostructure designs, i.e., 2D Rothemund triangle, 6HB (42-bpCS), and 24HB revealed a shape dependence in IR signal. These results demonstrate that AFM-IR nanospectroscopy might become a new versatile tool for qualitative as well as quantitative drug loading detection in DNA origami applications.

List of Abbreviations

6HB	six-helix bundles
6HB 21-bpCS	six-helix bundles with 21 base pairs per crossover spacings
6HB 42-bpCS	six-helix bundles with 42 base pairs per crossover spacings
24HB	24-helix bundles
A	adenine
bp	base pair
C	cytosine
CD	circular dichroism
Cl⁻	chloride
ds	double stranded
dsDNA	double-stranded DNA
G	guanine
T	thymine
AFM	atomic force microscopy
AFM-IR	atomic force microscopy infrared spectroscopy
DNA	deoxyribonucleic acid
EDTA	ethylenediaminetetraacetic acid
FRET	Förster resonance electron transfer
Gdm	guanidinium
GdmCl	guanidinium chloride
GdmSCN	guanidinium thiocyanate
Gdm₂SO₄	guanidinium sulfate
IR	infrared spectroscopy
ITTFA	iterative target test factor analysis
MB	methylene blue
MD	molecular dynamics
Mg²⁺	magnesium
MgAc₂	magnesium acetate

MgCl₂	magnesium chloride
Na⁺	sodium
NADH	nicotinamide adenine dinucleotide
nt	nucleotide(s)
PCA	principle component analysis
PFIR	peak-force tapping IR
RI	relative integrity
SCN	thiocyanate
SO₄²⁻	sulfate
ssDNA	single-stranded DNA
<i>T_m</i>	melting temperature
TAE	tris-acetate-EDTA
TPA	tetrapropylammonium
TPACl	tetrapropylammonium chloride
Tris	2-Amino-2-(hydroxymethyl)propane-1,3-diol

List of Publications

Elements of this thesis have been published in following articles:

- I. **M. Hanke**, D. Dornbusch, E. Tomm, G. Grundmeier, K. Fahmy and A. Keller, Superstructure-dependent stability of DNA origami nanostructures in the presence of chaotropic denaturants, *Nanoscale*, 2023, **15**, 16590-16600.
- II. **M. Hanke**, E. Tomm, G. Grundmeier and A. Keller, Effect of Ionic Strength on the Thermal Stability of DNA Origami Nanostructures, *Chembiochem : a European journal of chemical biology*, 2023, **24**, e202300338.
- III. **M. Hanke**, N. Hansen, E. Tomm, G. Grundmeier and A. Keller, Time-Dependent DNA Origami Denaturation by Guanidinium Chloride, Guanidinium Sulfate, and Guanidinium Thiocyanate, *Int. J. Mol. Sci.*, 2022, **23**, 8547.
- IV. **M. Hanke**, G. Grundmeier and A. Keller, Direct visualization of the drug loading of single DNA origami nanostructures by AFM-IR nanospectroscopy, *Nanoscale*, 2022, **14**, 11552–11560.
- V. **M. Hanke**, D. Dornbusch, C. Hadlich, A. Rossberg, N. Hansen, G. Grundmeier, S. Tsushima, A. Keller and K. Fahmy, Anion-specific structure and stability of guanidinium-bound DNA origami, *Comput. Struct. Biotechnol. J.*, 2022, **20**, 2611–2623.

Other publications:

- VI. **M. Hanke**, N. Hansen, R. Chen, G. Grundmeier, K. Fahmy and A. Keller, Salting-Out of DNA Origami Nanostructures by Ammonium Sulfate, *Int. J. Mol. Sci.*, 2022, **23**, 2817.
- VII. D. Hense, A. Büngeler, F. Kollmann, **M. Hanke**, A. Orive, A. Keller, G. Grundmeier, K. Huber and O. I. Strube, Self-Assembled Fibrinogen Hydro- and Aerogels with Fibrin-like 3D Structures, *Biomacromolecules*, 2021, **22**, 4084–4094.
- VIII. **M. Hanke**, Y. Yang, Y. Ji, G. Grundmeier and A. Keller, Nanoscale Surface Topography Modulates hIAPP Aggregation Pathways at Solid-Liquid Interfaces, *Int. J. Mol. Sci.*, 2021, **22**, 5142.

- IX. **M. Hanke**, A. Gonzalez Orive, G. Grundmeier and A. Keller, Effect of DNA Origami Nanostructures on hIAPP Aggregation, *Nanomaterials*, 2020, **10**, 2200.
- X. R. Hajiraissi, **M. Hanke**, A. Gonzalez Orive, B. Duderija, U. Hofmann, Y. Zhang, G. Grundmeier and A. Keller, Effect of Terminal Modifications on the Adsorption and Assembly of hIAPP(20-29), *ACS Omega*, 2019, **4**, 2649–2660.
- XI. K. Brassat, S. Ramakrishnan, J. Bürger, **M. Hanke**, M. Doostdar, J. K. N. Lindner, G. Grundmeier and A. Keller, On the Adsorption of DNA Origami Nanostructures in Nanohole Arrays, *Langmuir*, 2018, **34**, 14757–14765.
- XII. R. Hajiraissi, **M. Hanke**, Y. Yang, B. Duderija, A. Gonzalez Orive, G. Grundmeier and A. Keller, Adsorption and Fibrillization of Islet Amyloid Polypeptide at Self-Assembled Monolayers Studied by QCM-D, AFM, and PM-IRRAS, *Langmuir*, 2018, **34**, 3517–3524.

Contents

Abstract	1
List of Abbreviations	3
List of Publications	5
1 Introduction	11
2 Fundamentals	14
2.1 Deoxyribonucleic acid (DNA)	14
2.2 DNA origami	16
2.3 DNA origami stability	18
2.4 Chaotropic salts	19
2.5 Drug loading of DNA origami	22
3 Methods	24
3.1 Atomic force microscopy (AFM)	24
3.2 Atomic force microscopy infrared spectroscopy (AFM-IR)	26
3.3 Fluorescence spectroscopy	30
4 Biophysical stability studies of DNA origami nanostructures under various chaotropic conditions	33
4.1 Anion-specific structure and stability of guanidinium-bound DNA origami	33
4.1.1 Introduction	33
4.1.2 Results and discussion	35
4.1.2.1 AFM imaging	35
4.1.2.2 Discussion	42
4.1.2.3 Conclusion	43

4.1.3	Materials and methods	43
4.1.3.1	DNA origami synthesis	43
4.1.3.2	AFM imaging and analysis	44
4.2	Time-Dependent DNA Origami Denaturation by Guanidinium Chloride, Guanidinium Sulfate, and Guanidinium Thiocyanate	45
4.2.1	Introduction	45
4.2.2	Results	46
4.2.2.1	Guanidinium Chloride (GdmCl)	46
4.2.2.2	Guanidinium Sulfate (Gdm ₂ SO ₄).....	49
4.2.2.3	Guanidinium Thiocyanate (GdmSCN).....	52
4.2.2.4	Discussion	54
4.2.3	Materials and methods	57
4.2.3.1	DNA Origami Synthesis and Purification	57
4.2.3.2	Guanidinium Exposure.....	57
4.2.3.3	AFM Imaging.....	58
4.2.3.4	Quantification and Statistical Analysis	58
4.3	Superstructure-dependent stability of DNA origami nanostructures in the presence of chaotropic denaturants.....	59
4.3.1	Introduction	59
4.3.2	Results and discussion.....	61
4.3.2.1	Gdm ₂ SO ₄	61
4.3.2.2	GdmCl.....	66
4.3.2.3	TPACl.....	69
4.3.2.4	Quantitative comparison	70
4.3.3	Conclusion.....	72

4.3.4	Materials and Methods	74
4.3.4.1	DNA origami assembly	74
4.3.4.2	Sample preparation and AFM imaging	75
4.3.4.3	AFM image analysis.....	75
5	Effect of Ionic Strength on the Thermal Stability of DNA Origami Nanostructures	77
5.1	Introduction.....	77
5.2	Results and discussion	78
5.3	Conclusion	91
5.4	Materials and Methods.....	92
5.4.1	Calculation of staple melting temperatures	92
5.4.2	DNA origami assembly	92
5.4.3	Melting curve measurements and analyses	93
5.4.4	AFM imaging	93
6	Direct visualization of the drug loading of single DNA origami nanostructures by AFM-IR nanospectroscopy.....	95
6.1	Introduction.....	95
6.2	Results and discussion	96
6.3	Conclusion	105
6.4	Materials and Methods.....	106
6.4.1	DNA origami assembly and MB loading	106
6.4.2	DNA origami immobilization on template-stripped gold substrates.....	107
6.4.3	AFM-IR nanospectroscopy	107
7	Conclusion.....	108
8	References	111

Declaration of Authorship	133
Acknowledgement	134

1 Introduction

Deoxyribonucleic acid (DNA) as the carrier of genetic information in organisms exhibits one of the most unique structural properties and intermolecular interactions in nature. The native structure of double-stranded DNA (dsDNA) as a double helix is being composed of a phosphate backbone linked with a deoxyribose sugar unit and one of the four nucleobases, i.e., adenine (A), guanine (G), cytosine (C), and thymine (T) that complementary interact via so-called Watson-Crick base pairing.¹ The breakthrough in the structural revelation and the understanding of how native dsDNA is formed occurred in the 50s.²

About 30 years later, this inherent unique sequence dependence in dsDNA formation was exploited by Seeman³ in order to construct immobile junctions for controlled 2D DNA nanostructure formation via Watson-Crick base pairing.³ The biggest step forward in DNA nanotechnology was made by Rothemund⁴ in 2006 with DNA origami as a bottom-up concept for DNA nanostructure assembly. Therefore, a long viral ssDNA scaffold of about 7,000 nucleotides (nt) is folded by 200-250 short complementary oligonucleotides, called staple strands, in 100-fold excess into well-defined arbitrary nanostructures through a one pot reaction with high simplicity, relatively short reaction times, and feasibility of high yields.⁴ Nowadays, the applications with DNA origami nanostructures tremendously increased in numerous fields as in biomedicine and biosensing,^{5,6} biophysics,⁷ nanoelectronics,⁸ and nanopatterning.⁹

At the same time, the need of detailed understanding about intra- and intermolecular interactions of DNA origami nanostructures in different molecular and ionic environments is the key factor in order to effectively address these application fields with high and reliable functionality.^{5,10-12} In general, the intramolecular interaction of DNA origami must be considered as one of the essential aspects for assembly and stability since cationic presence, in particular of divalent Mg^{2+} , in solution is required to screen the high negatively charged backbone of the DNA and thus overcome the repulsive interaction of helices.^{10,13,14} In biophysiological conditions, however, also intermolecular interactions of DNA origami nanostructures with several molecular species as (enzymatic) proteins, chao- and kosmotropes or therapeutics but also different physiological ionic conditions with low Mg^{2+} concentrations need to be considered with regard to the overall DNA origami structural stability, integrity, and functionality.^{10,11} In this regard, studies have been already published addressing the stability

issue of DNA origami nanostructures under various conditions. It is known, that DNA origami nanostructures inherently possess reasonable stability properties under different chemical environments,¹⁵ buffer conditions,¹⁶ and by ionizing radiation.¹⁷ Under cryogenic temperatures, DNA origami nanostructures revealed high longevity properties.^{18,19} They are also reasonably unaffected of harsh thermal conditions when adsorbed on the surface.^{15,20} On the other hand, the stability of DNA origami nanostructures has significant deficits at low cation concentrations,^{21,22} especially of the divalent cation Mg^{2+} , in the presence of nucleases,^{23,24} and at chaotropic conditions.^{25,26} The latter, initial stability studies on DNA origami nanostructure in presence of chaotropic salts, i.e., guanidinium chloride (GdmCl) or urea, have demonstrated strong salt and cation concentration- as well as temperature-dependent denaturation effects with significant impact on their melting temperature and the structural integrity.^{25,26}

Since studies of DNA origami nanostructure stability in presence of chaotropic agents are not sufficiently understood, the first part of this work addresses the role of chaotropic agents, here guanidinium- (Gdm) and tetrapropylammonium- (TPA) salts, in DNA origami nanostructure stability.

First, the stability of DNA origami triangles in two different Gdm-salts, i.e., GdmCl and guanidinium sulfate (Gdm_2SO_4), at different temperature and concentration conditions has been investigated. Moreover, the Gdm-salt variety was further extended with guanidinium thiocyanate (GdmSCN) and time dependent stability investigations on DNA origami triangles at different temperatures were performed. Finally, the stability of six different DNA origami designs, i.e., the 2D Rothemund triangle,⁴ the “tall” rectangle,⁴ a Z shape,²⁷ two six-helix bundles (6HBs) with different crossover spacings of 42 (42-bpCS) and 21 bp (21-bpCS),²⁴ and a 24-helix bundle²⁸ (24HB) in three different types to chaotropic salts, i.e., GdmCl and guanidinium sulfate (Gdm_2SO_4) as well as tetrapropylammonium chloride (TPACl) have been investigated. This part of the work tremendously illustrated the complexity of DNA origami nanostructures interaction under different chaotropic conditions. It has been shown that various factors, i.e., incubation temperature, and time, as well as the type of chaotropic agent, its counterions, and the DNA origami design itself have an interdependent effect on the stability of DNA origami nanostructures.

Furthermore, besides chemical interaction between DNA origami nanostructures and chaotropic denaturants, next part of this work addresses the effect of ionic strength on the thermal stability of different DNA origami nanostructures. Since it is known that ionic

environment plays a crucial role in the structural stability in DNA origami, especially by the modulation of the Mg^{2+} -concentration,¹⁰ the melting temperature of five different DNA origami nanostructure designs, i.e., the 2D “tall” rectangle,⁴ the 2D Rothmund triangle,⁴ 6HB 42-bpCS and 21-bpCS,²⁴ and 24HB,²⁸ were experimentally investigated under different Mg^{2+} concentrations by fluorimetry and compared with calculated melting temperature values. The results surprisingly revealed substantial deviations of the measured melting temperatures of different DNA origami compared to the calculated melting temperature values. Even more intriguing, the measured melting temperatures of the different DNA origami saturate at high ionic concentrations and thus become independent of the ionic strength. These observations suggest that the thermal stability of DNA origami at high ionic strength is limited by mechanical strain other than by inter-helix repulsion.

Finally, the work addresses the visualization of efficient drug loading of single DNA origami nanostructures. Typical methods for drug loading detection are UV/VIS spectroscopy or fluorescence spectroscopy, for instance. However, these methods might under- or overestimate the efficient drug loading, in particular of complex nanostructures as DNA origami but it can also be caused due to the pH and the ionic strength of the solution or the drug concentration.²⁸ In this work, the efficient drug loading of single DNA origami nanostructures with the minor groove-binder methylene blue (MB) was visualized by AFM-IR nanospectroscopy for the first time. The results of IR spectra of the gold surface with drug-loaded DNA origami triangles with different MB concentration revealed IR peaks that correlate with MB concentration. In addition, performing IR imaging at 1650 cm^{-1} resolved MB-loaded DNA origami triangles. Applying simultaneously three different DNA origami nanostructure designs, i.e., 2D Rothmund triangle,⁴ 6HB (42-bpCS),²⁹ and 24HB²⁸ for IR imaging at 1650 cm^{-1} revealed a shape dependence in IR signal, showing the highest signal intensity for the thickest DNA origami nanostructure, i.e., 24HB. Thus, AFM-IR nanospectroscopy might become a new versatile tool for qualitative as well as quantitative drug loading detection in DNA origami applications.

2 Fundamentals

2.1 Deoxyribonucleic acid (DNA)

Deoxyribonucleic acid (DNA) is the carrier and storage of all genetic information that is essential for the formation of cells and tissues in an organism. The primary structure of DNA is a linear polymer that is built up of nucleotides (nt). The chemical structure of a nucleotide can be separated into three parts, i.e., an organic base that is linked to a five-carbonated sugar, called deoxyribose, on carbon 1 position and a phosphate group linked to carbon 5 position (see Figure 2.1). DNA consists of four different, that differ in the structure of the organic base. In general, the organic bases are derivatives of purine, called adenine (A) and guanine (G), and pyrimidine, called cytosine (C) and thymine (T). The nucleotides are linked via phosphodiester bonds forming the backbone of a nucleic acid strand of the DNA. Thus, a single-stranded DNA (ssDNA) consists of a phosphate group at 5' end and a hydroxyl group at 3' end of its terminal sugar.¹ Following this order and by convention, a polynucleotide sequence is usually written and read in the 5'→3' direction.³⁰ The backbone of the polynucleotides shows high conformational flexibility properties due to their rotatable bonds and is negatively charged at neutral pH because of the phosphate groups. Due to the affinity of planar stacking of the nucleic bases, they preferentially look away from the backbone.¹

Native DNA has a right-handed double-helical structure that was first correctly proposed by Watson and Crick² in 1953. The double helix is formed by two antiparallel oriented polynucleotides strands having their hydrophilic backbone on the outside while the hydrophobic bases are on the inside of the structure and form so called Watson-Crick base pairs³¹ in a complementary order, i.e., A interacts with T via two hydrogen bonds and G interacts with C via three hydrogen bonds (see Figure 2.1). The aromatic character of the base pairs (bp) leads to hydrophobic and van der Waals interaction that contribute to the stabilization of the double helix of a DNA.³⁰

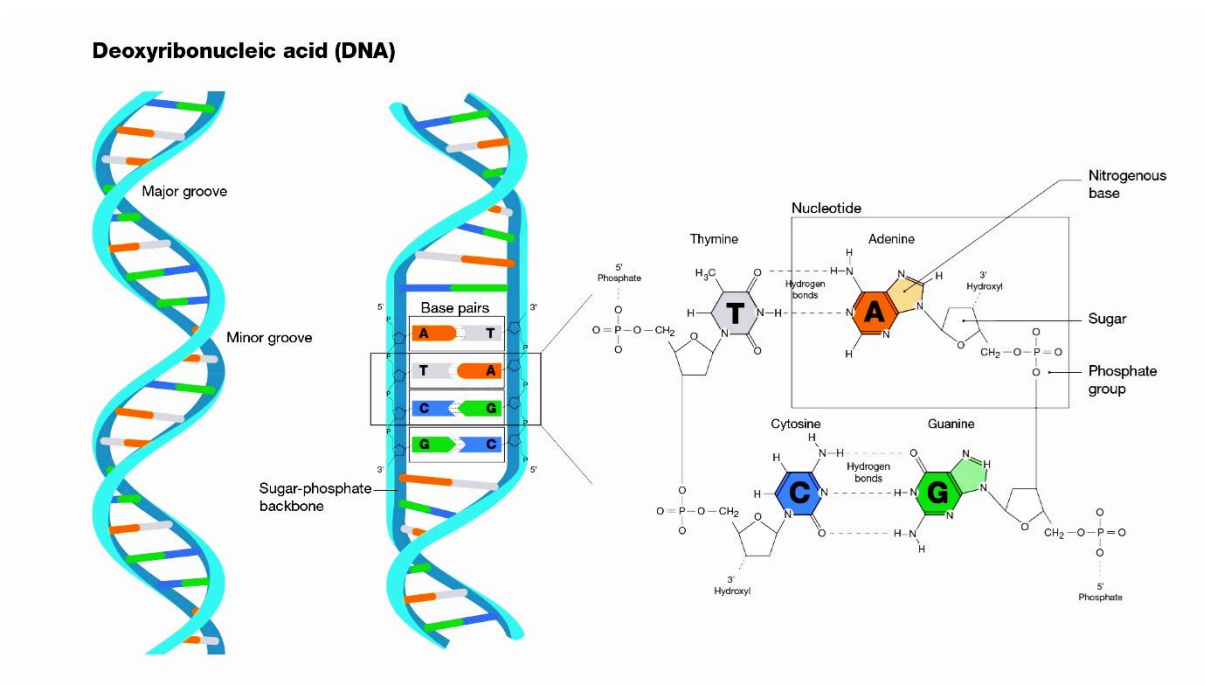


Figure 2.1 Schematic representation of a right-handed dsDNA structure illustrating minor and major grooves as well as Watson-Crick base pairing on the left panel. Chemical structure of the nucleotides and the nucleobases, i.e., adenine (A), guanine (G), cytosine (C) and thymine (T), and their specific interaction via hydrogen bonding are depicted on the right panel. Reprinted from public domain Courtesy: National Human Genome Research Institute (<https://www.genome.gov/genetics-glossary/Deoxyribonucleic-Acid>).

The elegant natural way of the double-stranded DNA (dsDNA) to minimize its energy by forming a double helix leads to some specific properties in the chemical structure as well as in the geometry depending on the environment. In solution, the most common structure of the DNA is the right-handed helical so-called B-form having a space of 0.34 nm between the stacked bases with about 10.5 pairs per turn and a diameter of 1.9 nm. Furthermore, due to the asymmetrical arrangement in binding between the bases and the sugar in the nucleotides, the DNA double helix structure is consequently asymmetrical. This leads to an alternating arrangement of major grooves and minor grooves in the helix that are important in DNA-protein interactions and DNA drug loading (see chapter 2.5 for more details).¹ DNA, as a double helix, remains its high flexibility properties that are inherently necessary to overcome several natural challenges, like compact packaging of long double strands in cellular structures and still being able to serve as a genetic encode. Therefore, dsDNA is very adjustable in its conformation that results in many different structures.³² The A-form DNA, for instance, is a transition of the B-

form DNA that is more favorable in low water environment. The leakage of water molecule leads to a stiffer and contracted double helix with an increased diameter of 2.3 nm and having 11 base pairs per turn.^{1,32} Besides right-handed double helix DNA, also left-handed double helixes DNA exists, as for example the Z-form DNA.^{32,33}

2.2 DNA origami

The unique molecular structure of the DNA with its specific intermolecular interactions that are based on the Watson-Crick base pairing provides a fascinating approach to fabricate well-defined nanostructures with numerous potential growth in applications evolved within a timeline of around the last 4 decades.³⁴

In year 1982, Seeman³ published his idea of an immobile junction construction that enabled the formation of a 2D DNA nanostructure via Watson-Crick base pairing with an algorithm of non-repeatable base sequence segments within one branched junction (see Figure 2.2 a)). Modifying the junctions with complementary sticky ends led to the assembly of bigger branched networks (see Figure 2.2 b)).³

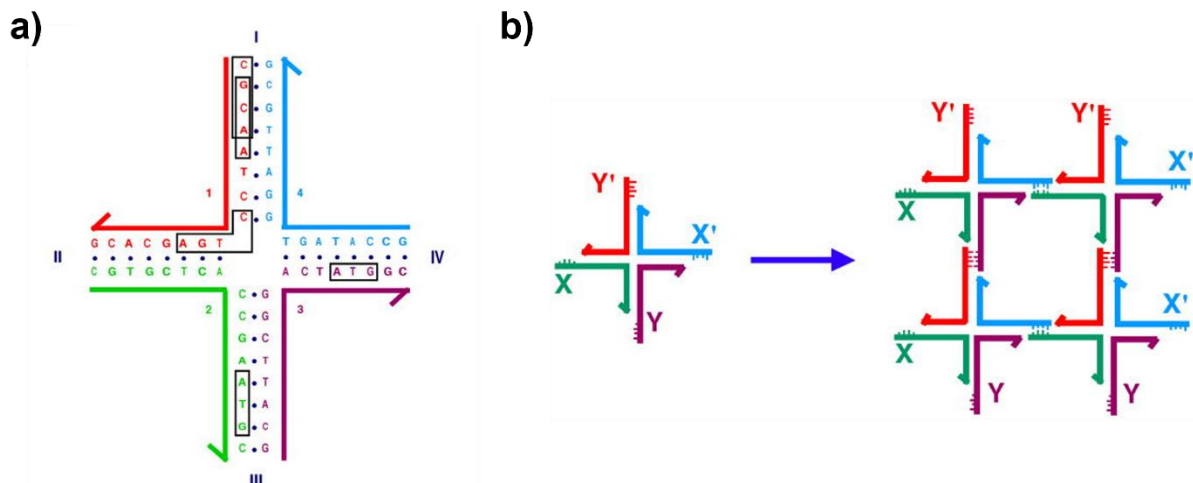


Figure 2.2 a) Structure of a branched tetrameric junction consisting of four individual segments with no symmetric sequence units at each branched corner. b) Schematic illustration of branched network assembly from tetrameric junction units. Each segment of one branched tetrameric junction exhibits a sticky end with a configuration of X – X' and Y – Y' that are complementary to each other resulting in a growing lattice network. a) and b) adapted with permission.³⁵ Copyright © 2005 IOP Publishing Ltd. Permission conveyed through Copyright Clearance Center, Inc.

The era of DNA nanotechnology was born and evolved in terms of complexity and stability by creating 2D and 3D robust motifs within the next approx. 25 years.³⁴ However, the biggest breakthrough in DNA nanotechnology was achieved by Rothemund⁴ in 2006 with the bottom-up concept of DNA origami assembly. His idea represents the folding of a long viral ssDNA scaffold of about 7,000 nt by 200-250 short complementary oligonucleotides, called staple strands, in 100-fold excess into well-defined arbitrary nanostructures through a one pot reaction (see Figure 2.3). The simplicity of the reaction and the feasibility of high yields in relatively short time makes this approach very attractive.⁴

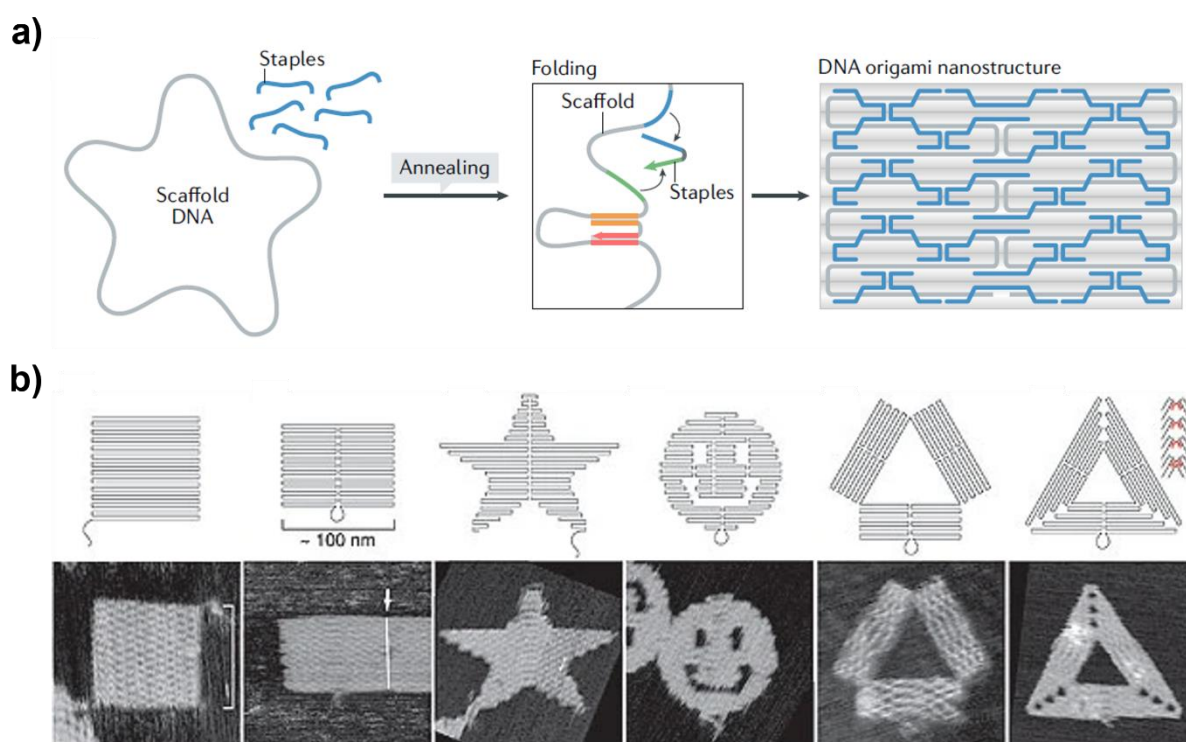


Figure 2.3 a) Schematic illustration of DNA origami assembly from scaffold DNA via folding with complementary staple strands into a well-defined DNA origami nanostructure. Adapted with permission.³⁶ Copyright © 2021, Springer Nature Limited. b) Examples of 2D DNA origami designs created by Rothemund ranging from square and rectangular shapes to stars, smileys and two different triangular shapes with corresponding AFM images. Adapted with permission.⁴ Copyright © 2006, Springer Nature Limited.

The fundamental approach of designing a 2D DNA origami nanostructure is precisely described by Rothemund⁴. The folding path of a 2D DNA origami nanostructure consists of parallel double helices with an integer number of turns that are adjacently connected with each other via crossovers (see Figure 2.3 a)). The crossovers are periodically arranged antiparallel between two helices in an alternating way with odd numbers, e.g., every 1.5 turn (16 bp), in order to create and hold the desired pattern of the scaffold. Furthermore, the scaffold follows up the shape from line to line, hence scaffold crossovers are implemented as well. Computational calculations are done for each staple strand to create an individual set of short, sequenced oligonucleotides that interact specifically at each desired region of the DNA origami nanostructure via complementary Watson-Crick base pairing. Furthermore, to reduce inner geometric strain in the DNA origami nanostructure that inherently are caused by the non-integer number of base pairs per turn, the arrangement of each minor groove of the periodic crossover in each column alters between facing up and down. Strain effects in scaffold crossovers are reduced by twist correction. The overall stability in the design process is eventually increased via merging two adjacent staple strands as well as recombine staple strands at the seam region to create so called bridge staples.⁴

From then, DNA origami nanotechnology started to drastically evolve presenting a variety of 3D shape models based on folding helices on a honeycomb lattice,³⁷ creating multi-layer DNA helix bundles,³⁸ polyhedral structures,^{39,40} and DNA origami crystal lattices.⁴¹

In parallel, within the popularity and the opportunities the new synthetic method provided, the research for applications with DNA origami nanostructures tremendously increased in numerous fields as in biomedicine,⁵ and biosensing,⁶ biophysics,⁷ nanoelectronics,⁸ and nanopatterning.⁹

2.3 DNA origami stability

The wide field of applications that DNA origami nanotechnology nowadays potentially offers relies on their structural stability and integrity under various conditions.^{5,10-12}

In general, it has been shown, that DNA origami nanostructures inherently possess reasonable stability properties under different chemical environments,¹⁵ buffer conditions,¹⁶ and by ionizing radiation,¹⁷ Moreover, cryogenic temperatures studies of DNA origamis revealed high longevity properties.^{18,19} On the other side, they are also surprisingly unaffected of harsh thermal conditions when adsorbed on the surface.^{15,20}

However, limitations on the stability of DNA origami could be observed at low cation concentrations,^{21,22} especially of divalent cation Mg^{2+} , in the presence of nucleases,^{23,24} and at chaotropic conditions.^{25,26}

The essential key for DNA origami assembly and stability is the cationic presence in solution in order to screen the high negatively charged backbone of the DNA and thus overcome the repulsive interaction of helices.^{13,14} To this end, the divalent cation Mg^{2+} shows to be more favorable in binding to the DNA than the monovalent cation Na^+ , for instance.¹⁴ Hence, studies in low-magnesium buffers revealed a partially denaturation of DNA origami nanostructures.²² Besides that, studies of DNA origamis in presence of nucleases led to a degradation of the superstructure.^{23,24} Most intriguing, it could also been shown, that the design of the DNA origami nanostructure has a significant effect on the stability in low-magnesium buffer and also on the digestion resistance.²²⁻²⁴ Furthermore, studies on DNA origami exposure to chaotropic salts, as guanidinium chloride (GdmCl) or urea, demonstrated strong salt and cation concentration- as well as temperature-dependent denaturation effects by having a significant impact on their melting temperature and the structural integrity.^{25,26}

In order to enhance the stability of the DNA origami against these several issues, different approaches might potentially be reliable such as shape-design modifications,²⁴ protein coating,⁴² enzymatic ligation,⁴³ or silification.⁴⁴ Apart from that, also interface interplay seems to have a positive effect on the stability of the DNA origami.⁴⁵

2.4 Chaotropic salts

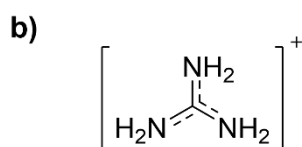
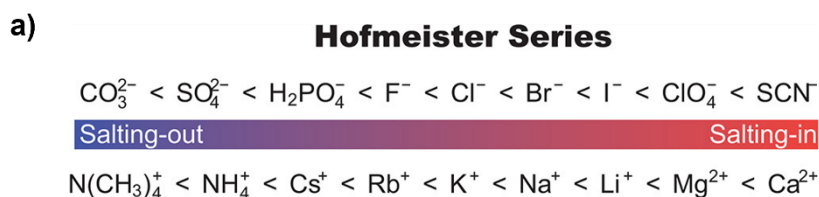
Hofmeister⁴⁶ published studies about the specific effect of several ions in solution with the aim to elucidate a relation between their behavior and individual properties that nowadays is listed and represented as the Hofmeister series.^{47,48} This series is giving information about how cations and anions specifically interact with water molecules and the consequences from it. This results in a suborder of so called kosmotropes and chaotropes.⁴⁹ Kosmotropes are ions of high charge density with a strong hydration affinity but a weak effect on the hydration shell of solutes. This kosmotropic effect leads to stabilizing bio- macromolecules in solution and, depending on the concentration, to salting-out. In contrast, chaotropes are ions of low charge density with a weak hydration affinity but a strong effect on the hydration shell of solutes by disordering the water structures via H-bonding interactions and having direct interaction with the macromolecules. This chaotropic effect leads to destabilizing bio- macromolecules native

folding in solution and salting-in.⁴⁸⁻⁵³ A graphical table of the Hofmeister series for cations and anions is represented in Figure 2.4 a). However, depending on the overall conditions, reversed behavior of the Hofmeister series were also reported.⁵⁴⁻⁵⁶

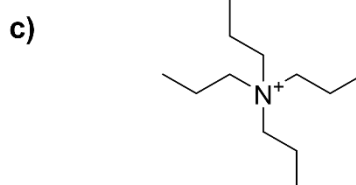
The application field of chaotropic agents addresses protein denaturation studies,^{57,58} biosensor system,⁵⁹ messenger RNA manufacturing,⁶⁰ DNA isolation,⁶¹ and thermal stability of DNA.⁶² Moreover, DNA origami related applications with chaotropic agents were also reported, e.g., isothermal DNA origami assembly,⁶³ self-assembly of DNA origami at room temperature conditions,⁶⁴ or from dsDNA scaffold,⁶⁵ and unpurified intact bacteriophages.⁶⁶

The variety of applications and different species of chaotropic agents make them a versatile tool in biological contexts. However, because of this huge variety, this work was focused on two chaotropic agents, i.e., guanidinium (Gdm) and tetrapropylammonium (TPA) salts (see Figure 2.4 b) and c)).

Guanidinium is a positively charged planar cation with a centered sp^2 -hybridized C-atom and three NH-groups. Its low hydrated planar face leads to hydrophobic stacking of Gdm^+ - Gdm^+ via cation- π interaction while all three NH-groups tend to form hydrogen bonds in solution. The variety of Gdm^+ to potentially interact with biomacromolecules via different mechanisms makes it a strong chaotropic agent. However, the efficiency of Gdm^+ as a chaotropic agent in solution drastically depends on the present anion and can be followed by the Hofmeister series. For instance, studies on Gdm^+ with SO_4^{2-} as a strongly hydrated anion have shown to exhibit a stabilizing effect on biomacromolecules by exclusion and Gdm^+ - SO_4^{2-} pairing. In this case, hydrated anions are depleted from the biomacromolecule/water interface and thus do not interact directly with the biomacromolecule. In contrast, Gdm^+ paired with Cl^- or SCN^- that are moderate till low hydrated anions, respectively, destabilized biomacromolecules by inclusion. In this case, the ions are strongly present in the biomolecule/water interface and thus interact directly with the biomacromolecule. However, the interaction is rather complex and highly concentration dependent. Thus, lower concentrations of $GdmSCN$ could also have a stabilizing effect via only moderate inclusion and turned around to destabilize at higher concentrations via high inclusion, while $GdmCl$ did not show that inverse effect.^{52,53,67,68}



Guanidinium (Gdm)



Tetrapropylammonium (TPA)

Figure 2.4 a) Graphical representation of the Hofmeister series for cations and anions. Blue and red colored shading indicate the tendency of ions to affect salting-out and salting-in, respectively. Reprinted with permission.⁵⁶ Copyright © 2013, American Chemical Society. b) Structural formula of guanidinium cation. c) Structural formula of tetrapropylammonium cation.

Interestingly, and in contrast to proteins, spectroscopic and MD simulations studies about the interaction of Gdm^+ as GdmCl salt with B-DNA revealed to have a stabilizing effect on the DNA via forming intra-strand hydrogen bonds between the cation and nucleobases preferably in the minor grooves. As a result, the interaction affects the width of the minor grooves by decreasing the distance between the adjacent nucleobases that might explain the increase of the stability of the DNA.^{69,70}

TPA, on the other hand, is a cation with low charge density of a tetrahedral shape with four aliphatic propyl chains, forming four flat faces. Although both cations have similar positions in the Hofmeister series and are strong chaotropic cations, their physicochemical properties are quite different. TPA^+ is a much larger ion than Gdm^+ and due to its comparable lower charge density and lack of the capability forming hydrogen bonds, homo- and hetero-ion pairing of TPA^+ - TPA^+ and TPA^+ - SO_4^{2-} could not be observed. Hence, the anionic effects of TPA salts compared to Gdm salts can be considered negligible. Instead, interaction of TPA^+ with polypeptides primarily occurs via hydrophobic interactions.^{52,68,71}

2.5 Drug loading of DNA origami

The generation of DNA origami nanotechnology provides tremendous innovations in the field of biological applications.⁷² In this context, advantages that DNA origami nanostructures inherently offer are high biocompatibility,⁷³ as well as high functionality and efficient targeting in drug delivery systems as nanocarrier for cancer therapy, theragnostic and in the application of immuno- and phototherapie.^{72,74-77}

The general mechanisms of non-covalent drug loading of DNA origami nanostructures can mainly be sub-divided into three categories, i.e., intercalation,⁷⁸⁻⁸¹ groove-binding,^{79,82-86} and electrostatic binding.^{87,88}

Intercalation is a non-covalent binding between dsDNA and a small organic molecule with a flat and aromatic moiety. The binding of the so-called mono-intercalator occurs in between the base pairs via π - π stacking, hydrophobic and van der Waals interaction as the driving forces. Besides mono-intercalators, there also exist bis-intercalators, i.e., two mono-intercalators covalently binding together, as well as threading intercalators exhibiting side chains from both sides and thus binding in two grooves of a DNA. The intercalation leads to a partial unwinding and lengthening of the DNA double strand but also stabilizes the DNA molecule. The biological function of intercalators is the inhibition of DNA replication as well as transcription thus having vast relevance in cancer therapy applications.^{72,78,79}

Quite prominent intercalators that were studied in DNA origami drug loading and delivery systems as chemotherapeutic drugs are doxorubicin and daunorubicin,⁸⁹ for instance.^{72,74,90}

Groove binding drug molecules dominantly bind to the minor groove of the DNA. Depending on the molecule properties, the binding can have an impact on the groove geometry by enlarging its width. The characteristic molecular structure of minor groove binders is curved to enhance the compatibility binding in between the minor groove region of the DNA. The interaction of the minor groove binders and DNA occurs via hydrophobic interactions, van der Waals, electrostatic interactions, and hydrogen bonding.^{79,83}

A prominent minor groove binder is netropsin^{91,92} that was already used in DNA origami drug loading studies.^{85,86}

However, the binding model of drug molecules drastically depends on the condition. So, for instance, methylene blue (MB), a photosensitizer,⁹³ intercalates in DNA at low salt

concentration of Mg^{2+} , while at higher salt concentration, the binding mode changes to groove binding.⁹⁴ Study of MB on DNA origami drug loading was conducted showing binding efficiency depending on the DNA origami superstructure. It has been demonstrated that drug loading of DNA origami nanostructures with MB is strongly affected by the DNA topology in the lattice design, i.e., honeycomb and square lattice, respectively. However, also the flexibility properties of each individual nanostructure seem to play a significant role in efficient DNA origami drug loading.⁸⁶

Besides intercalation and groove binding, non-covalent binding of drug molecules with DNA nanostructures via electrostatic interaction was also realized. For instance, the study of loading vancomycin⁹⁵ on DNA nanogels via electrostatic interaction has shown higher loading efficiencies.⁸⁸

3 Methods

3.1 Atomic force microscopy (AFM)

Atomic force microscopy (AFM) was introduced by Binnig et al.⁹⁶ in 1986 presenting a new microscopic technique that is able to scan and resolve surface topographies on an atomic scale of conductive and non-conductive samples in air and liquid.^{96,97}

The principle of this method relies on the force interactions between a sharp tip and a surface sample when both are in close proximity to each other. A simplified construction of an AFM setup is illustrated in Figure 3.1 a). The sharp tip is located at the end of a cantilever that is mounted on a piezoelectric actuator. When the tip is scanning the sample, changes in force between the tip and the surface lead to a deformation of the cantilever. The deformation of the cantilever is detected by the deflection of a laser beam, that is directly focused on top of the cantilever, through a photodiode while either the applied force or the height of the cantilever with respect to the sample is kept at a constant value by a feedback loop. Hence, alteration in the signal on the photodiode can give information about the height changes at constant applied force or deflection forces at constant height of the cantilever that can directly be monitored.⁹⁸

The operation with AFM can generally be separated into three different modes, i.e., contact mode, non-contact mode and tapping mode, in that different intermolecular forces are dominant (see Figure 3.1 b)).⁹⁸

In contact mode, the tip is in direct contact with the sample surface while scanning. Hence, repulsive interaction between the tip and the surface is dominant due to Pauli and electrostatic repulsion. The operation in this mode is typically performed at constant force applied of the cantilever on the surface in the region of nN. In order to control the force of the cantilever, a certain set-point is defined by the amount of the laser deflection on the photodiode and constantly kept at that value during the scan via a feedback loop. Topographical changes at the surface lead to an offset in the deflection (signal error) of the cantilever compared to the set-point. As a response, the height of the cantilever is adjusted by applying a certain voltage on the piezoelectric actuator to reach again the set-point. These height adjustments via the voltage correlate with the topography information of the sample and so can be displayed.⁹⁸ Although the setup of this mode is straightforward, capillary effects and high shear forces make the

contact-mode less suitable for measurement of soft samples as biomolecules, for instance, due to deformation or displacement of the molecule at the surface.^{98,99}

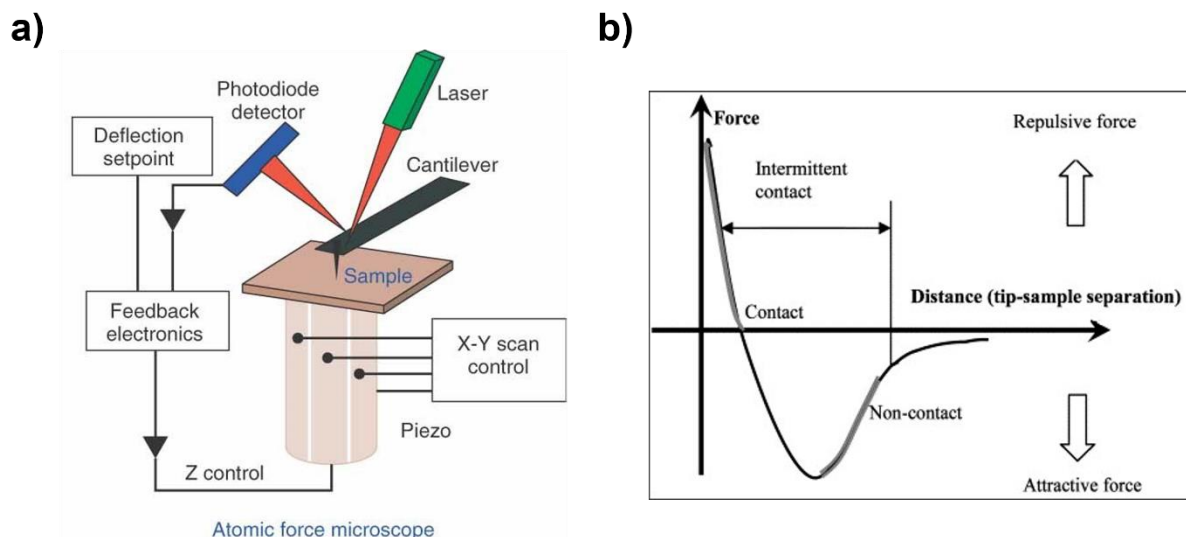


Figure 3.1 a) Scheme of a general AFM setup. A cantilever with a sharp tip is scanning over a sample. Force interactions between the tip and the sample surface lead to deformation of the cantilever that is directly detected by the laser deflection at a photodiode detector. Adapted with permission.⁹⁷ Copyright © 2010, John Wiley & Sons, Inc. b) Schematic illustration of a force distance curve resulting from long-range attractive van der Waals forces and short-range repulsive forces due to Pauli and electrostatic repulsion. Regimes the different AFM modes are operating in, i.e., repulsive regime in contact mode, attractive regime in non-contact mode, and tapping mode in-between both force regimes. Reprinted with permission.⁹⁸ Copyright © 2004, Elsevier Ltd. All rights reserved.

In complete opposite, i.e., in non-contact mode,¹⁰⁰ the cantilever oscillates at a certain distance to the sample surface. Hence, long-range attractive van der Waals forces between the tip and the surface are dominant (see Figure 3.1 b). In this mode, the value of the amplitude is used as the set-point and kept constantly during the scan via a feedback loop. This mode feasibly enables measurements of soft samples because deformation and displacement of the molecules on the surface can be neglected. However, since the cantilever is significantly far away from the surface and long-range attractive interaction are inherently small, measurements of the surface can be insufficient in terms of the resolution.⁹⁸

The tapping mode¹⁰¹ significantly mitigates the issues that contact and non-contact modes are causing. Therefore, the cantilever is excited via a piezoelectric actuator to oscillate near its resonance frequency and tapping the surface during the scan. The amplitude of the oscillated cantilever is used as the set-point and kept constantly via the feedback loop. While the cantilever approaches the surface a change in the resonance frequency and the amplitude magnitude occurs. Attractive long-range interactions lead to a shift of lower resonance frequencies while repulsive Pauli and electrostatic interactions increase the resonance frequency of the cantilever during the intermittent approach and retreat (see Figure 3.1 b)). Thus, the changes in the amplitude with respect to the set-point (error signal) are detected by the photodiode. To maintain the set-point amplitude, the distance between the tip and the sample is adjusted by applying a certain voltage to the piezoelectric actuator.^{98,102} Since the time between the contact of the tip with the surface is drastically reduced, shear forces that might cause displacement of molecules as well as deformation issues are significantly reduced. Thus, tapping mode is highly suitable for imaging of soft samples as biological molecules, for instance.^{97,99}

In addition, an advanced technique, called peak-force tapping AFM, that was introduced by Adamcik et al.¹⁰³ in 2011, provides a direct control of the applied force of the cantilever to the sample. Here, the cantilever is excited to oscillate with a rather low frequency around 2 kHz with an amplitude of 300 nm in air. Other than conventional tapping mode, the tip is in short contact with the sample with a defined force collecting continuous force-distance curves at each pixel of the sample image. Thus, various information of the surface can be obtained at the same time, as topography, adhesion as well as nanomechanical properties of the surface.¹⁰⁴⁻¹⁰⁶

3.2 Atomic force microscopy infrared spectroscopy (AFM-IR)

Atomic force microscopy infrared spectroscopy (AFM-IR) is a technique that enables infrared spectroscopy (IR) of samples with a spatial resolution of atomic force microscopy (AFM) and was first introduced by Dazzi et al.¹⁰⁷ in 2005.¹⁰⁸

The principle of an AFM-IR measurement relies on the photothermal effect by direct IR light absorption of a sample through a tunable IR laser source (see Figure 3.2). Therefore, an IR laser is directly focused under an AFM tip and if the wavelength of the IR light matches with the absorption range of the sample material, a local thermal expansion occurs that can be directly detected by the cantilever via deflection changes at the photodiode. Normally, the IR laser

source is operating in pulse mode leading to an oscillation motion of the cantilever during the exposure due to alternate thermal expansion and relaxation of the sample material. The deflection of the cantilever as a measure of the amount of the absorbed IR light can then be plotted as a function of the wavelength that results in an IR absorption spectrum of the sample with a spatial resolution of approx. 10 nm. Alternatively, a fixed wavelength can be set for scanning an area of the sample to provide a chemical image of the surface.^{108–110}

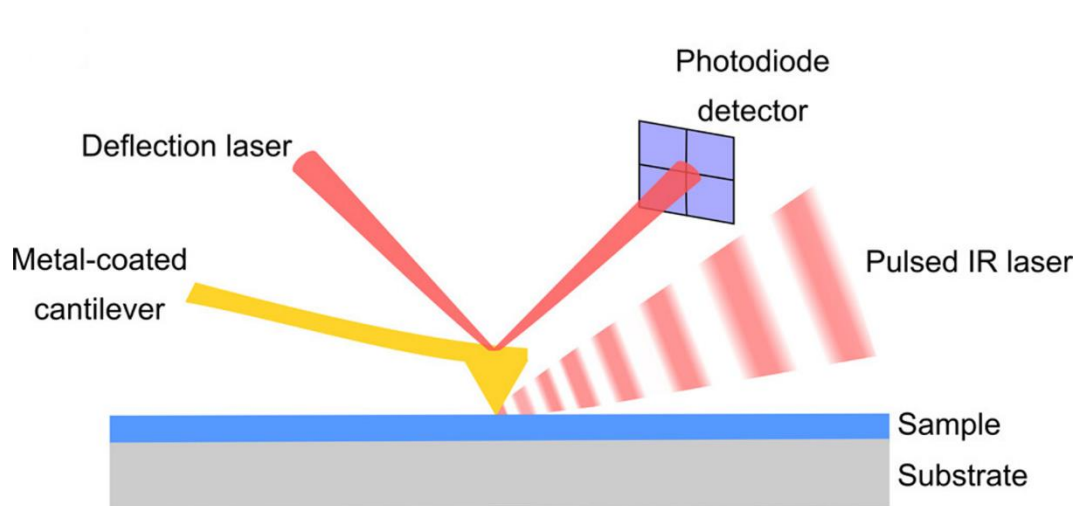


Figure 3.2 Simplified schematic illustration of AFM-IR setup and work principle. A pulsed IR laser is directly focused under an AFM tip on a sample. When the wavelength of the IR light is absorbed from sample material, absorption leads to a local thermal expansion that can be directly detected by the cantilever via deflection changes on the photodiode. The deflection of the cantilever is monitored and detected over time. Correlation between deflection oscillation amplitude and the wavenumber provides an absorption spectrum. Adapted with permission.¹⁰⁹ Copyright © 2023 The Authors. Published by American Chemical Society. This publication is licensed under CC-BY 4.0.

AFM-IR can be operated like AFM in various modes, i.e., ringdown or resonance enhanced contact mode, tapping mode, and peak-force tapping IR (PFIR) depending on the sample properties, resolution (depth) output, and sample information of high interest.¹⁰⁹

In both contact modes, the cantilever tip is constantly in direct contact with the surface, while the IR excitation of both modes significantly differs (see Figure 3.3 a) and b)). In ringdown contact mode, that was firstly invented, the pulse rate of the laser is rather low around 1 Hz pulsing with short pulse lengths approx. between 0.2- 500 ns leading to a thermal expansion of

the sample in IR absorption range and thus to an oscillation of the cantilever. Due to the low repetition rate of the pulsed laser, the cantilever relaxation time is relatively long compared to the thermal expansion time resulting in a ringdown decay. The obtained signal from the ringdown decay contains the amplitudes from several overtones of the oscillated cantilever that correlate proportionally with the optical absorption coefficient of the sample material. The ringdown contact-mode provides comparatively lower sensitivity than the resonance enhanced contact mode. Here, the pulse rates of the IR laser are set to values that match with the contact resonance frequency of the used cantilever, i.e., normally higher than 10 kHz, and so substantially increase the oscillation amplitude leading to approx. 5-40 times higher signal amplification than operation in ringdown contact mode enabling signal detection of much thinner samples. To constantly match the pulse rate of the IR laser with the cantilever contact resonance frequency, a phase-locked loop (PLL) is used. The contact modes provide a lateral resolution of approx. 10 nm and a sample depth information of over 1 μm .^{109,110}

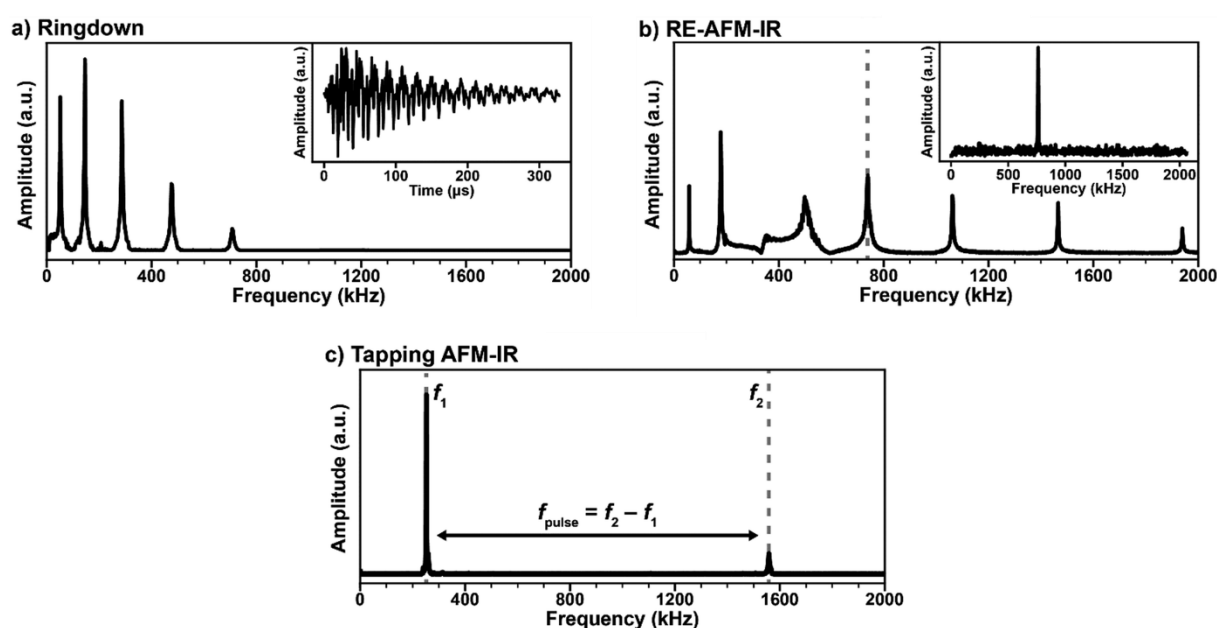


Figure 3.3 AFM-IR obtained signal in different operation modes. a) Contact mode with ringdown excitation operates with low repetition rates of the pulsed laser leading to long cantilever relaxation time resulting in a ring-down decay. Excitation of several overtones of the cantilever provides several amplitude signals at different frequencies. Values of amplitude signal are proportional to optical absorption coefficient of the sample material. b) Resonance enhanced contact mode operates with repetition rates of the pulsed laser that match with the contact resonance frequency of the used cantilever leading to much higher amplitude signals. c) Tapping AFM-IR mode operates with an excited cantilever

near to its resonance frequencies of an overtone, f_2 in this scheme, while the detection of the signal from the IR excited sample is detected via demodulation at another resonance frequency of the cantilever, here f_1 . The pulse rate of the IR laser is set to the value of $f_p = f_2 - f_1$. Adapted with permission.¹¹⁰ Copyright © 2022, The Royal Society of Chemistry. Licensed under Creative Commons Attribution 3.0 Unported Licence.

The tapping AFM-IR mode operates with an excited cantilever near to its resonance frequencies of an overtone, e.g., f_2 , while the detection of the signal from the IR excited sample is detected via demodulation at another resonance frequency of the cantilever, e.g., f_1 or vice versa (see Figure 3.3 c)). The pulse rate of the IR laser is set to the value of $f_p = f_2 - f_1$, detected in heterodyne scheme via demodulating f_1 or f_2 depending on the chosen resonance frequency of the cantilever. A PLL is used to keep the pulse rate within that optimum area of f_p during the measurement. Like conventional AFM, due to the relatively short contact time between the oscillated cantilever and the sample, lateral forces are drastically reduced improving the imaging of soft samples as biomolecules or certain polymers. Another upside of the tapping AFM-IR mode is the enhanced spatial resolution with values lower than 10 nm, however, since the cantilever is only intermittently in contact with the surface, less signal intensity with lower signal-to-noise ratios are the downsides of this mode.^{109,110}

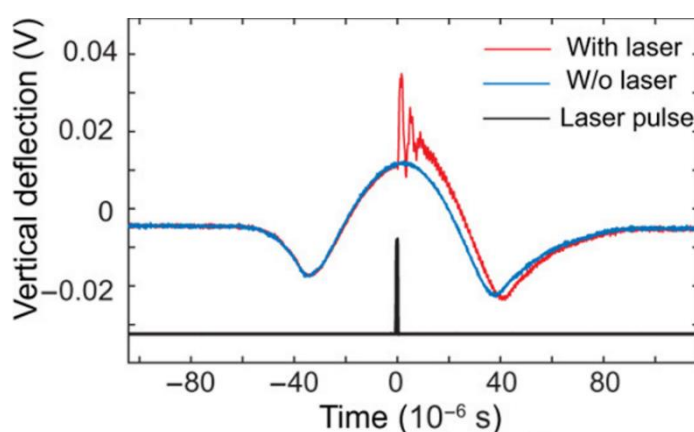


Figure 3.4 Diagram of the vertical deflection of the cantilever as a function of time during a peak-force tapping cycle with (red line) and without (blue line) a laser pulse while the cantilever is in contact with the surface. The expansion of the sample material is detected by the cantilever resulting in a ringdown scheme that is used to obtain the absorption spectrum. Adapted with permission.¹¹¹ Copyright © 2017,

The peak-force tapping IR (PFIR)¹¹¹ is based on the conventional peak-force tapping AFM where the cantilever oscillates with a low frequency of around 2-4 kHz being in contact with the sample for a relative short time with a certain applied force, measured by the deflection of the cantilever at the photodiode (see Figure 3.4). Whenever the cantilever is in contact with the sample, the IR laser excites the sample leading to a photothermal expansion that is directly detected by the cantilever with a subsequent relaxation. The absorption signal can then be determined from the ringdown scheme to obtain the absorption spectrum. This mode provides higher signal-to-noise ratios than the tapping AFM-IR mode by simultaneously being highly suitable for soft samples. In addition, due to the peak-force tapping, information about mechanical properties of the sample can also be obtained.^{109,110,112}

3.3 Fluorescence spectroscopy

Fluorescence spectroscopy is a widely used technique in various biological applications.¹¹³⁻¹¹⁵ The technique relies on the phenomenon of light emission from an electronically excited molecule, called luminescence, and can be separated into two mechanisms, i.e., fluorescence and phosphorescence.¹¹⁶

The overall excitation and emission process is well illustrated by the Jablonski diagram (see Fig. 3.5). Thus, an electron of a fluorescent molecule, called fluorophore, is excited via photon illumination from the singlet ground state S_0 to an excited first or second singlet state S_1 or S_2 , respectively, with opposite spin configuration. The excitation process occurs extremely fast within 10^{-15} s and normally also leads the electron to higher vibrational and rotational energy levels of S_1 or S_2 . Furthermore, electrons with higher energy levels within their state typically undergo a quick vibrational relaxation (10^{-12} s) to the lowest energy level of S_1 , called internal conversion. In fluorescence, the subsequent emission of light from the lowest vibrational energy level of S_1 occurs via spin-allowed relaxation to a higher vibrational energy of the ground state S_0 within 10^{-9} s with further vibrational relaxation. However, in phosphorescence, spin conversion of an electron, called intersystem crossing, from the first singlet state S_1 to the first

triplet state T_1 with parallel spin configuration leads to a comparatively slower spin-forbidden relaxation to the ground state S_0 ($\geq 10^{-6} \text{ s}^{-1}$).^{116,117}

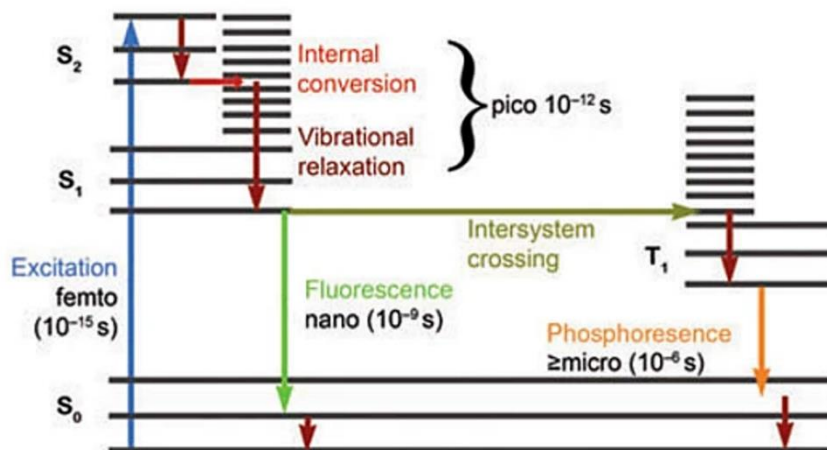


Figure 3.5 Jablonski diagram. Adapted with permission.¹¹⁷ Copyright © 2005, Springer Nature America, Inc.

As a consequence of internal conversion and electron relaxation to higher vibrational energy of the ground state S_0 , the emission spectra of the fluorescence typically exhibit a Stokes shift to higher wavelengths with a symmetric appearance regarding the excitation spectra.^{116,117}

The typical fluorophores consist of several aromatic pi-systems that can be excited in the UV/VIS range. They are subdivided into two categories, i.e., intrinsic, and extrinsic fluorophores. Intrinsic fluorophores are natural molecules with fluorescent properties, as aromatic amino acids or NADH, for instance. On the other hand, extrinsic fluorophores are used to provide fluorescence in a non-fluorescent sample, e.g., fluorescein or rhodamine of labeling antibodies. For DNA labeling, fluorophores are usually chosen that have an excitation area above UV-spectrum. One of the most popular fluorophores with high binding affinities to DNA is ethidium bromide. In addition, fluorophores of cyanine class as Cy-3, Cy-5, and Cy-7, are very common dyes with fluorescent properties in red and near-infrared wavelength spectrum. However, the variety of fluorophores mentioned here is only a very small assortment of many more dyes that can be easily modified for a bunch of different experiment approaches.¹¹⁶

Fluorescence spectroscopy is experimentally measured via a spectrofluorometer. A simplified setup of the spectrofluorometer is shown in Figure 3.6. Xe or Xe-Hg lamps are mainly used as the light source for covering the excitation range of approx. 250-700 nm. An excitation monochromator is used to filter the polychromatic light from the source that eventually shines through a cuvette sample. The emission light is detected in a 90° angle with respect to the incoming light of the source. An emission monochromator filters the wavelengths of the emitted light that then is detected.¹¹⁶

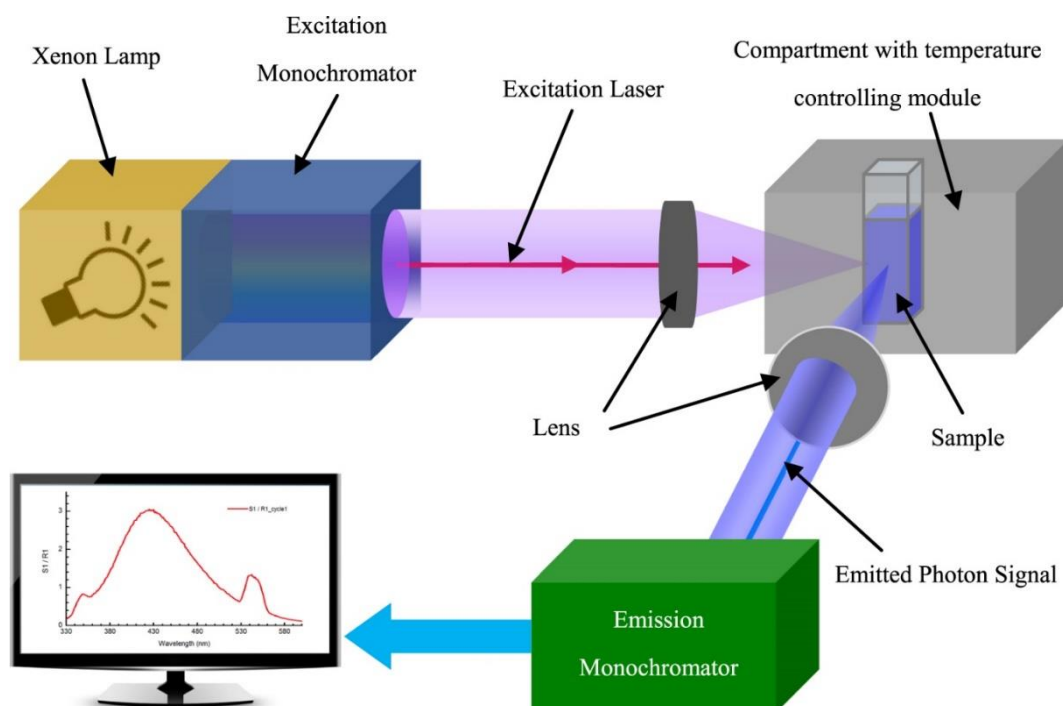


Figure 3.6 Setup of a spectrofluorometer. Reprinted with permission.¹¹⁸ Copyright © 2014, IOP Publishing Ltd. Permission conveyed through Copyright Clearance Center, Inc.

Besides conventional fluorescence spectroscopy, fluorescence microscopy is commonly used to image biological samples.^{117,119} Moreover, in combination with the Förster resonance energy transfer (FRET), fluorescence signals of single molecules can be detected that provide information about molecular conformational changes and intra- and intermolecular distances withing nanometer ranges.^{120,121}

4 Biophysical stability studies of DNA origami nanostructures under various chaotropic conditions

4.1 Anion-specific structure and stability of guanidinium-bound DNA origami

4.1.1 Introduction

Over the last decade, DNA origami technology⁴ has made significant advances and gained more and more relevance in a wide field of applications ranging from biomedicine^{5,6} to biophysics^{7,122} to chemical^{123,124} and synthetic biology.^{125,126} Despite the large number of applications, the unique capabilities of DNA origami to build up biocompatible, well-defined 2D and 3D molecular assemblies of almost arbitrary shape have not been utilized to their fullest extent yet.³⁶ A widely perceived issue concerns the limited stability of DNA origami nanostructures under conditions that deviate from those employed in DNA origami assembly.^{5,11,127} Although several DNA origami nanostructures were found to be remarkably stable in various electrolytes featuring different buffers, pH values, and salt compositions,^{16,22,24} as well as during long-term cryostorage,^{18,19} the peculiar arrangement of double helices that comprise their individual 3D structure may lead to unexpected and surprising behaviors in denaturing environments such as low-salt conditions,^{22,24} under nuclease digestion,^{23,24} or in the presence of chaotropes.²⁵ The latter example is particularly interesting at a fundamental level because the interaction of chaotropic agents such as different guanidinium (Gdm) salts with DNA is highly complex and so far barely understood. Guanidinium chloride (GdmCl), for instance, is a widely employed and potent protein denaturant,¹²⁸ whose interaction with DNA has only recently received some attention.^{25,26,69,70} Moreover, despite having been studied for several decades, even the ubiquitously employed Gdm⁺-induced denaturation of proteins is not completely understood yet.^{52,53,68,71} From an application-oriented point of view, the interaction of chemical denaturants with DNA is highly relevant for various processes such as isothermal and low-temperature DNA origami assembly,^{63,64} assembly of DNA origami nanostructures from double-stranded (ds) DNA,⁶⁵ and intact bacteriophages,⁶⁶ selective DNA origami denaturation for analytical purposes,¹²⁹ and the removal of DNA origami masks in molecular lithography.^{130,131} In this context, Gdm⁺ is particularly interesting because its effect on DNA origami nanostructures is

strongly influenced by concentration, temperature, and the presence and concentration of other ions,^{25,26} which may be exploited for fine-tuning its activity to precisely match the requirements of a given application.

The structure of Gdm (see Figure 2.4 b)) is characterized by planar hydrophobic faces made up by three NH₂ groups bound through delocalized bonds to a single sp²-hybridized carbon atom. Therefore, hydrophobic interactions as well as the formation of hydrogen bonds between the cation and various amino acids may occur and participate in protein denaturation.⁶⁸ Intriguingly, it has been demonstrated that the denaturing effect of the Gdm⁺ ion also depends strongly on its counteranion.^{52,53,68} In particular, a correlation between the Hofmeister series and the denaturing effect of selective anions has been shown.⁵³ On the other hand, distortions of the microscopic structure of water are due to the combined effect of the cation-anion pairs, which questions the significance of the Hofmeister concept of “structure maker or breaker” for any single ion.¹³² Likewise, direct ion-polymer interactions modulate the detailed energy balance of the denatured vs. the native state of a biopolymer in salt solutions.¹³³ Thus, it cannot be expected that the existing concepts of protein denaturation by Gdm⁺ would equally apply to a complex supramolecular DNA nanostructure. In addition, the present knowledge on the salt-dependence of dsDNA stability has been gained with synthetic or genomic dsDNA of different lengths, rather than the extended DNA assemblies in DNA origami nanostructures. In contrast to other DNA condensates formed by DNA-condensing molecules, stability of the DNA origami is provided by directed hybridization and not by sequence-independent cation-mediated aggregation. Also in the latter, the analysis of salt effects has naturally focused on cations, which engage in direct electrostatic interactions with the anionic DNA backbone.^{134,135}

In this work, the stability of 2D DNA origami triangles⁴ in the presence of either GdmCl or guanidinium sulfate (Gdm₂SO₄) was investigated. To this end, DNA origami triangles were incubated with the selected salts at different temperatures for 1 h. After the incubation, the DNA origami triangles were adsorbed on mica in order to further analyze the superstructural changes by *ex-situ* atomic force microscopy (AFM) (see Figure 4.1).

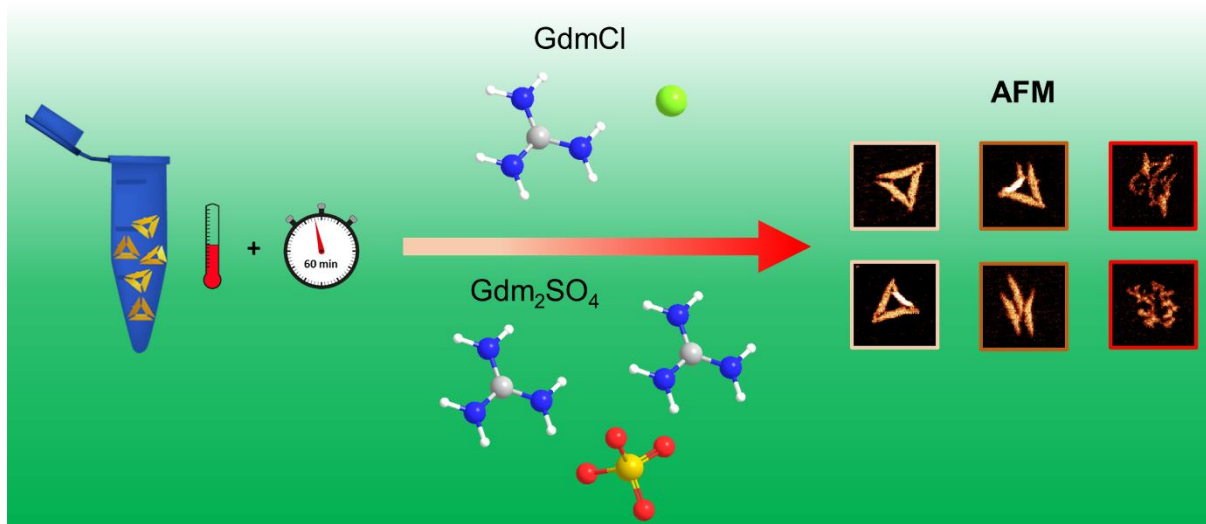


Figure 4.1 Experimental approach: The nanostructural integrity of DNA origami triangles after exposure to GdmCl and Gdm₂SO₄ for one hour is evaluated at selected temperatures by AFM. Selected AFM images of damaged triangles are depicted that show different states of damage moieties, ranging from ruptured vertices between individual trapezoids to complete denatured structures. In the ball-and-stick models, H, C, N, S, O, and Cl atoms are indicated in white, grey, blue, yellow, red, and green, respectively.

The resulting AFM images from ex-situ AFM measurements have been statistically evaluated to obtain relative fractions of “intact” and “damaged” DNA origami. Furthermore, statistical analysis from ex-situ AFM measurements were correlated with in-situ circular dichroism (CD) spectroscopy in order to derive a thermodynamic model of DNA origami denaturation by GdmCl and Gdm₂SO₄ via principle component analysis (PCA) and iterative target test factor analysis (ITTFA).¹³⁶ The circular dichroism (CD) spectroscopy as well as the thermodynamic modelling based on PCA and ITTFA have been performed at Helmholtz-Zentrum Dresden-Rossendorf in the group of Prof. Dr. Fahmy and are not represented in this thesis.

4.1.2 Results and discussion

4.1.2.1 AFM imaging

The interaction of triangular DNA origami nanostructures with the two selected Gdm salts at the nanostructure level was investigated by ex-situ AFM. The ex-situ AFM characterization under dry conditions was specifically chosen for two reasons. i) Initial in-situ AFM imaging

experiments revealed that the presence of high concentrations of Gdm_2SO_4 not only suppresses DNA origami adsorption at the mica surface but can even lead to the desorption of once-adsorbed DNA origami (see Figure 4.2). Therefore, in-situ AFM imaging is not possible under all buffer conditions investigated in the present work. ii) Previous work has shown that DNA origami denaturation in GdmCl may proceed over several hours.²⁵ In order to ensure identical incubation times for all samples and to freeze the state of degradation obtained at a certain time point, the reaction thus needs to be stopped after immobilization of the DNA origami nanostructures at the mica surface by washing and removal of residual Gdm^+ . Therefore, to avoid such issues, the DNA origami triangles were incubated with different concentrations (1 – 6 M) of the respective salt for 1 h at different temperatures ranging from 23 to 42 °C. After dilution in Gdm^+ -free buffer to facilitate efficient adsorption, the samples were incubated on mica surfaces for 5 min, washed, and dried. Then, AFM images were recorded in the dry state to evaluate the relative fractions of “intact” and “damaged” DNA origami. Six examples of DNA origami triangles categorized as “damaged” are shown in Figure 4.1. This category includes any deviation from the perfect triangular shape of untreated DNA origami nanostructures, ranging from ruptured vertices to completely denatured structures that feature only the scaffold.

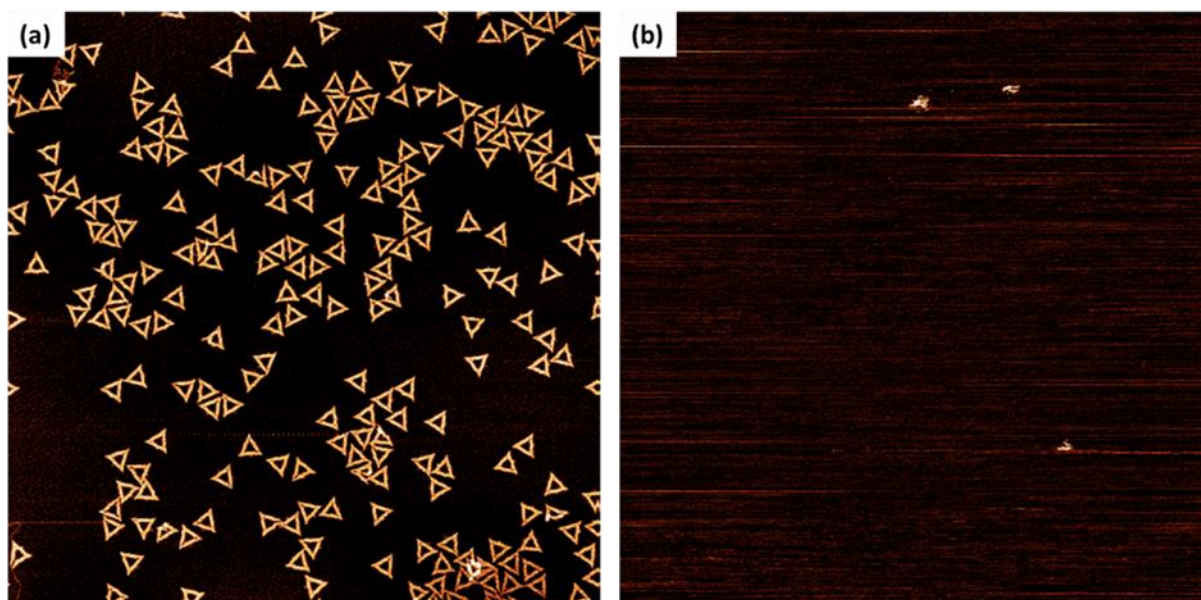


Figure 4.2 AFM images of DNA origami triangles deposited on mica. a) Imaged in air after drying. b) The same sample subsequently imaged in Tris/MgAc₂ buffer with 6 M Gdm_2SO_4 . The images have a size of $3 \times 3 \mu\text{m}^2$ and a z-range of 2 nm.¹³⁶

The general effect of GdmCl on the DNA origami triangles has been characterized previously.²⁵ However, the electrolyte conditions in the present work have been modified in order to match with CD spectroscopic conditions (10 mM Tris acetate, pH 8.0, with 10 mM MgAc₂ instead of 40 mM Tris acetate, pH 8.5, with 1 mM EDTA and 10 mM MgCl₂ as used previously) to enable a thorough correlation of superstructural transitions with molecular details.¹³⁶ The overall trend (see Figure 4.3) is very similar to the previously reported one, showing intact triangular shapes between 23 and 42 °C for GdmCl concentrations up to 4 M. At 6 M GdmCl, intact triangles are observed only below 37 °C, while higher temperatures result in the complete denaturation of all DNA origami nanostructures.

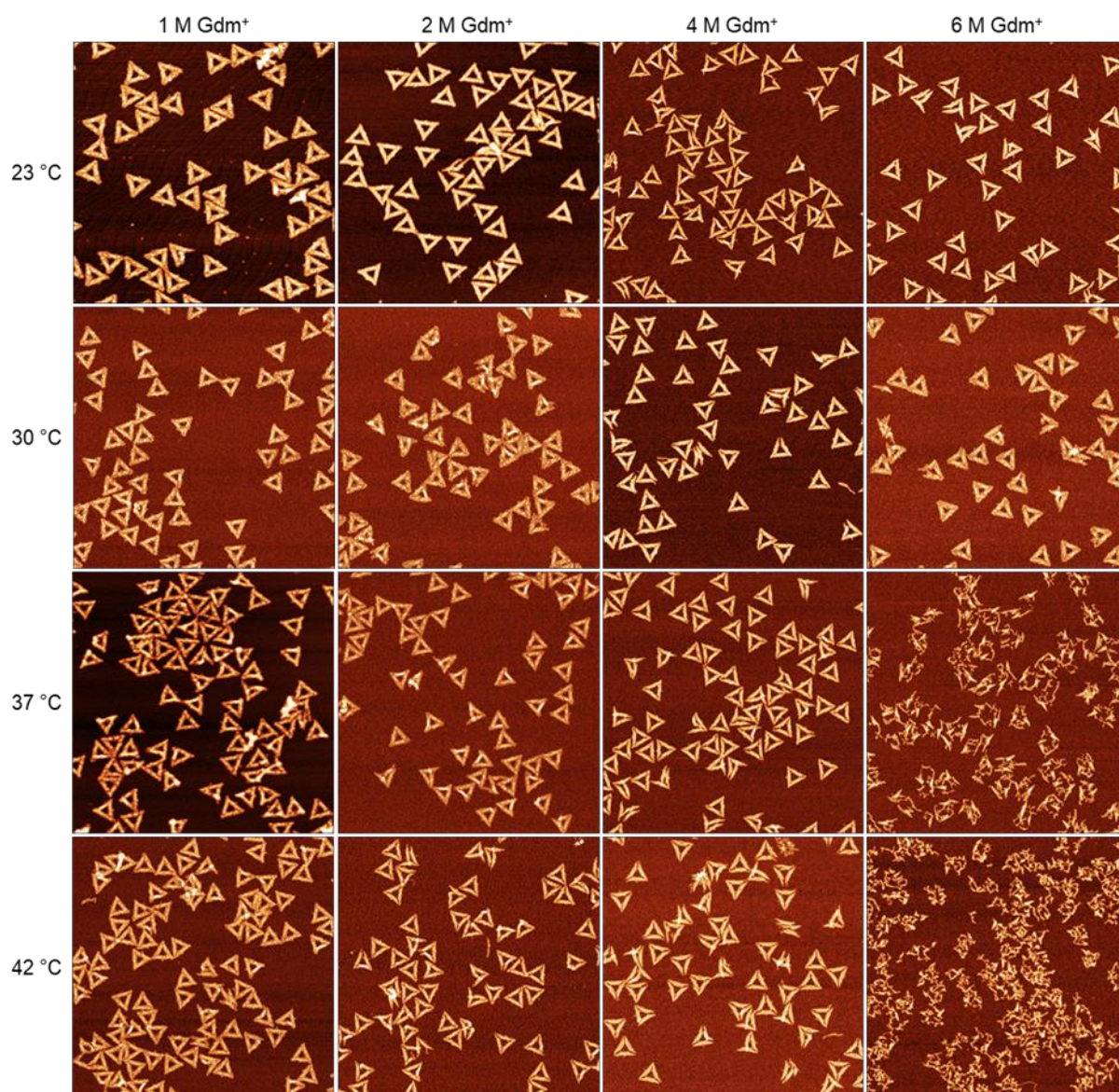


Figure 4.3 AFM images of DNA origami triangles deposited on mica after 1 h incubation in GdmCl at different Gdm⁺ concentrations and temperature conditions. All images have a size of 1.5 x 1.5 μm². The color range was set to automatic with tails cut off.¹³⁶

The statistical analysis of the AFM images shown in Figure 4.4 reveals that in 1 M GdmCl at 23 °C, the fraction of intact DNA origami is slightly above 70 % and thus lower than typical assembly yields of about 90 % observed in the absence of chaotropic agents.¹⁹ This fraction barely changes upon increasing the temperature to 30 °C but drops to about 50 % at 37 and 42 °C. The corresponding AFM images in Figure 4.3 show that the connections between two trapezoids are severed in some of the damaged DNA origami, suggesting that the DNA origami triangle responds most sensitively to Gdm⁺ denaturation at the vertices. This particular sensitivity of the vertices has been observed previously and attributed to the short length of the bridging staples, which are the shortest in the whole triangle design and thus have particularly low melting temperatures.^{25,43}

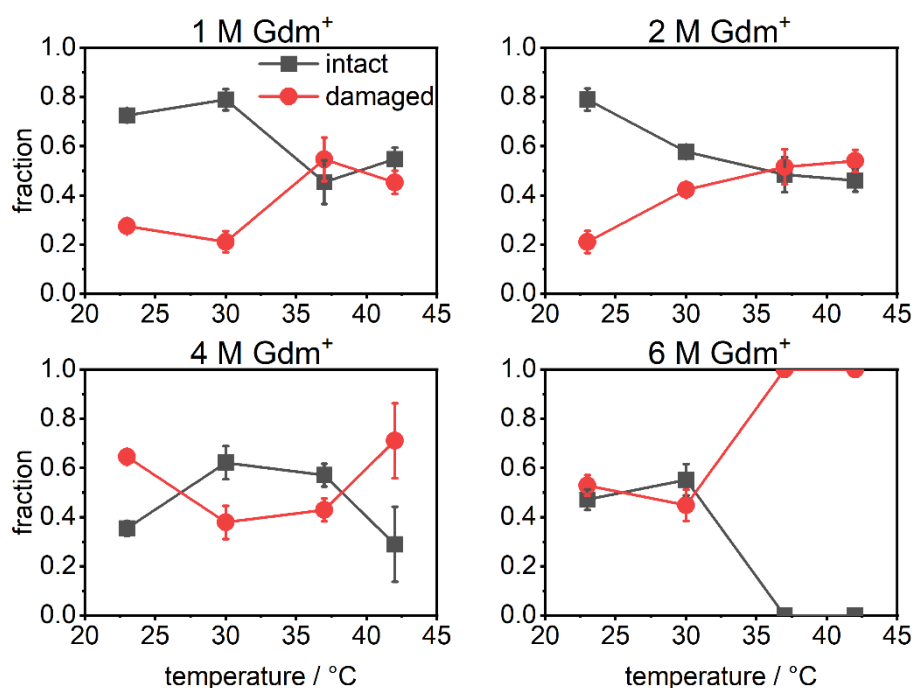


Figure 4.4 Mean fractions of intact and damaged DNA origami triangles after 1 h incubation in GdmCl at different Gdm⁺ concentrations and incubation temperatures. Values represent averages over at least three AFM images with standard deviations given as error bars.

Increasing the GdmCl concentration to 2 M does not affect the DNA origami stability at 23 °C, whereas at 30 °C, only about 60 % of intact structures prevail and higher temperatures further reduce this fraction to below 50 % at 42 °C. The corresponding AFM images in Figure 4.3 reveal preferential damage at the vertices similar to that in 1 M GdmCl. However, some DNA origami triangles are ruptured at all three vertices, resulting in a loosely connected assembly of largely intact trapezoids.

In case of 4 M GdmCl, the results of the statistical analysis reveal a counter-intuitive temperature dependence of the DNA origami stability. Already at 23 °C, most of DNA origami exhibit ruptured vertices or broken trapezoids (see the corresponding AFM image in Figure 4.3), and only about 35 % of the DNA origami remain intact. Surprisingly, the fraction of intact DNA origami triangles recovers to about 60 % upon increasing the temperature to 30 °C. The intact fraction persists at 37 °C with a percentage comparable to that observed in 2 M GdmCl. At 42 °C, the fraction of intact DNA origami nanostructures drops again to about 30 %. At first glance, this behavior suggests that DNA origami nanostructures partially denature at low temperature and subsequently re-establish their intramolecular interactions and thereby recover their shape at elevated temperature.

In 6 M GdmCl, about half of the DNA origami nanostructures stay intact between 23 and 30 °C. At 37 °C, however, the damage drastically increases with intact DNA origami being virtually absent. Notably, the DNA origami morphology under these conditions does not show any resemblance to the original triangular shape anymore but rather appears mostly melted. At 42 °C, any remaining indications of the original triangular superstructure have disappeared completely.

While GdmCl clearly exerts denaturing effects on the DNA origami, the influence of Gdm₂SO₄ is markedly different. Sulfate anions have been shown to stabilize proteins⁵³ and an analogous stabilizing effect is also seen for the DNA origami triangles in Figure 4.5. However, the overall situation appears surprisingly complex. In 2 M Gdm⁺, corresponding to 1 M Gdm₂SO₄, more than 80 % of the DNA origami nanostructures are structurally intact at 23 °C and 30 °C (see Figure 4.6). At 37 °C, however, the fraction of intact DNA origami decreases to about 62 %. Upon increasing the temperature further to 42 °C, the fraction of intact DNA origami nanostructures drops to only about 18 %. This is in stark contrast to the behavior seen for GdmCl in Figure 4.4, where the fraction of intact DNA origami in 2 M GdmCl never drops below 40 %. This illustrates impressively the importance of the counteranions in modulating

the efficiency of Gdm^+ -induced DNA origami denaturation. However, despite this astonishingly small fraction of intact DNA origami, the corresponding AFM image in Figure 4.5 shows surprisingly little damage to the individual DNA origami nanostructures, which is mostly comprised of disrupted vertices and partially damaged trapezoids resulting in an overall deformation of the triangular shape.

For Gdm_2SO_4 at 4 M Gdm^+ , the denaturation at intermediate temperatures becomes more pronounced. At 23 °C and 30 °C, about 85 % intact DNA origami nanostructures are observed, whereas this value decreases to 25 % at 37 °C. Increasing the temperature to 42 °C does not result in a further decrease of intact DNA origami. However, the corresponding AFM images in Figure 4.5 reveal a slight depletion of DNA origami adsorbed at the mica surface.

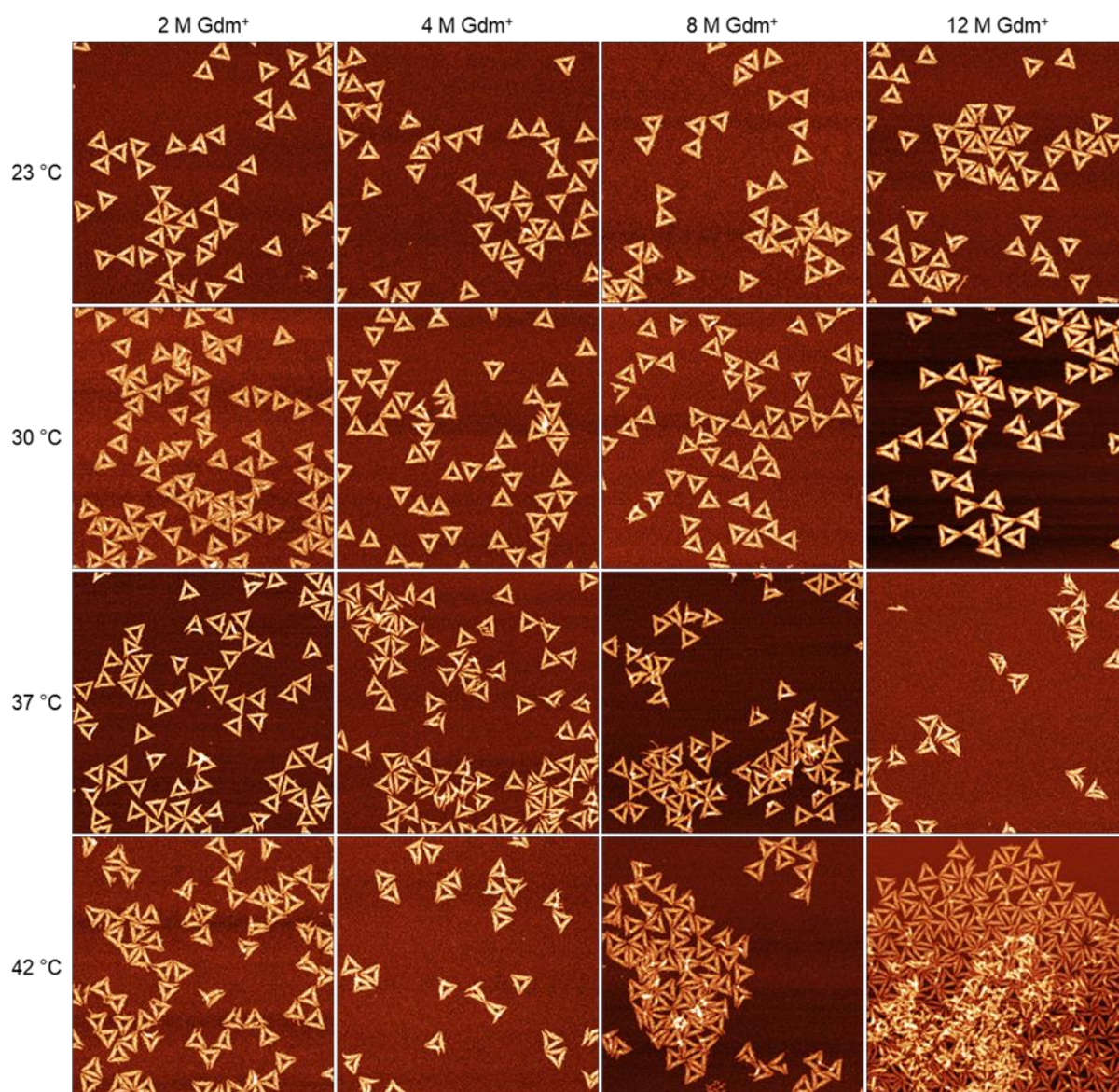


Figure 4.5 AFM images of DNA origami triangles deposited on mica after 1 h incubation in Gdm_2SO_4 at different Gdm^+ concentrations and temperature conditions. All images have a size of $1.5 \times 1.5 \mu\text{m}^2$. The color range was set to automatic with tails cut off.¹³⁶

At a Gdm^+ concentration of 8 M, the observed damage is similar to that of 2 M. More than 80 % of the DNA origami nanostructures are intact at 23 °C and 30 °C, while at 37 °C and 42 °C, this value drops to about 20 % and 28 %, respectively. Strikingly, the original triangular shape can still be identified for all DNA origami nanostructures and no DNA origami melting is observed at all (see Figure 4.5). Even at 12 M Gdm^+ , more than 80 % of the DNA origami remain intact at 23 °C. This is again in striking contrast to the case of 6 M GdmCl , where 50 % of the DNA origami are damaged at this temperature (see Figure 4.4). At 37 °C, the fraction of intact DNA origami nanostructures drops to less than 10 %. Surprisingly, at 42 °C, this value recovers to about 30 %.

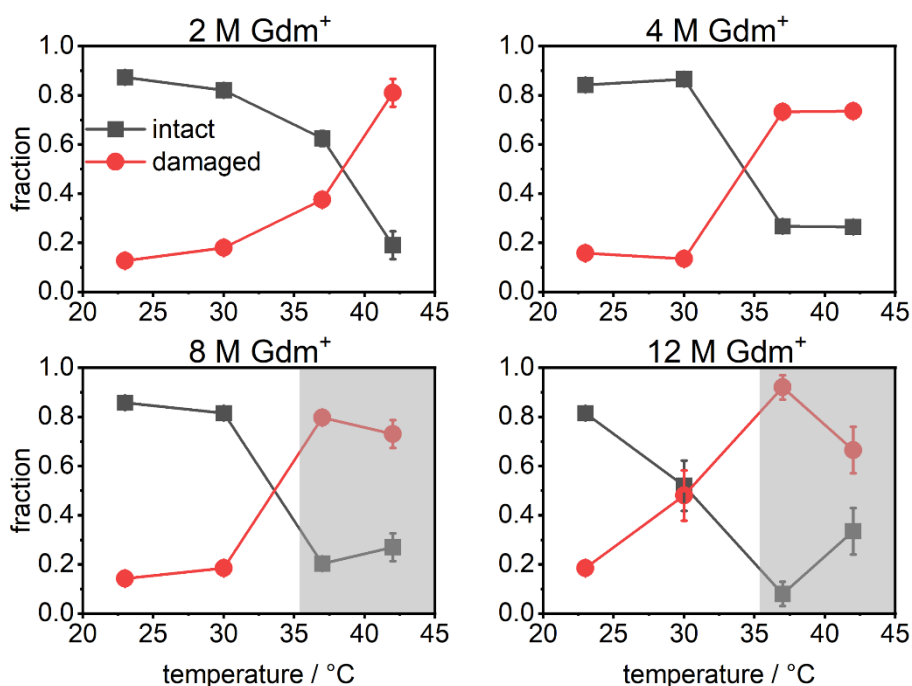


Figure 4.6 Mean fractions of intact and damaged DNA origami triangles after 1 h incubation in Gdm_2SO_4 at different Gdm^+ concentrations and incubation temperatures. Values represent averages over at least three AFM images with standard deviations given as error bars. The shaded areas indicate the occurrence of DNA origami clustering.

Close evaluation of the AFM images recorded for Gdm_2SO_4 at 8 M and 12 M Gdm^+ in Figure 4.5 reveals that the DNA origami nanostructures show a tendency to form clusters at the mica surface. This clustering is getting more pronounced with increasing temperature, resulting in large agglomerates at 37 °C and 42 °C, respectively. Intriguingly, the observed clusters seem to consist mostly of intact DNA origami. However, overlapping and multilayer formation makes it very challenging to identify and count the damaged and intact DNA origami triangles inside the clusters, so that the corresponding fractions given in Figure 4.6 (shaded areas), may over- or underestimate species since they are mostly based on isolated DNA origami outside the clusters. This tendency of the DNA origami nanostructures to form clusters in Gdm_2SO_4 probably results from the salting-out effect of the kosmotropic SO_4^{2-} anions.¹³⁷ Salting-out of biomolecules occurs when added salt ions neutralize charges at the biomolecule surface and dehydrate hydrophobic surface patches, thereby triggering biomolecular aggregation and precipitation. Kosmotropic ions such as SO_4^{2-} are particularly efficient in this regard and it was recently shown that also DNA origami nanostructures can be salted out by high concentrations of $(\text{NH}_4)_2\text{SO}_4$.¹³⁷

4.1.2.2 Discussion

It was shown that the anions Cl^- and SO_4^{2-} exert surprisingly distinct effects on the thermal stability of DNA origami in the presence of Gdm^+ . Already below the global melting temperature T_m , ex-situ AFM measurements revealed different stability modulations by the two anions on the superstructure of the DNA origami triangles.

In addition, a thermodynamic model was derived to describe the thermal denaturation of Gdm^+ -bound DNA origami triangles, indicating an intermediate pre-melting state of the DNA before the main melting transition. The altered Gdm denaturation modulation via both anions Cl^- and SO_4^{2-} is explained by different heat capacity changes. Furthermore, MD simulations, performed at Helmholtz-Zentrum Dresden-Rossendorf in the group of Prof. Dr. Fahmy, have shown for GdmCl more water-like and less charged hydration shell structures in contrast to Gdm_2SO_4 forming ion pairs in the solution. Hence, Gdm^+ from GdmCl increases the number of ordered low entropy water networks around the DNA origami much more significantly compared to Gdm_2SO_4 leading to substantial heat capacity changes.¹³⁶

4.1.2.3 Conclusion

It has been shown that DNA origami thermally denature in a complicated manner in the presence of Gdm-salts. It appears to originate in the more water-like and less charged hydration shell structures in GdmCl and the lack of ion pairing as compared to Gdm₂SO₄. Thereby, under the overall water-limited solvation conditions at 4 M Gdm⁺, the transfer of the denaturing cation from solvent to DNA upon heating increases the number of ordered low entropy water networks around the DNA origami much more for the chloride than the sulfate counter ion.¹³⁶

The data suggest that the supramolecular structure of a DNA origami amplifies subtle steric effects by their accumulation over the large number of linked dsDNA segments. While similar amplification effects have recently been found also in DNA origami degradation by UV irradiation¹³⁸ and reactive oxygen species,¹³⁹ this is the first time that such a behavior could be observed not only at the nanostructural but also at the molecular level.¹³⁶ Therefore, in combination with the thermodynamic analysis, geometric, energetic, and hydration effects accompanying DNA-ligand interactions may find a novel sensitive nanoscopic and thermodynamic readout.¹³⁶

4.1.3 Materials and methods

4.1.3.1 DNA origami synthesis

The synthesis of the DNA origami triangles⁴ was based on a previously published protocol.²⁶ To this end, M13mp18 scaffold (Tilibit) and about 200 staple strands (Eurofins) were mixed at a molar ratio of 1:10 in 10 mM Tris buffer (Sigma-Aldrich) containing 10 mM MgAc₂ (Sigma-Aldrich). The pH was adjusted to 8.0 with acetic acid. DNA origami assembly was performed during slow cooling from 80 °C to room temperature over 90 min using a Primus 25 advanced thermocycler (PEQLAB). Then, the DNA origami were purified by PEG precipitation. For this purpose, 200 µl of DNA origami solution were diluted in 600 µl Tris/MgAc₂ buffer and mixed with 800 µl PEG solution containing 1x TAE (Roth), 15 % PEG-8000 (w/v) (Sigma-Aldrich) and 505 mM NaCl (Sigma-Aldrich). This solution was centrifuged using a VWR microcentrifuge at 14,000 rcf for 30 min at 18 °C, after which the supernatant was carefully removed with a pipette. The precipitate was re-dissolved in about 30 µl Tris/MgAc₂ buffer overnight. The DNA origami concentration of the resulting solution was determined using an Implen Nanophotometer P330 and adjusted to 100 nM with Tris/MgAc₂ buffer.

4.1.3.2 AFM imaging and analysis

GdmCl solution (8 M) and Gdm₂SO₄ salt were purchased from Sigma-Aldrich. Gdm₂SO₄ salt was dissolved in HPLC-grade water (VWR) to reach a concentration of 8 M. For each experiment, stock solutions of GdmCl and Gdm₂SO₄ were mixed with Tris/MgAc₂ buffer and DNA origami triangle stock solution to reach final Gdm⁺ salt concentrations of 1 M, 2 M, 4 M, and 6 M at a constant DNA origami concentration of 5 nM. 100 µl samples of the resulting solutions were incubated for 1 h at different temperatures (23 °C, 30 °C, 37 °C, 42 °C) using a Primus 25 advanced thermocycler.

After 1 h of incubation, 1 µl of sample solution was deposited on freshly cleaved mica, covered with 50 µl of Tris/ MgAc₂ buffer, and incubated for 5 min. Then, the sample was rinsed with about 6 ml of HPLC-grade water and dried in a stream of ultra-pure air. AFM imaging was performed in air using a Bruker Dimension ICON in ScanAsyst PeakForce Tapping mode with ScanAsyst-Air cantilevers (Bruker) or an Agilent 5100 in intermittent contact mode with HQ:NSC18/Al BS cantilevers (MikroMasch).

For the statistical analyses, approx. 300-600 DNA origami nanostructures from at least three AFM images taken at different positions on the surfaces of up to three independent samples were analyzed for each experimental condition using Adobe Photoshop software. The DNA origami nanostructures visible in the AFM images were classified either as intact or damaged based on visual evaluation of their shape as previously described.^{22,140} In particular, any DNA origami shape that visibly deviated from a perfectly assembled triangle was considered damaged, even if the deviation was comparably small such as a partially ruptured vertex. The relative fractions of intact and damaged DNA origami nanostructures were determined by manually counting the absolute numbers of each species visible in each AFM image. The so determined fractions per AFM image were then averaged over at least three AFM images per condition. Fractions are presented as mean values with standard deviations as error bars.

4.2 Time-Dependent DNA Origami Denaturation by Guanidinium Chloride, Guanidinium Sulfate, and Guanidinium Thiocyanate

4.2.1 Introduction

The work in chapter 4.1 revealed that the counteranion species in particular have a surprisingly strong influence on the denaturant activity of Gdm^+ . Using a combination of *ex-situ* AFM and *in-situ* circular dichroism spectroscopy, a thermodynamic model of DNA origami denaturation by GdmCl and Gdm_2SO_4 was derived based on principle component analysis (PCA) and iterative target test factor analysis (ITTFA).¹³⁶ The results showed that Gdm^+ -induced DNA origami denaturation proceeds via three successive state transitions involving an intermediate pre-melting state. Remarkably, this complex denaturation was further found to be driven by heat capacity changes, which are modulated by the counteranions via altered wetting properties of the hydrophobic DNA surface regions and in particular in the grooves. This was attributed to the presence of more water-like and less charged hydration shells in GdmCl and the more pronounced ion pairing in Gdm_2SO_4 , in accordance with MD simulations. Transfer of Gdm^+ from GdmCl bulk solution to the DNA base stack upon heating thus results in a stronger increase in the number of ordered low entropy water networks around the DNA origami nanostructures compared to Gdm_2SO_4 .¹³⁶

In this work, previous investigations were extended and focused on the time dependence of DNA origami denaturation by GdmCl , Gdm_2SO_4 , and guanidinium thiocyanate (GdmSCN). These three counterion pairings of the chaotropic Gdm^+ cation cover the whole range of the anionic Hofmeister series⁴⁸ (see Figure 2.4 a)). Here, SO_4^{2-} is located at the kosmotropic end, whereas Cl^- is found in the middle. SCN^- on the other hand is the most chaotropic anion in the Hofmeister series, which is reflected in the exceptionally strong denaturant activity of the chaotropic-chaotropic ion pair GdmSCN .^{53,141} The effect of these three Gdm salts on the structural integrity of DNA origami triangles is assessed in 2 M solutions of the salts at different temperatures in 15 min intervals by *ex-situ* AFM over a time course of 90 min. In general, it was found that GdmSCN is the most potent DNA origami denaturant, which already at this comparably low concentration can cause complete DNA origami denaturation. Furthermore, while under moderately to strongly denaturing conditions, DNA origami denaturation occurs within the first 15 min of Gdm^+ exposure, much slower DNA origami denaturation is observed under weakly denaturing conditions such as for Gdm_2SO_4 at 25 °C. Finally, by choosing a wider

temperature range, it was able to observe a novel non-monotonic temperature dependence of DNA origami denaturation in Gdm_2SO_4 with the fraction of intact DNA origami nanostructures having an intermediate minimum at a temperature around 40 °C. The results thus highlight the complexity of the Gdm^+ -DNA interaction and underscore the importance of the counteranion species, which may lead to complex and unexpected time and temperature dependencies of the Gdm^+ -induced DNA origami denaturation.

4.2.2 Results

4.2.2.1 Guanidinium Chloride (GdmCl)

For investigating the time dependence of DNA origami denaturation in the different Gdm salts, DNA origami triangles⁴ were exposed to comparably low Gdm salt concentrations of 2 M. The Rothemund triangle is one of the most studied DNA origami nanostructures, in particular with regard to its stability under various conditions,^{13,15,17,19,22,23,28,43,45,137,138,140,142–146} including the presence of molar concentrations of Gdm salts.^{25,26,136} It is composed of three trapezoids of parallel double helices that are connected to each other via one scaffold crossover and four bridging staples. For exposure to 2 M GdmCl, only in low to moderate fractions of damaged DNA origami triangles have been observed in the temperature range between 23 and 42 °C.¹³⁶ However, in this work, the temperature range was slightly extended and AFM images of the DNA origami triangles were recorded after incubation at 25, 40, and 50 °C, respectively, in order to assess a broader dynamic range in the observable damage. As can be seen in the AFM images in Figure 4.7, intact DNA origami triangles can be observed for all temperatures and incubation times. Note that 0 min incubation refers to the freshly prepared samples at room temperature before incubation at the desired temperature (see section 4.2.3.2). Closer inspection reveals also some damaged triangles, which have come apart at the vertices due to dissociation of the short bridging staples that connect the three trapezoids^{25,43,136} (see white arrows in Figure 4.7). Note that this kind of damage is also observed in freshly assembled DNA origami triangles without any exposure to denaturing conditions.¹⁴⁰ Therefore, damaged DNA origami nanostructures appear rather rarely at 0 min, whereas they seem to become more prominent at longer incubation times, in particular at 50 °C.

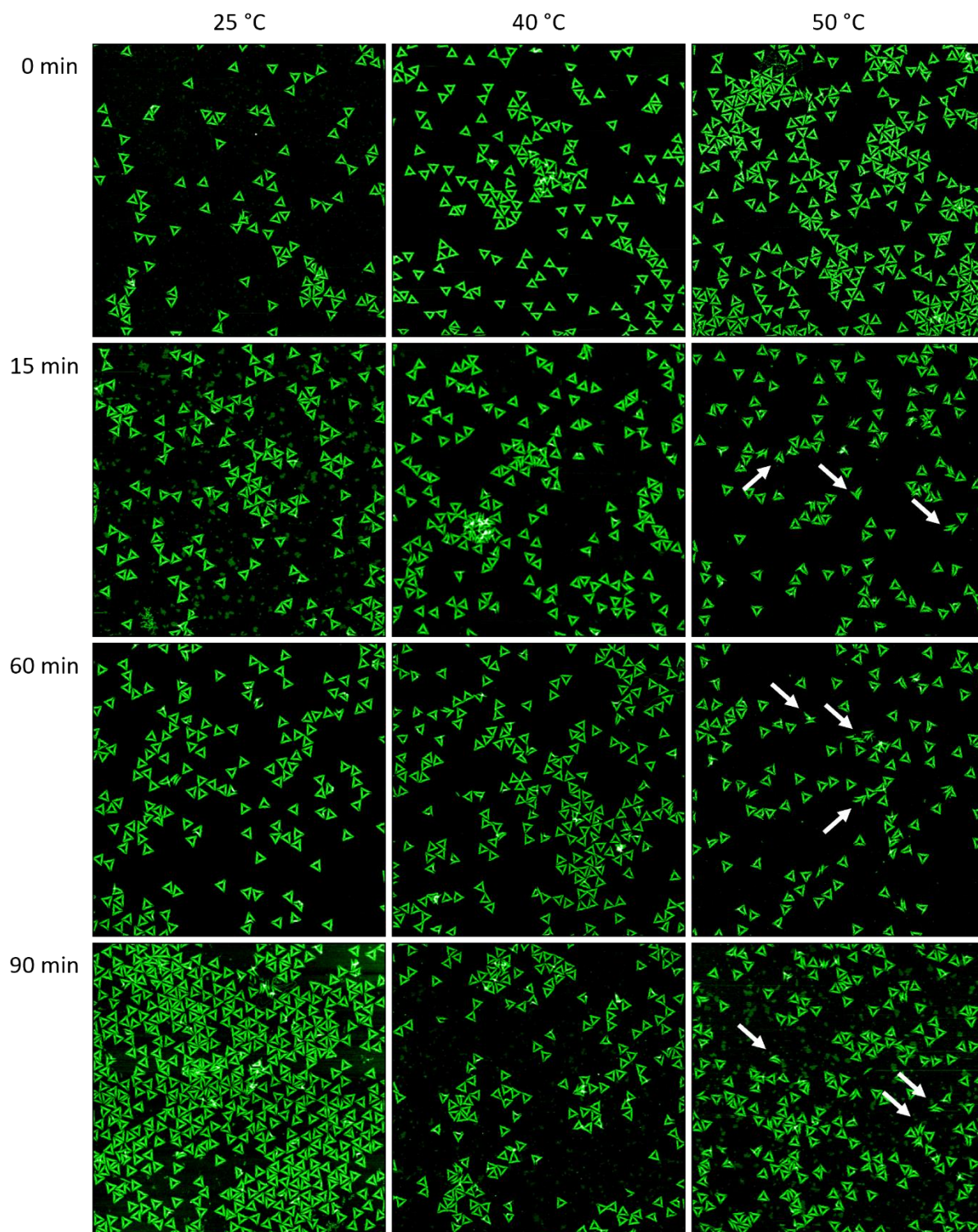


Figure 4.7 AFM images of DNA origami triangles after incubation in 2 M GdmCl at different times and temperatures. Images have a size and height scale of $3 \times 3 \mu\text{m}^2$ and 2.5 nm, respectively. The white arrows indicate collapsed triangles that disintegrated by rupture at the vertices.

These qualitative observations are further substantiated in the results of the statistical analyses of the AFM images shown in Figure 4.8. Here, the fractions of intact and damaged DNA origami are plotted as a function of incubation time for all three temperatures. The fractions were determined by manual counting with the classification “damaged” applying to all DNA origami nanostructures with compromised triangular shapes, ranging from triangles with a single ruptured vertex to completely disintegrated structures. For all three temperatures, an initial decrease in the fraction of intact DNA origami within the first 15 min of incubation were observed. At 25 °C, the fraction of intact DNA origami drops only slightly from initially about 80% to about 65%, while larger drops to about 60% and less than 40% are observed for 40 and 50 °C, respectively. This general trend agrees fairly well with previously reported observations.¹³⁶ For incubation times exceeding 15 min, the fractions of intact DNA origami nanostructures remain more or less constant but show some random fluctuations that can be attributed to sample-to-sample variations. At a temperature of 50 °C, an additional drop in the fraction of intact DNA origami is observed between 75 and 90 min incubation. However, since this drop has a similar magnitude as the maximum variation observed in the 25 °C data at intermediate times, this behavior can be attributed to random fluctuations as well and not to the onset of a second, late-stage denaturation phase.

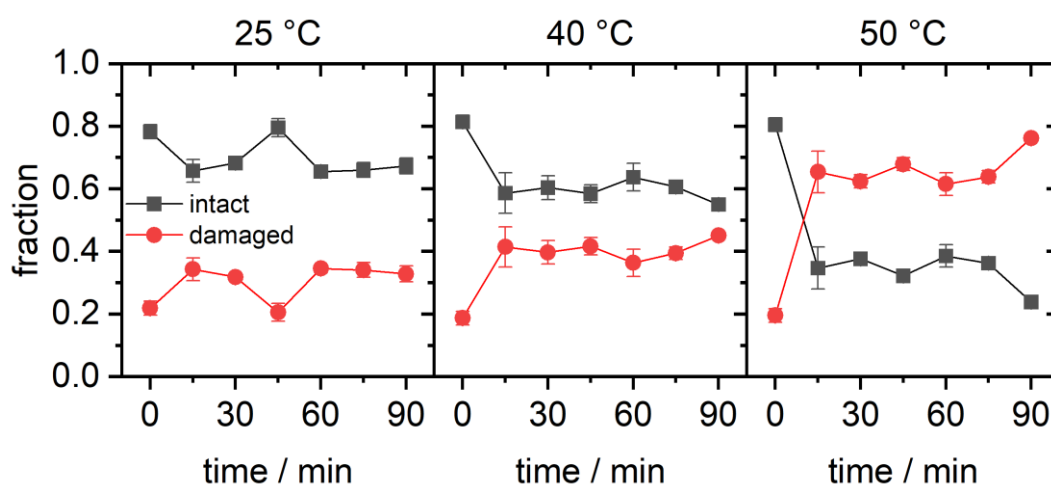


Figure 4.8 Results of the statistical analysis of the AFM images for 2 M GdmCl. Each data point represents the average of three AFM images with the standard deviations given as error bars.

Summing up the observations for GdmCl, it seems that under the chosen conditions, DNA origami damage occurs mostly within the first 15 min of GdmCl exposure. Longer incubation times up to 90 min result neither in more damaged DNA origami nor in more severe damage. The observed degree of DNA origami damage is comparably low and mostly consists of ruptured vertices of the DNA origami triangles, while the trapezoids remain almost completely intact. Furthermore, the fraction of damaged DNA origami nanostructures increases with temperature. All this is in fair agreement with previous investigations.^{25,136}

4.2.2.2 Guanidinium Sulfate (Gdm₂SO₄)

Gdm₂SO₄ is more complex in its effect on DNA origami nanostructures, as it pairs the chaotropic Gdm⁺ cation with the kosmotropic SO₄²⁻ anion.¹³⁶ As can be seen in Figure 4.9, a rather similar behavior as for GdmCl is observed, with moderate DNA origami damage. This is rather remarkable considering that at a salt concentration of 2 M, the concentration of the denaturing Gdm⁺ cations is twice as high as for GdmCl. Also, the apparent time dependencies and the type of damage are similar to the case of GdmCl. In particular, almost all damaged DNA origami triangles have ruptured vertices but intact trapezoids.

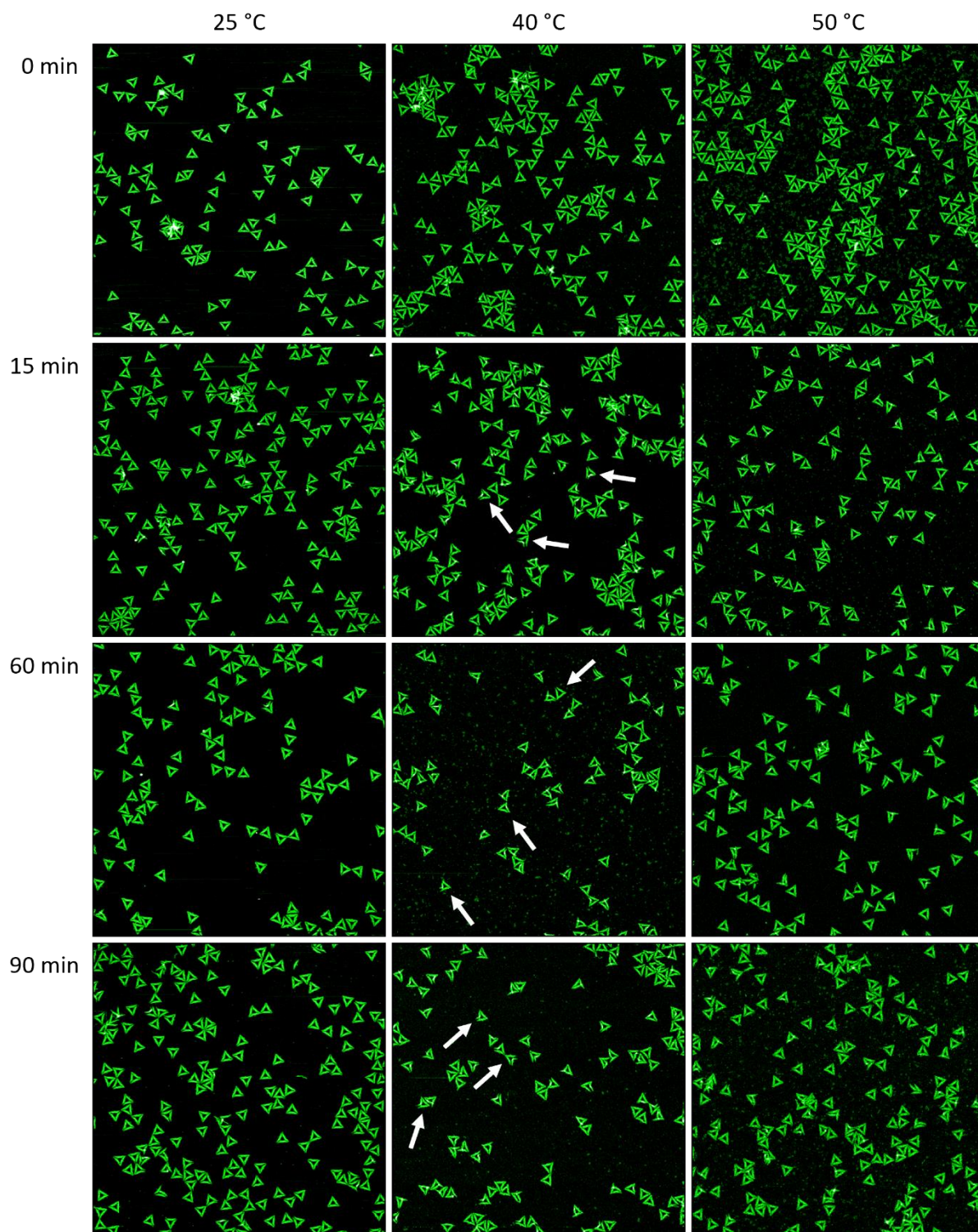


Figure 4.9 AFM images of DNA origami triangles after incubation in 2 M Gdm₂SO₄ at different times and temperatures. Images have a size and height scale of 3 x 3 μm² and 2.5 nm, respectively. The white arrows indicate damaged yet mostly intact triangles with one or two ruptured vertices.

Despite all those qualitatively similar observations, the results of the statistical analyses shown in Figure 4.10 reveal some rather astonishing differences. At 25 °C, a weak yet rather continuous decrease in the fraction of intact DNA origami triangles from about 85 % at 0 min to about 75 % at 75 min were observed. Then, however, the fraction suddenly drops to about 45 %. Since this is a rather large drop compared to the random fluctuations observed in this and the other data sets, it indeed indicates the onset of a second and more drastic denaturation regime. At the other temperatures of 40 °C and 50 °C, different time dependencies are observed that show only a large initial drop in the fraction of intact DNA origami triangles between 0 and 15 min, while at longer incubation times, the fraction saturates and displays only random fluctuations.

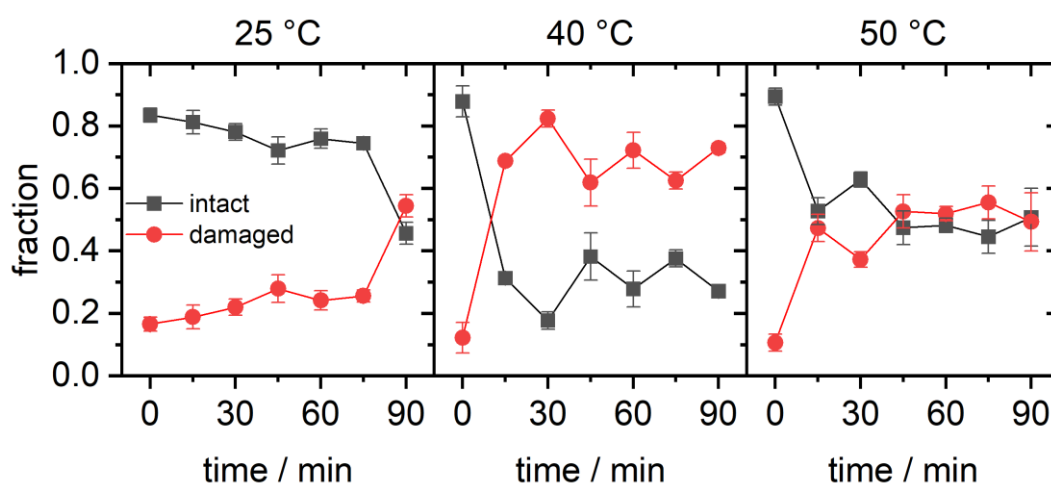


Figure 4.10 Results of the statistical analysis of the AFM images for 2 M Gdm₂SO₄. Each data point represents the average of three AFM images with the standard deviations given as error bars.

Another interesting feature visible in the plots of Figure 4.10 is the apparent non-monotonic temperature dependence. At 25 °C the final value of the fraction of intact DNA origami at 90 min incubation is 46 %. Increasing the temperature to 40 °C results in a fraction of intact DNA origami triangles of only 29.7 % ± 1.9 % (averaged over all data points between 15 and 90 min). Such a decrease is to be expected upon an increase in temperature and consistent with previous observations.¹³⁶ However, upon increasing the temperature further to 50 °C, the average value of the fraction of intact DNA origami recovers to 53.3 % ± 3.3 %. Here, the actual degree of damage is essentially the same as at 40 °C, there are only fewer DNA origami

triangles with ruptured vertices observed at 50 °C. While such a non-monotonic temperature dependence is rather counterintuitive, a similar behavior have already been observed for GdmCl.¹³⁶

From these experiments, it can be concluded that rapid DNA origami denaturation within the first 15 min of incubation is a common feature in both GdmCl and Gdm₂SO₄, at least under moderately to strongly denaturing conditions. Under weakly denaturing conditions such as 2 M Gdm₂SO₄ at 25 °C, however, denaturation occurs more slowly over a time course of more than one hour. Furthermore, a non-monotonic dependence of DNA origami denaturation in Gdm₂SO₄ is observed, which extends previous observations made within a smaller range of temperatures.

4.2.2.3 Guanidinium Thiocyanate (GdmSCN)

As the third Gdm salt to be investigated in this study, GdmSCN was selected, which is well known as a strong protein denaturant that even exceeds GdmCl in its potency.^{53,141} This remarkable denaturant activity results from the pairing of the two strongly chaotropic ions, i.e., Gdm⁺ and SCN⁻, which are exceptionally weakly hydrated and thus interact very strongly with protein surfaces.¹⁴⁷ In accordance with this behavior, the AFM images in Figure 4.11 reveal strongly enhanced DNA origami denaturation compared to GdmCl and Gdm₂SO₄. Already at 25 °C, many collapsed triangles with ruptured vertices can be found (white arrows). In addition, some DNA origami have damaged trapezoids and even melted scaffold dangling from them (yellow arrows). Most notably, this kind of damage is already apparent at 0 min. At 40 °C, more severe damage is observed. For incubation of 15 min and beyond, virtually all DNA origami nanostructures are severely damaged and have a completely collapsed and partially melted appearance. Increasing the temperature further to 50 °C results in the complete denaturation of all the DNA origami triangles, so that only unstructured scaffold is found at the mica surface.

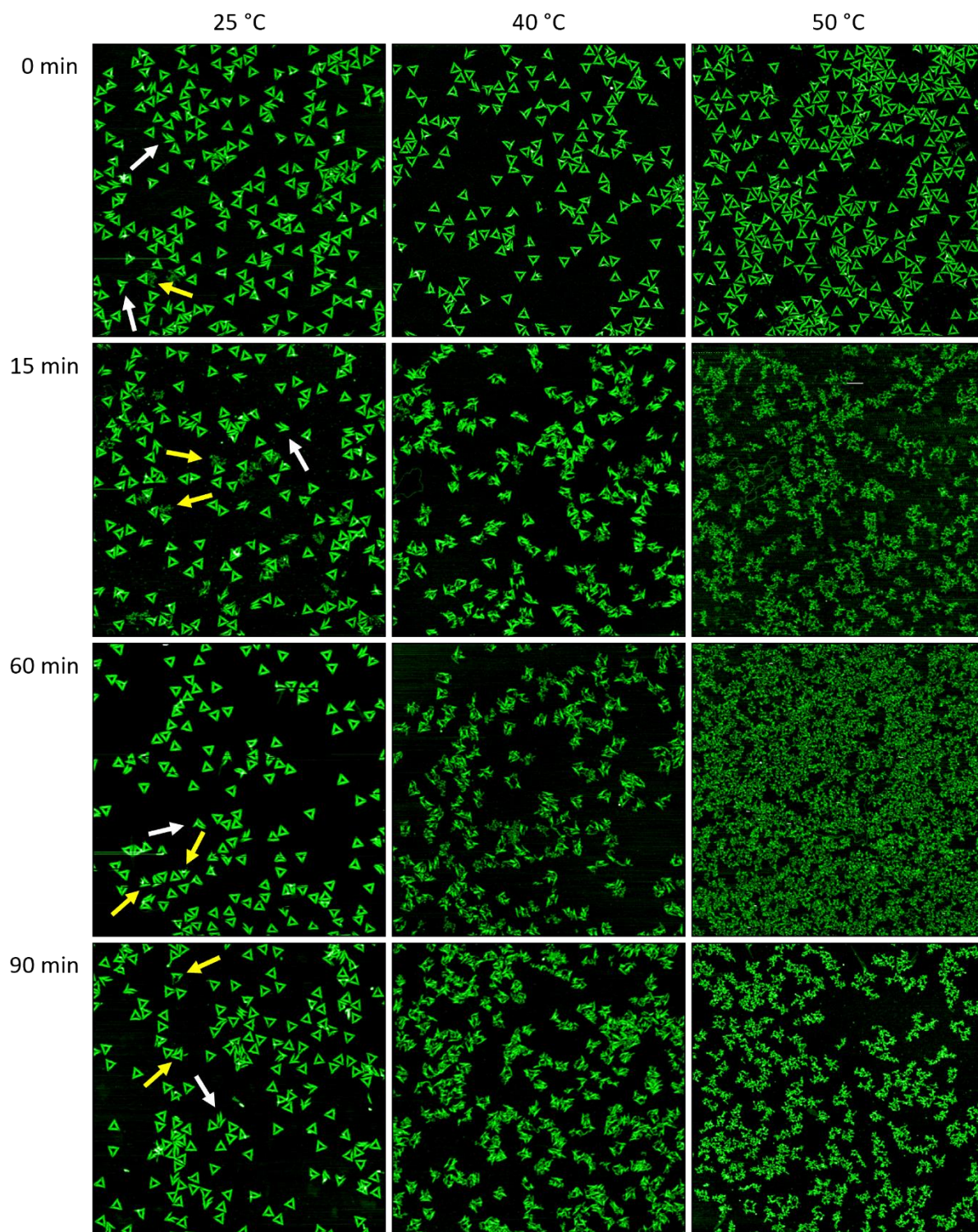


Figure 4.11 AFM images of DNA origami triangles after incubation in 2 M GdmSCN at different times and temperatures. Images have a size and height scale of $3 \times 3 \mu\text{m}^2$ and 2.5 nm, respectively. The white arrows indicate collapsed triangles with ruptured vertices and yellow arrows triangles with damaged trapezoids or dangling scaffold.

Interestingly, the results of the statistical analysis of the AFM images shown in Figure 4.12 reveal that the fraction of intact DNA origami at 25 °C remains roughly constant during the whole-time course of the experiment and fluctuates around a value of about 46 %. This is rather remarkable since for all experiments with GdmCl and Gdm₂SO₄ described above, fractions of intact DNA origami of about 80 to 90 % are obtained at 0 min incubation. In contrast, exposure to GdmSCN results in an immediate destabilization of DNA origami structure at room temperature. Further incubation at 25 °C does not appear to lead to additional denaturation. At both 40 °C and 50 °C, however, incubation for additional 15 min results in the fraction of intact DNA origami dropping to 0 %.

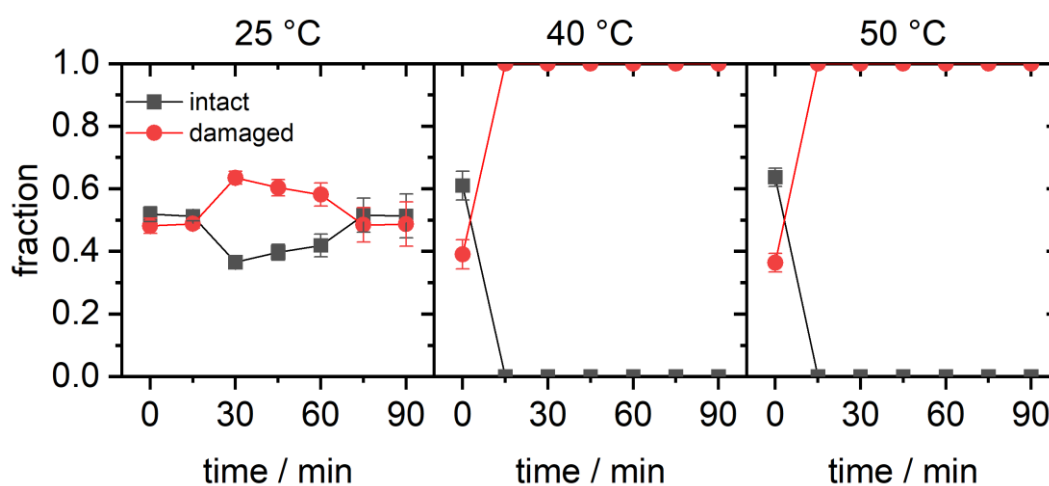


Figure 4.12 Results of the statistical analysis of the AFM images for 2 M GdmSCN. Each data point represents the average of three AFM images with the standard deviations given as error bars.

4.2.2.4 Discussion

Figure 7 directly compares the fractions of intact DNA origami nanostructures during exposure to the different Gdm salts as a function of incubation time. As can be seen, for all temperatures investigated in the present work, GdmSCN is the strongest DNA origami denaturant, which is in agreement with its known effect on protein structure.^{53,141,147} In particular, exposure to GdmSCN results in immediate denaturation, so that a strongly reduced fraction of intact DNA origami is observed already at 0 min. Most remarkably, GdmSCN furthermore is the only salt that achieves complete melting of the DNA origami triangles at a concentration as low as 2 M. This is seen in the AFM images in Figure 4.11, which show only unstructured scaffold after

15 min incubation at 50 °C, whereas after incubation under equivalent conditions in the other salts, many intact triangles can still be observed (see Figures 4.7 and 4.9). In GdmCl, complete DNA origami denaturation has been observed so far only at a concentration of 6 M and incubation temperatures of 37 °C or higher,²⁵ which demonstrates the high denaturant activity of GdmSCN already at comparably low concentrations. This makes GdmSCN a promising candidate for applications that require efficient DNA origami denaturation at low temperatures, for instance in molecular lithography.^{130,131}

With regard to the time dependence of DNA origami denaturation, it appears that most denaturation occurs within the first 15 min of incubation, after which the induced DNA origami damage saturates in terms of both the fraction of damaged DNA origami and the degree of damage. The only exception from this behavior is observed for Gdm₂SO₄ at 25 °C. Under such weakly denaturing conditions, the fraction of intact DNA origami triangles decreases only weakly during the first 75 min, after which a sudden drop from about 75 % to about 45 % occurs. The data suggest the gradual build-up of unstacked duplexes and dissociated base pairs in the DNA origami, which upon reaching a certain threshold results in the sudden collapse of the DNA origami shape, mostly by dissociation at the particularly vulnerable edges.^{25,43} Indeed, close inspection of the corresponding AFM image in Figure 4.9 reveals that the vast majority of damaged triangles under this condition have one or two dissociated vertices but intact trapezoids. Under more strongly denaturing conditions, this accumulation of damage seems to happen much faster, so that the maximum degree of damage is observed already after 15 min of incubation.

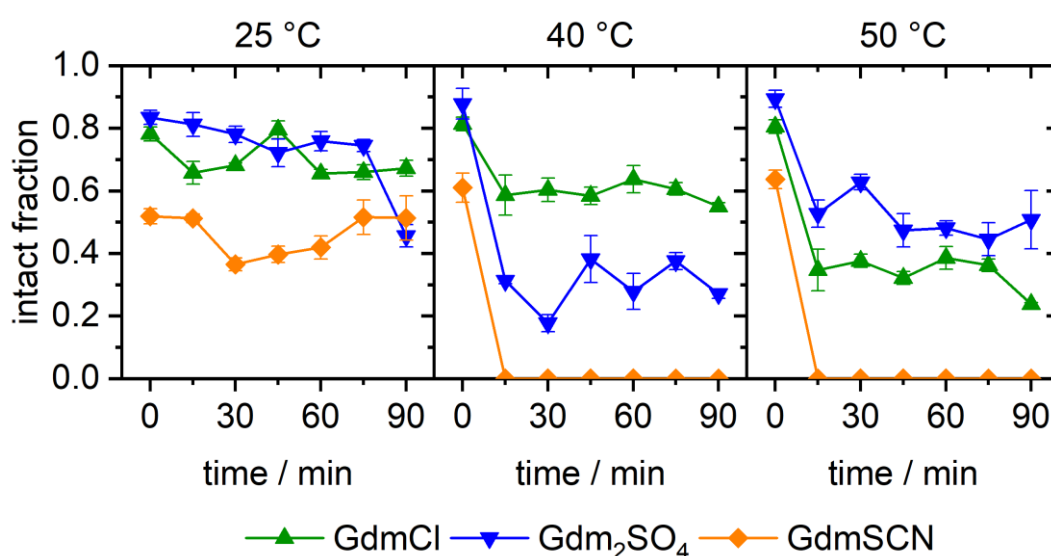


Figure 4.13 Comparison of the fractions of intact DNA origami triangles obtained in the different Gdm salts at different temperatures and as a function of incubation time.

Finally, different dependencies of DNA origami denaturation on incubation temperature are observed for the different salts. For GdmCl and GdmSCN, the fraction of intact DNA origami decreases with increasing temperature. For 2 M GdmCl, this observation is in fair agreement with previously reported results.^{25,136} For Gdm₂SO₄, however, a non-monotonic temperature dependence is observed, in which the fraction of intact DNA origami first decreases with temperature in the range from 25 °C to 40 °C, after which it increases again between 40 °C and 50 °C. A non-monotonic temperature dependence of the fraction of intact DNA origami has previously been observed for 4 M GdmCl, where an increase was observed between 23 °C and 30 °C, followed by a decrease between 37 °C and 42 °C. This was explained by DNA origami denaturation in Gdm salts being governed by heat capacity changes, with the free enthalpy of reaction becoming a non-monotonic function of temperature, and could be reproduced with a thermodynamic model¹³⁶. The current results for 2 M Gdm₂SO₄, however, do not agree with the predictions of this model, which was derived based on previous experimental observations. Even though the initial decrease in the fraction of intact DNA origami between 25 °C and 40 °C is well reproduced, the model also predicts that the intact fraction will monotonically decrease with increasing temperature.¹³⁶ This discrepancy might be caused by the limited temperature range of the AFM investigations of 23 to 42 °C, which was used to prime the analysis of the CD spectra and derive a thermodynamic model of Gdm⁺ denaturation. In addition, the CD spectra were recorded within a temperature ramp, which is very different from the isothermal conditions used in the present study. However, further investigations are needed to resolve this issue, in particular at a wider temperature range and while considering temperature-specific variations in denaturation kinetics.

In summary, the results underscore the exceptionally high complexity of DNA origami denaturation in Gdm salts and highlight the necessity of more detailed experimental and theoretical studies that explore the complete parameter space of the underlying reactions. Furthermore, future studies should also assess possible influences of DNA origami shape, superstructure, and local and global design features. While several previous studies found that such factors may dramatically alter the interactions between the DNA origami nanostructures and various molecules and cations,^{22–24,28,86,137,142,143,148} similar superstructure-dependent

effects in DNA origami denaturation by Gdm salts are largely unexplored. Nevertheless, based on the mentioned studies, a strong influence of DNA origami shape and superstructure also on the denaturing effect of Gdm salts has to be considered. This in particular concerns bulky 3D DNA origami nanostructures, which have previously been found to be more sensitive toward ion binding effects because of their dense packing of helices and the associated higher importance of electrostatic repulsion between neighboring core helices.²² It can only be speculated, however, whether these differences in the electrostatic interactions will influence also any anion-specific effects. Finally, while previous studies have demonstrated that GdmCl denaturation of DNA origami nanostructures shows rather different effects and dependences than urea denaturation,^{25,26} it remains to be seen whether these effects and dependencies are also observed for other chaotropic salts such as other thiocyanate or tetrapopylammonium salts.

4.2.3 Materials and methods

4.2.3.1 DNA Origami Synthesis and Purification

DNA origami triangles⁴ were assembled as previously described¹³⁶ using the 7249 nt M13mp18 scaffold (Tilibit GmbH, München, Germany) and about 200 staple strands (Eurofins Genomics GmbH, Ebersberg, Germany) in 10 mM Tris buffer (Sigma-Aldrich Chemie GmbH, Taufkirchen, Germany) containing 10 mM MgAc₂ (Sigma-Aldrich Chemie GmbH, Taufkirchen, Germany). The pH of the Tris buffer was adjusted to 8.0 with acetic acid (Merck KGaA, Darmstadt, Germany). After thermal annealing in a Primus 25 advanced thermocycler (PEQLAB Biotechnologie GmbH, Erlangen, Germany), the DNA origami triangles were purified by PEG precipitation.¹³⁶ The precipitate was redissolved in Tris/MgAc₂ buffer overnight, after which the DNA origami concentration was determined using an Implen Nanophotometer P330 (Implen GmbH, München, Germany) and adjusted to 100 nM with Tris/MgAc₂ buffer.

4.2.3.2 Guanidinium Exposure

100 µl samples were prepared by mixing 9.5 µl of 100 mM Tris buffer containing 100 mM MgAc₂, 5 µl of 100 nM DNA origami solution, and 85.5 µl of 2.34 M Gdm salt solution to yield a DNA origami and Gdm salt concentration of 5 nM and 2 M, respectively. GdmCl and

Gdm₂SO₄ solutions were prepared by dissolving dry GdmCl ($\geq 99.5\%$, VWR International S.A.S., Fontenay-sous-Bois, France) and Gdm₂SO₄ (99%, Sigma-Aldrich Chemie GmbH, Taufkirchen, Germany) in HPLC-grade water (VWR International S.A.S., Fontenay-sous-Bois, France). For GdmSCN, a 6 M solution ($\geq 99\%$, Sigma-Aldrich Chemie GmbH, Taufkirchen, Germany) was diluted with HPLC-grade water to the desired concentration of 2.34 M. The samples were vortexed and incubated for 90 min at the desired temperature using a thermocycler PEQLAB Primus 25 advanced. At 15 min intervals, 1 μ l aliquots were removed from the samples and deposited immediately on freshly cleaved mica. After addition of 100 μ l 10 mM Tris/MgAc₂ buffer, which is supposed to prevent any further denaturation, the DNA origami were left to adsorb for 5 min, after which the mica surfaces were rinsed with 12 ml HPLC-grade water and dried in a stream of ultrapure air. For each sample, an additional aliquot was analyzed at 0 min incubation, i.e., directly after mixing the DNA origami with the Gdm salts at room temperature and before heating them to the desired temperature.

4.2.3.3 AFM Imaging

The dry samples were imaged in air using a Bruker Dimension ICON (Bruker France S.A.S., Wissembourg, France) in ScanAsyst Peak-Force Tapping mode with ScanAsyst-Air cantilevers (Bruker AFM Probes, Camarillo, CA, USA) and a JPK Nanowizard III (JPK Instruments, Berlin, Germany) in intermittent contact mode with HQ:NSC18/Al BS cantilevers (MikroMasch, Wetzlar, Germany), respectively. The obtained AFM images were flattened and height-adjusted using Gwyddion 2.52 open-source software.¹⁴⁹

4.2.3.4 Quantification and Statistical Analysis

The fractions of intact and damaged DNA origami triangles visible in the AFM images were determined by visual inspection and manual counting as previously described.^{22,140} For each data point in Figures 4.7, 4.9, and 4.11, three images (3 x 3 μ m²) recorded at different positions on the mica surface were analyzed, with the total number of DNA origami per data point ranging from 225 to 1297. Mean values and standard deviations were computed using OriginPro 2020 (OriginLab Corporation, Northampton, MA, USA).

4.3 Superstructure-dependent stability of DNA origami nanostructures in the presence of chaotropic denaturants

4.3.1 Introduction

The work in chapter 4.1 and 4.2 relied on the investigation of the interaction of 2D DNA origami nanostructures with Gdm salts and focused on the effects of different environmental parameters such as Gdm⁺ concentration, temperature, time, and counterion species. A surprisingly complex picture was revealed that included for instance strong counterion effects, and non-monotonic temperature dependencies.^{136,150} The origin of these observations lies in the structure of the Gdm⁺ cation (see Figure 4.14 g) and h). It consists of a single sp²-hybridized carbon atom with three NH₂ groups having a delocalized bond that leads to a planar hydrophobic face with the potential to participate in π interactions and to form hydrogen bonds. This renders Gdm⁺ a powerful protein denaturant with a complex mechanism of action that is still not completely understood.^{52,53,68,151}

In this work, it has been attempted to elucidate the impact of shape and superstructure on DNA origami stability and denaturation in the presence of different chaotropic salts. In this context, the term “superstructure” includes all design-specific parameters such as the selected lattice type, crossover arrangement, etc.

The protein denaturing activity of Gdm⁺ can be modulated by the counteranion it is paired with. Anions with low charge density and weak hydration properties such as Cl⁻ and SCN⁻ combined with Gdm⁺ show a high denaturant activity due to strong protein interactions (salting-in). In contrast, anions with high charge density and strong hydration properties, e.g., SO₄²⁻, interact more weakly with proteins and rather form ion pairs with Gdm⁺, which tends to stabilize protein structure (salting-out).^{52,53,68} While the propensity for salting-in and salting-out effects and therefore the protein denaturing activity of Gdm⁺ and other ions is reflected in the Hofmeister series,¹⁵² the interaction of Gdm⁺ salts with proteins is much more complex, involving dependencies on concentration and medium composition. Experimentally observed behaviors may thus deviate from the Hofmeister series.^{53,68}

Another chaotropic agent of high interest is tetrapropylammonium (TPA⁺) (see Figure 4.14 i)), which is used in numerous applications ranging from electrochemistry¹⁵³ to materials synthesis¹⁵⁴ to energy storage.¹⁵⁵ Furthermore, it is a well-known denaturant of both protein^{52,68,71} and DNA structure.^{156,157} TPA⁺ consists of a central nitrogen atom with four propyl

groups and has a strongly delocalized positive charge that is spread over the whole molecule. With its roughly tetrahedral shape, TPA^+ is substantially larger in size than Gdm^+ with the larger flat faces of the tetrahedron having aliphatic nonpolar surfaces.⁶⁸ Due to their rather different nonpolar hydrophobic properties, Gdm^+ and TPA^+ have quite different effects on protein structure, even though they are located near each other in the Hofmeister series.^{68,71} Whether such differences also exist in their interaction with DNA or DNA nanostructures, however, has not been investigated yet.

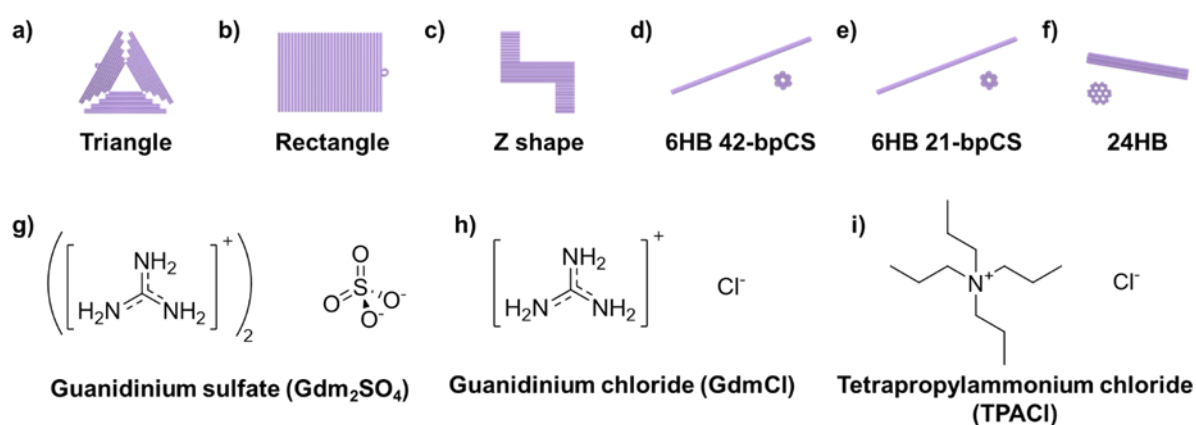


Figure 4.14 Schematic representations of the DNA origami nanostructures (a-f)) and the chaotropic salts (g-i)) used in this work. Reproduced with permission.¹⁵⁸ Copyright © 2023, The Royal Society of Chemistry.

Another issue unexplored so far is whether the denaturing effects of different chaotropic salts are also modulated by DNA origami superstructure. All previous studies investigated only one representative 2D DNA origami design, i.e., the so-called Rothemund triangle.^{25,26,136,150} However, it is well established that DNA origami stability under various conditions depends on the overall shape as well as certain design choices, e.g., lattice type and crossover arrangement.^{21–24} Therefore, in this work, the stability of six different DNA origami designs, i.e., the Rothemund triangle,⁴ the “tall” rectangle,⁴ a Z shape,²⁷ two six-helix bundles (6HBs) with different crossover spacings of 42 (42-bpCS) and 21 bp (21-bpCS),²⁴ and a 24-helix bundle (24HB)²⁸ (see Figure 4.14 a-f)) in the presence of three different chaotropic salts were investigated. Here, two Gdm^+ salts, i.e., Gdm_2SO_4 and GdmCl , as well as TPACl (see Figure 4.14 g-i)) were selected. While Gdm^+ and TPA^+ have a similar ranking in the Hofmeister series,

Cl^- and SO_4^{2-} differ in their behavior. While Cl^- is located in the middle of the Hofmeister series, SO_4^{2-} is a strongly hydrated anion found at the kosmotropic end and has a high salting-out potential.^{68,152} The results reveal that of the three salts, Gdm_2SO_4 is the weakest DNA origami denaturant and TPACl the strongest, with GdmCl showing intermediate activity. Furthermore, we observe a strong superstructure dependence. In particular for 3D DNA origami nanostructures, it is observed that less rigid designs with a lower crossover density²⁴ are more resistant against chemical denaturation by Gdm^+ and TPA^+ . Finally, nanostructural DNA origami stability assessed by AFM were compared with melting temperature measurements, performed at Helmholtz Zentrum Dresden Rossendorf in the group of Prof. Dr. Fahmy, and it was found that the melting temperatures overestimate the stability of certain DNA origami nanostructures in the presence of certain chaotropic salts.¹⁵⁸

4.3.2 Results and discussion

4.3.2.1 Gdm_2SO_4

First, Gdm_2SO_4 was added to six different DNA origami nanostructures assembled in standard assembly buffer to achieve final Gdm_2SO_4 concentrations ranging from 0 to 3 M and incubated them for 1 h at 42 °C. After incubation, the DNA origami nanostructures were deposited on freshly cleaved mica and characterized in the dry state by *ex-situ* AFM. *In-situ* AFM was intentionally avoided since it was shown previously that high Gdm_2SO_4 concentrations prevent DNA origami adsorption on mica.¹³⁶ In previous studies, the structural integrity of the DNA origami triangle was assessed by eye, which is enabled by its well-defined geometric shape that responds visibly even to minor damage.^{19,22,25,26,43,136,140,150} For other DNA origami shapes such as the rod-like 24HB used in this work, however, visual identification of structural damage is more difficult.²² Therefore, in this work, a semi-automated method¹³⁸ was adapted to quantify DNA origami structural integrity that is based on the statistical evaluation of the projected surface area occupied by each DNA origami in each AFM image (see section 4.3.4.3). Figure 4.15 shows the histograms of the projected surface area for all six DNA origami nanostructures after incubation in buffer containing 0 M, 0.5 M, 2 M, and 3 M Gdm_2SO_4 . For the DNA origami triangle (Figure 4.15 a)) in the absence of Gdm_2SO_4 , the histogram is dominated by a narrow peak located at $5.5 \times 10^3 \text{ nm}^2$ and a secondary peak at $10.5 \times 10^3 \text{ nm}^2$, which represent DNA origami monomers and dimers, respectively, as can be seen in the AFM images shown next to

the peaks. At 0.5 M Gdm₂SO₄, the histogram remains essentially unchanged, with the dominant peak still located at a projected area of $5.5 \times 10^3 \text{ nm}^2$. This indicates that the DNA origami triangles are stable at this Gdm₂SO₄ concentration, which is further verified in the corresponding AFM image. Increasing the Gdm₂SO₄ concentration to 2 M and 3 M, however, leads to subtle variations in the shape of the distributions. While the positions of the monomer and dimer peaks remain mostly unaltered, the peaks are becoming notably broader. The AFM images in the insets reveal that this is due to the simultaneous occurrence of intact and collapsed triangles with dissociated vertices. In addition, it appears that the overall fraction of DNA origami dimers increases with Gdm₂SO₄ concentration. Most importantly, the moderate denaturing effect of Gdm₂SO₄ on the DNA origami triangle as well as the observed cluster formation are consistent with the previous results¹³⁶. This confirms that the analysis of the projected surface area is sufficiently sensitive to detect even comparably small alterations in DNA origami shape and aggregation state.

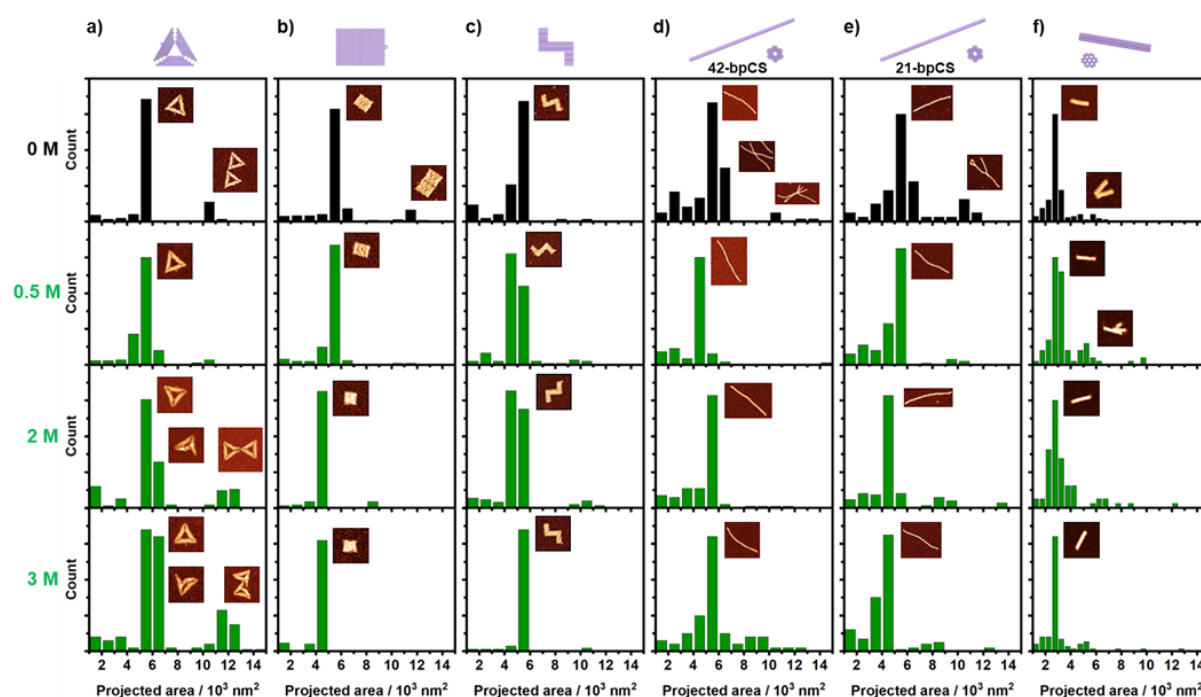


Figure 4.15 Histograms of the projected surface areas of a) DNA origami triangles, b) rectangles, c) Z shapes, d) 6HBs 42-bpCS, e) 6HBs 21-bpCS, and f) 24HBs after 1 h incubation at 42 °C in buffer containing 0 M, 0.5 M, 2 M and 3 M Gdm₂SO₄. Upper and lower limits of the projected area of 1×10^3 and $15 \times 10^3 \text{ nm}^2$ were applied. Insets show representative AFM images of individual or aggregated DNA origami nanostructures that correspond to the peaks in the histograms. For each condition, between

57 and 445 individual particles have been evaluated. Reproduced with permission.¹⁵⁸ Copyright © 2023, The Royal Society of Chemistry.

A similar trend as for the DNA origami triangle is observed also for the rectangle (see Figure 4.15 b)). As the triangle, the rectangle is a single-layer DNA origami based on the square lattice. Therefore, its monomer peak is located at the same projected area of $5.5 \times 10^3 \text{ nm}^2$. However, the rectangle has a lower tendency to aggregate than the triangle, because the edge staples have been omitted during assembly, so that intermolecular blunt-end stacking is suppressed by single-stranded scaffold loops along the long edges. Up until 0.5 M Gdm_2SO_4 , the rectangular shape remains completely intact with no notable change in the histogram. However, at 2 M and 3 M Gdm_2SO_4 , the monomer peak shifts slightly to a lower projected area around $4.5 \times 10^3 \text{ nm}^2$. While small, this change can be clearly seen in the corresponding AFM images in the insets, which reveal a smaller rectangular shape with increased height, presumably induced by the interaction with the Gdm_2SO_4 . This apparent compaction of the DNA origami rectangle could be caused by sample washing and drying. However, the fact that it occurs at the same concentrations at which the triangle is notably getting damaged suggests that this change in shape is indeed caused by exposure to the high Gdm_2SO_4 concentrations.

While the Z shape is another single-layer DNA origami as the triangle and the rectangle, it is based not on the square but on the honeycomb lattice.²⁷ Nevertheless, its monomer peak in the absence of Gdm_2SO_4 is again located at $5.5 \times 10^3 \text{ nm}^2$ (see Figure 4.15 c)). Barely any aggregates are observed because the edges of the Z shape are modified with single-stranded poly-T overhangs. Addition of 0.5 and 2 M Gdm_2SO_4 does not lead to any major shifts in the monomer peak position but only to a slight broadening of the peak. In contrast to the case of the DNA origami triangle, however, the monomer peak of the Z shape becomes narrow again at 3 M Gdm_2SO_4 . It might thus rather be related to sample-to-sample variation or the particle analysis itself and not a direct effect of Gdm_2SO_4 .

Figures 4.15 d) and e) show the histograms for the two 6HB designs that are structurally identical in all aspects except the crossover spacings.²⁴ Consequently, the histograms of both 6HB designs in the absence of Gdm_2SO_4 are rather similar, exhibiting a dominant monomer peak at $5.5 \times 10^3 \text{ nm}^2$ and a secondary dimer peak at $10.5 \times 10^3 \text{ nm}^2$. It is noteworthy that these projected area values are identical to those of the monomeric triangles and rectangles. This is surprising considering that the 6HBs essentially are double-layer DNA origami and should thus

have notably smaller projected area. This apparent discrepancy can be attributed to the collapse of the rather flimsy 6HBs during adsorption and drying, which results in a reduced height and increased width. Furthermore, it should be mentioned that the observed dimers do not form in solution but during adsorption at the mica surface. This can be seen in the corresponding AFM images in the insets of Figures 4.15 d) and e), where the 6HBs lie on top of each other. Addition of Gdm_2SO_4 lowers the obtained surface coverage,¹³⁶ which results in lower chances of neighboring 6HBs coming in direct contact and thus the almost complete disappearance of the dimer peak. The presence of Gdm_2SO_4 also leads to small shifts in the position of the monomer peak toward lower values. In contrast to the case of the rectangles, however, these shifts appear more random and their origins cannot be easily determined in the AFM images. Therefore, a more detailed analysis of the dimensions of the 6HBs exposed to the different concentrations of Gdm_2SO_4 have been conducted. As can be seen in Figure 4.16, the observed shifts in the projected surface area correlate well with a decrease in the average width of the 6HBs, whereas their average length and height remain relatively unaffected by the different concentrations of Gdm_2SO_4 . The fact that these variations in width are not correlated with corresponding changes in height indicates that they are not caused by significant structural rearrangements of the 6HBs' double helices as would be the case for partial denaturation. Rather, it can be assumed that these changes in 6HB width are caused by variations in the shape of the AFM tip. While height values can be accurately measured in AFM images, lateral dimensions always suffer from a convolution with the tip shape and thus are critically affected by variations in tip angle and radius. This is even more critical for objects such as the 6HBs, which have lateral dimensions (about 6 nm) comparable to the tip radius (< 12 nm). While these variations do not affect the potential of the statistical analysis to detect damage, they demonstrate the limitation of the analytical approach in detecting minor damage in such compact 3D DNA origami nanostructures. Therefore, both 6HB designs appear stable within the limit of detection in the presence of Gdm_2SO_4 at concentrations up to at least 3 M.

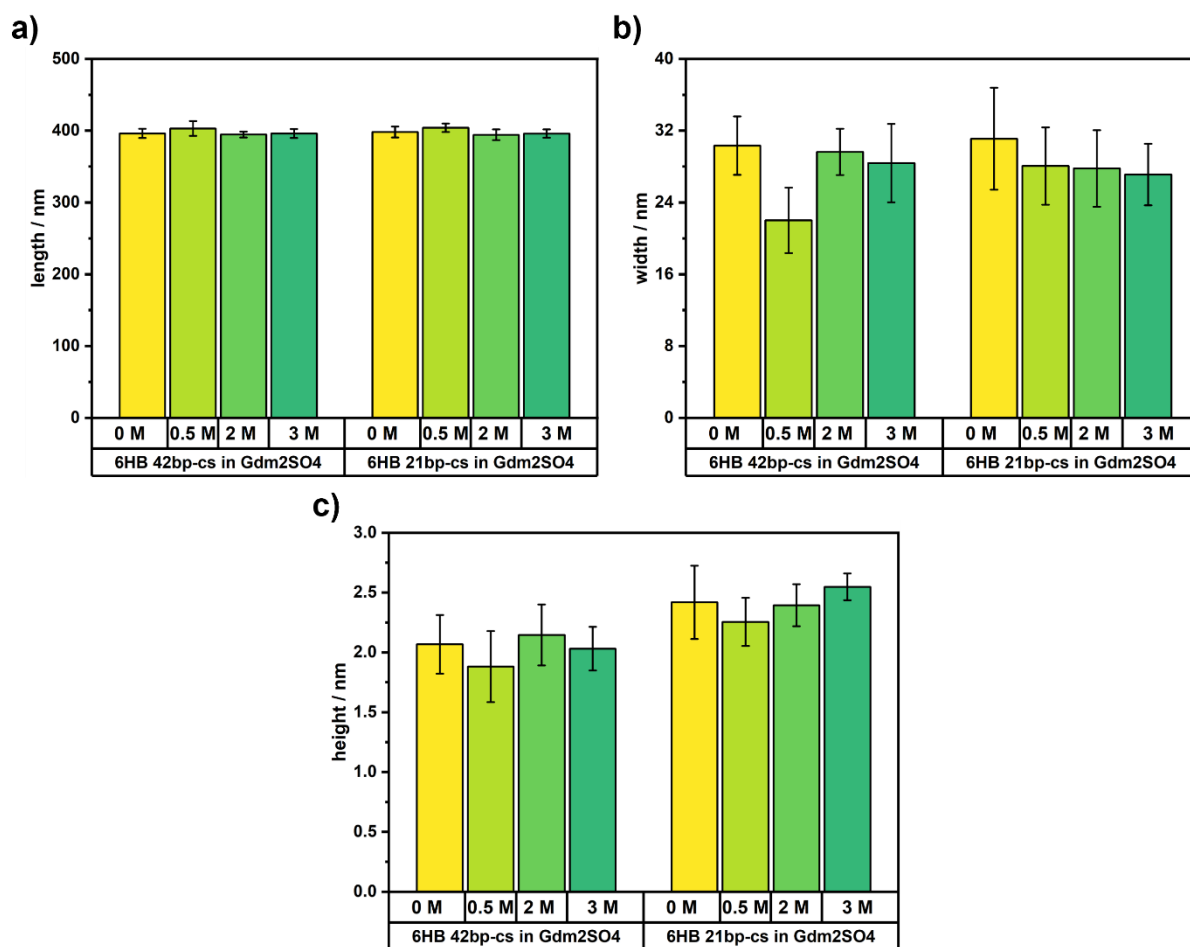


Figure 4.16 Average a) length, b) width, and c) height of the two different DNA origami 6HB designs after exposure to different concentrations of Gdm₂SO₄. The variations in 6HB width correlate well with the observed variations in the projected surface area in Figure 2. For each condition, 10 individual 6HBs have been analyzed.

Since the 24HB has a much smaller projected surface area than the other four DNA origami nanostructures, the bin size was reduced to half the original value in order to be able to differentiate between the intact and the denatured states. As can be seen in Figure 4.15 e), the 24HB in the absence of Gdm₂SO₄ exhibits a dominant monomer peak at $2.75 \times 10^3 \text{ nm}^2$, which is approximately half the value of that of the other DNA origami nanostructures. A broad but small distribution around twice that value can be observed as well and represents intact 24HB dimers. Similar to the case of the 6HBs, the monomer peak of the 24HB is rather unaffected by the addition of Gdm₂SO₄ at concentrations up to 3 M.

Therefore, even in this comparatively weak denaturant, differences between different DNA origami nanostructures can be observed. While the triangle and the rectangle exhibit notable shape distortions and aggregation in the presence of Gdm_2SO_4 , the Z shape and the three helix bundles apparently are less affected. This is most likely due to the different lattice types. The square lattice of the triangle and the rectangle assumes 10.67 bp per helical turn, which leads to residual twist strain and pronounced structural distortions.¹⁴³ The honeycomb lattice of the other structures, on the other hand, assumes a more natural 10.5 bp per helical turn, resulting in lower strain. Therefore, it appears reasonable that the more strained structures are more susceptible to partial denaturation when exposed to mild denaturants.

4.3.2.2 GdmCl

In the stronger denaturant GdmCl, the overall stability of the DNA origami nanostructures changes drastically. Here, three different concentrations were selected as well, i.e., 1 M, 4 M and 6 M, in order to obtain the same Gdm^+ concentrations in solution as for Gdm_2SO_4 . Figure 4.17 a) shows the histograms of the projected area for the DNA origami triangle. At 1 M GdmCl, prominent monomer and dimer peaks can be observed with the corresponding AFM images in the inset revealing intact triangles. Increasing the concentration to 4 M GdmCl, however, results in notable differences to the corresponding Gdm_2SO_4 concentration. In particular, the histogram shows an increase in the counts of projected surface area values below $4 \times 10^3 \text{ nm}^2$, whereas the AFM images reveal heavily damaged DNA origami triangles with partially denatured trapezoids. At an even higher GdmCl concentration of 6 M, the DNA origami triangles are completely denatured with the AFM images mostly showing the scaffold. In the histogram, this complete denaturation results in a broad projected area distribution with a maximum at low area values and a slope toward higher values. This is because the native scaffold may still carry different numbers of staples, adopt a large variety of conformations at the mica surface, and form large aggregates. Therefore, the stronger denaturant activity of GdmCl compared to Gdm_2SO_4 is reflected accurately in the histograms of the projected surface area.

In case of the DNA origami rectangle, some minor damage at the edges can be observed by AFM already at 1 M GdmCl. The DNA origami rectangles start to unravel at these edge sites, which results in a slight increase in the projected surface area (see Figure 4.17 b)). Interestingly, this initial damage appears to start at the short edges and not the long edges with their exposed scaffold loops. At 4 M GdmCl, the denaturation of the rectangle gets more pronounced with the

rectangular shapes breaking up in the center. Only a small fraction of rectangles still exhibits more or less intact shapes. This assortment of rectangular structures with different degrees of damage leads to a broad distribution of the projected surface area with the highest counts observed at low area values. Increasing the GdmCl concentration further to 6 M again results in the complete DNA origami denaturation with a similar histogram as that of the triangles. Hence, the DNA origami rectangle seems to be slightly more susceptible toward GdmCl denaturation than the triangle, with moderate damage occurring at 4 M GdmCl and complete denaturation at 6 M.

The DNA origami Z shape shows a similar behavior as the rectangle. At 1 M GdmCl, the arms start to unravel while the central bar remains mostly intact (see Figure 4.17 c)). This leads to a notable broadening of the monomer peak. Already at a GdmCl concentration of 4 M, however, complete DNA origami melting is observed with the histogram of the projected surface area resembling those of the other 2D DNA origami nanostructures at 6 M GdmCl. Therefore, of the three 2D DNA origami nanostructures investigated here, the Z shape has the lowest stability in GdmCl, but the highest stability in Gdm₂SO₄. This exemplifies the complex interplay between DNA origami superstructure and denaturant type.

For the 6HBs 42-bpCS, however, the situation is remarkably different (see Figure 4.17 d)). Here, the histograms are dominated by a strong monomer peak up to the highest GdmCl concentration of 6 M. Nevertheless, at 4 M and 6 M GdmCl, a small fraction of 6HBs in the AFM images seem to be broken and sometimes folded back on themselves, while others appear partially melted at the ends. This results in broader distributions of the projected surface area, in which the dominant monomer peaks also include 6HBs with apparent breaks but otherwise almost identical projected surface areas. Compared to the 2D DNA origami shapes, the 6HB 42-bpCS is pronouncedly more stable in GdmCl. In contrast, the 21-bpCS 6HB design shows a behavior more similar to the DNA origami triangles and rectangles (see Figure 4.17 e)). While only minor damage is observed at 4 M GdmCl, the 6HBs 21-bpCS are completely denatured in 6 M GdmCl, resulting in a histogram dominated by very low projected area values. Similar increased stability of the 42-bpCS 6HB was observed previously in Mg²⁺-free solutions and attributed to its higher flexibility allowing it to accommodate electrostatic inter-helix repulsion more efficiently.²⁴ While electrostatic repulsion is unlikely to play a role in 6 M Gdm⁺, the additional strain exerted on the individual staple strands by the higher crossover density may promote staple dehybridization under denaturing conditions.

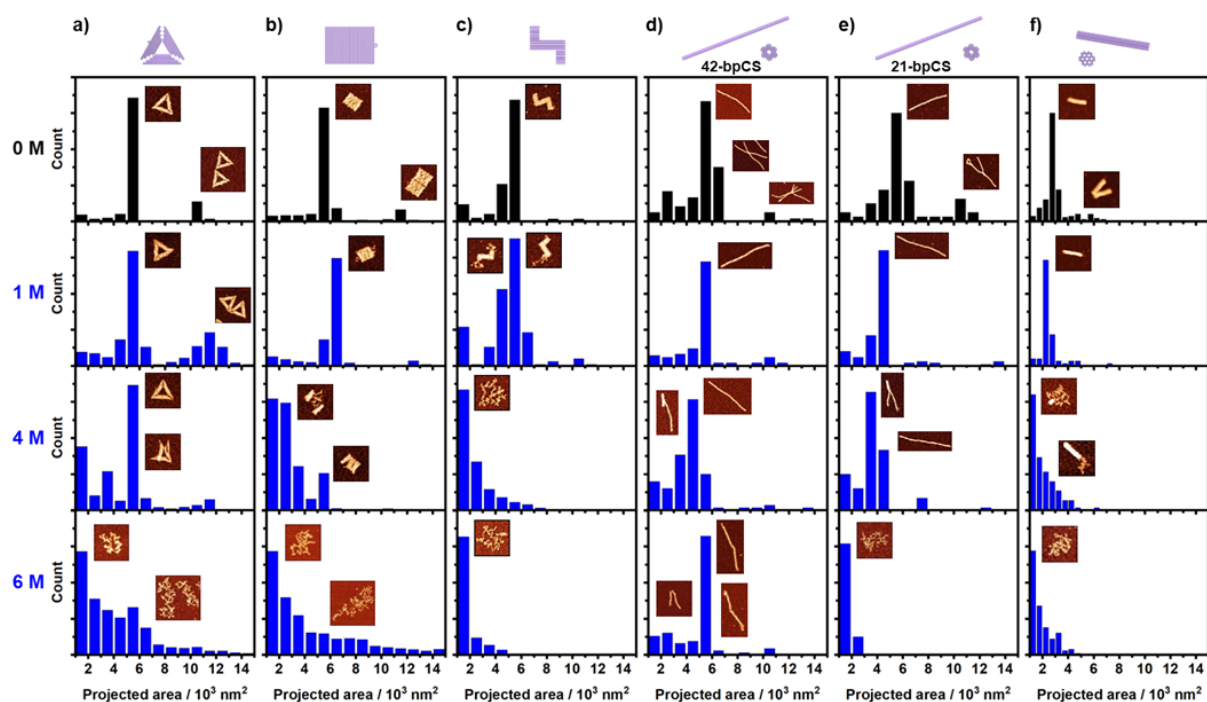


Figure 4.17 Histograms of the projected surface areas of a) DNA origami triangles, b) rectangles, c) Z shapes, d) 6HBs 42-bpCS, e) 6HBs 21-bpCS, and f) 24HBs after 1 h incubation at 42 °C in buffer containing 0 M, 1 M, 4 M and 6 M GdmCl. Upper and lower limits of the projected area of 1×10^3 and $15 \times 10^3 \text{ nm}^2$ were applied. Insets show representative AFM images of individual or aggregated DNA origami nanostructures that correspond to the peaks in the histograms. For each condition, between 43 and 1239 individual particles have been evaluated. Reproduced with permission.¹⁵⁸ Copyright © 2023, The Royal Society of Chemistry.

Figure 4.17 f) shows the results for the 24HB DNA origami, which indicate an even higher susceptibility toward GdmCl-induced denaturation. While a distinct monomer peak representing intact 24HBs can be observed in the histogram at 1 M GdmCl, this peak is replaced with a broad distribution dominated by small projected area values already at 4 M GdmCl. Corresponding AFM images reveal that 24HB denaturation at this concentration is so advanced that only a few structures still exhibit some small parts of the native 24HB fold. Increasing the GdmCl concentration to 6 M results in the complete denaturation of all 24HBs. The reduced stability of the 24HB in GdmCl is rather not surprising considering that it has a high density of staple crossovers similar to the 21-bpCS 6HBs and additionally a comparably high number of scaffold crossovers.²⁸ Overall, the results presented in this section reveal that DNA origami

denaturation in GdmCl depends not only on GdmCl concentration but also on DNA origami superstructure.

4.3.2.3 TPACl

Finally, the Gdm^+ cation was exchanged with TPA^+ and DNA origami denaturation in TPACl were studied, which is another well-known chaotropic salt used in protein and DNA denaturation. Since the overall solubility of TPACl is distinctly lower than that of the Gdm^+ salts, only two concentrations were selected, i.e., 0.5 M and 1.5 M. However, despite the lower concentrations, a much stronger denaturing effect of TPACl for each DNA origami nanostructure was observed. As can be seen in Figure 4.18, a TPACl concentration of 1.5 M results in complete DNA origami denaturation for all shapes investigated. This already evidences the much higher denaturant activity of TPACl compared to GdmCl, which is consistent with previous observations in the denaturation of polypeptides.⁵² Differences between the different DNA origami shapes are only visible at a lower concentration of 0.5 M TPACl. Here, the denatured DNA origami triangles and rectangles appear slightly more structured in the AFM images than the Z shapes, the 21-bpCS 6HBs, and the 24HBs, which are already completely denatured. Most astonishingly, however, the 42-bpCS 6HB design appears to be completely intact at this TPACl concentration of 0.5 M. Therefore, DNA origami denaturation shows roughly the same superstructure dependence in TPACl as in GdmCl.

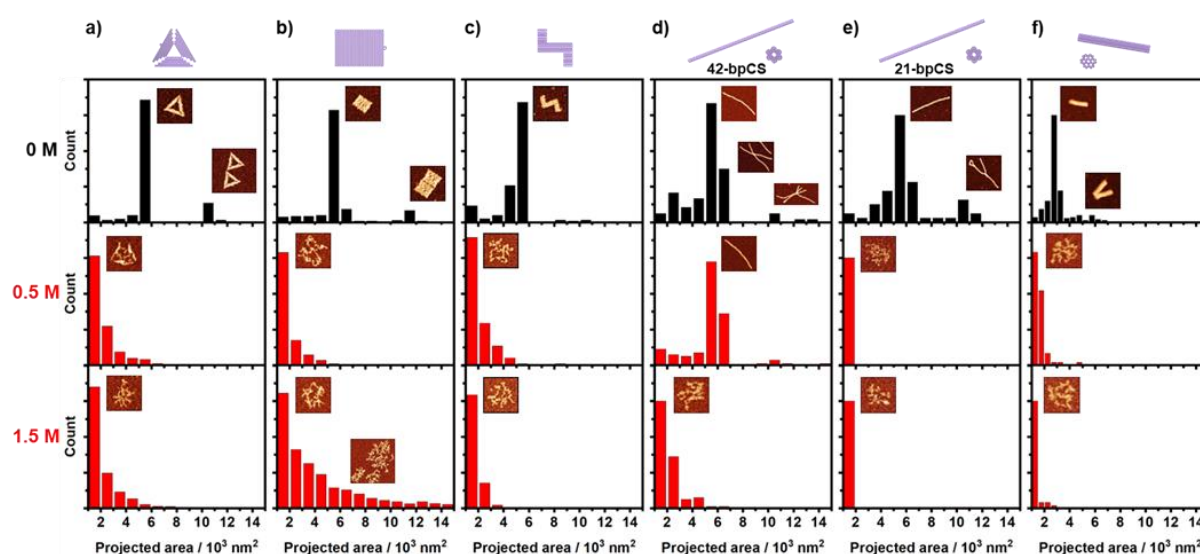


Figure 4.18 Histograms of the projected surface areas of a) DNA origami triangles, b) rectangles, c) Z

shapes, d) 6HBs 42-bpCS, e) 6HBs 21-bpCS, and f) 24HBs after 1 h incubation at 42 °C in buffer containing 0 M, 0.5 M, and 1.5 M TPACl. Upper and lower limits of the projected area of 1×10^3 and $15 \times 10^3 \text{ nm}^2$ were applied. Insets show representative AFM images of individual or aggregated DNA origami nanostructures that correspond to the peaks in the histograms. For each condition, between 9 and 2449 individual particles have been evaluated. Reproduced with permission.¹⁵⁸ Copyright © 2023, The Royal Society of Chemistry.

4.3.2.4 Quantitative comparison

In order to quantitatively compare the differential effects of the different salts on the structural integrity of the different DNA origami nanostructures, the relative integrity (RI) from the histograms of the projected surface areas for all shapes and conditions were calculated. In the absence of chaotropic salts, the RI values were calculated as the combined counts of the monomer and dimer peaks relative to the overall counts (see Chapter 4.3.4.3 for details). The same was then done for all other conditions with chaotropic salts by using the same peak positions as in the absence of the chaotropic salts. The so-determined RI values are shown in Figure 4.19 for the different DNA origami shapes and chaotropic salts in dependence of the salt concentration.

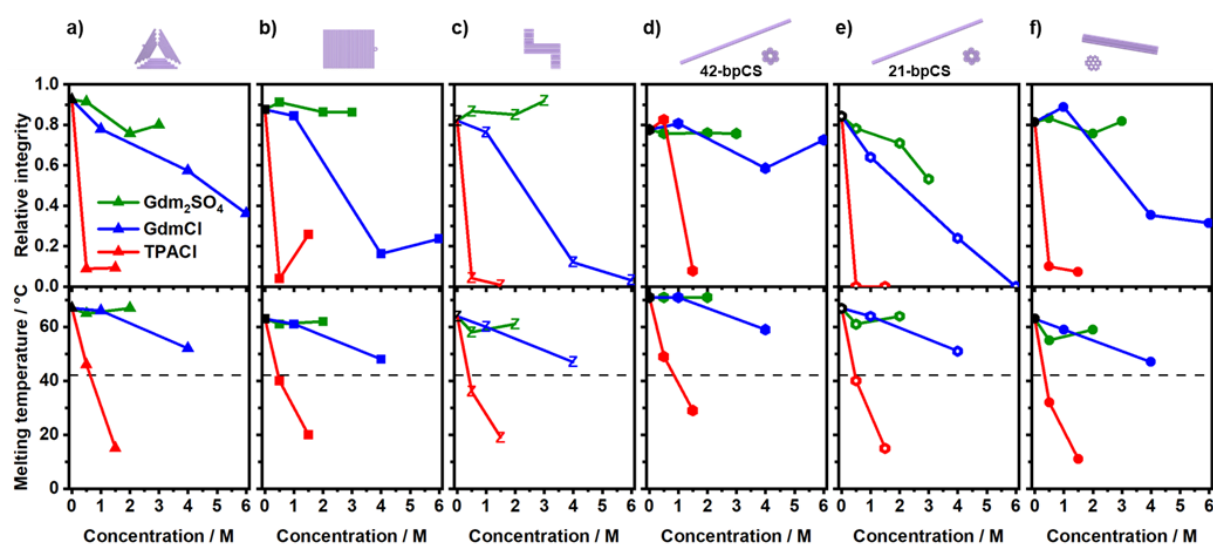


Figure 4.19 Relative integrity (RI, upper plots) and melting temperature (T_m , lower plots) of a) DNA origami triangles, b) rectangles, c) Z shapes, d) 6HBs 42-bpCS, e) 6HBs 21-bpCS, and f) 24HBs in dependence of the concentrations of the different chaotropic salts. The relative integrity values were determined after 1 h incubation at 42 °C. This incubation temperature is indicated in the melting

temperature plots by the broken horizontal lines. Melting temperature measurements have been performed at Helmholtz-Zentrum Dresden-Rossendorf in the group of Prof. Dr. Fahmy. Reproduced with permission.¹⁵⁸ Copyright © 2023, The Royal Society of Chemistry.

In general, the RI data in Figure 4.19 reproduce the main trends observed in the qualitative analyses in Figures 4.15, 4.17 and 4.18, i.e., Gdm_2SO_4 is the weakest and TPACl the strongest denaturant. However, for Gdm_2SO_4 , almost no effect is observed for most DNA origami shapes, with the RI values remaining above 0.8, indicating that the RI does not respond to small changes in DNA origami shape, even though they are visible in the histograms of the projected surface area. The only exception is the 6HB 21-bpCS, where RI decreases monotonically with increasing Gdm_2SO_4 concentration due to the observed decrease in 6HB width (see Figure 4.16 b)). In contrast to Gdm_2SO_4 , the RI values in Figure 4.19 reveal much larger changes in the presence of GdmCl . Here, 6HB 42-bpCS is the exception with an RI value that is almost unaffected by the addition of GdmCl up until 6 M, in line with its high stability observed under other denaturing conditions.^{22,24,140} A similar yet less pronounced behavior is observed in the presence of TPACl. Here, a TPACl concentration of 0.5 M results in RI values below 0.1 for all DNA origami nanostructures except 6HB 42-bpCS, which remains at an RI of about 0.8. A rather exceptional behavior is observed for the DNA origami rectangle in TPACl. While its RI is almost zero at 0.5 M, it increases to more than 0.2 at 1.5 M TPACl. Upon closer inspection of the projected surface area histograms and corresponding AFM images in Figure 4.18 b), it becomes clear that this, in fact, is not due to different denaturation states but rather an artefact caused by clustering of completely denatured rectangles.

For comparison, the melting temperature (T_m) of the different DNA origami shapes in the different environments by their UV absorption have been measured at Helmholtz Zentrum Dresden Rossendorf in the group of Prof. Dr. Fahmy.¹⁵⁸ Because of the strong UV absorption of Gdm^+ , however, these measurements were limited to low and medium Gdm^+ concentrations up to 4 M. Nevertheless, the T_m data shown in Figure 4.19 qualitatively reproduce the trends observed in the RI data. In particular, for all DNA origami nanostructures, addition of Gdm_2SO_4 barely has any effect on the determined T_m values. GdmCl , on the other hand, leads to a moderate reduction of T_m at a concentration of 4 M. In the presence of TPACl, comparable T_m values are observed already at 0.5 M, while at a concentration of 1.5 M TPACl, T_m is drastically reduced and may even reach values below room temperature.

Whereas the salt dependence of the RI values is well reproduced by the determined melting temperatures, the situation is more complex when the superstructure dependence is considered. Comparing just the two 6HB designs in Figures 4.19 d) and e), it was found that the T_m of the 42-bpCS design in 0.5 M TPACl is slightly above 42 °C, while that of 21-bpCS is slightly below. Consequently, after 1 h incubation at this temperature, the RI value of 6HB 42-bpCS remains at roughly its salt-free value, whereas that of 21-bpCS has already dropped to zero. In 4 M GdmCl, both the DNA origami triangle and the 6HB 42-bpCS have a $T_m > 50$ °C, i.e., well above 42 °C (see Figures 4.19 a) and d)). Nevertheless, incubation of both shapes at this temperature results in reduced RI values below 0.6. This effect is even more pronounced for the DNA origami rectangle, the Z shape, and the 6HB 21-bpCS, where T_m values around 50 °C are contrasted with RI values of 0.16, 0.12, and 0.24, respectively (see Figures 4.19 b) and e)). Visual inspection of the corresponding AFM images in Figures 4.17 further suggests that these surprisingly low RI values are indeed indicative of structural damage. The most surprising observation, however, is made for the DNA origami triangle in 0.5 M TPACl (Figure 4.19 a)). Here, a T_m of 46 °C is determined, i.e., above the incubation temperature of 42 °C and only 3 °C below that of the 6HB 42-bpCS under the same conditions (Figure 4.19 d)). Nevertheless, incubation at 42 °C results in almost complete denaturation of the DNA origami triangles, whereas the 6HBs 42-bpCS remain perfectly stable (see Figures 4.18 a) and d) and 4.19 a) and d)). This demonstrates that while T_m measurements potentially can provide a rough estimate of DNA origami stability under denaturing conditions, they may both drastically overestimate or underestimate DNA origami stability for certain DNA origami shapes and designs in denaturing environments.

4.3.3 Conclusion

The stability of six different 2D and 3D DNA origami nanostructures in the chaotropic salts Gdm₂SO₄, GdmCl, and TPACl has been investigated. All six DNA origami nanostructures showed a similar dependence on the salt type. Gdm₂SO₄ had barely any effect on the different DNA origami up to a Gdm⁺ concentration of 6 M. For TPACl, however, complete DNA origami denaturation was observed already at a concentration of 1.5 M. The denaturing activity of GdmCl, on the other hand, was in-between those of Gdm₂SO₄ and TPACl. This is a rather remarkable observation since TPA⁺ and Gdm⁺ are located near each other in the Hofmeister series. In general, these differences in the action of Gdm⁺ and TPA⁺ could result from different

interactions of these ions with buffer components. While Gdm^+ can participate also in hydrophobic interactions, H-bonding is its main type of interaction. Therefore, Gdm^+ may directly interact with Tris, which is known to participate in H-bonding interactions.¹⁵⁹ However, previous studies did not observe any notable change in the denaturing potential of Gdm^+ due to the presence of Tris.¹⁶⁰ Since Mg^{2+} is a divalent cation, it unlikely participates in direct interactions with Gdm^+ due to electrostatic repulsion. On the other hand, Mg^{2+} and Gdm^+ compete for hydration water, which at high Mg^{2+} concentrations of 100 mM and above may lead to a salting-out of Gdm^+ and thereby to enhanced DNA origami denaturation.²⁶ In the present study, however, a constant Mg^{2+} concentrations of 10 mM was used so that this effect can be considered negligible. In contrast, TPA^+ is a cation with even lower charge density than Gdm^+ that does not show any ion pairing capability. Moreover, since it cannot form H-bonds, TPA^+ participates only in hydrophobic interactions through its aliphatic side chains. Therefore, any interactions of TPA^+ with Tris or Mg^{2+} appear unlikely. The strongly different effects of Gdm^+ and TPA^+ on DNA stability thus suggest different mechanisms of interaction with the DNA origami nanostructures. Notably, similar observations have been made regarding the interactions of these salts with proteins.^{68,71}

Comparing the different DNA origami nanostructures, a remarkable superstructure dependence was found. In particular, the 6HB 42-bpCS design is the most stable of all tested DNA origami nanostructures and remains almost completely intact in 6 M GdmCl and 0.5 M TPACl , while all other designs are almost completely denatured under such conditions. This is in agreement with its behavior under Mg^{2+} -free conditions, which has been attributed to its less rigid design allowing a certain degree of readjustment to accommodate increased electrostatic inter-helix repulsion. Since electrostatic repulsion is unlikely to play a role at such high ionic strengths, it may be assumed that compared to the other DNA origami nanostructures, the staples of the 6HB 42-bpCS experience a lower amount of strain. When Gdm^+ or TPA^+ interfere with the base stack and destabilize base pairs and induce unstacking, such strain may promote staple dissociation from the scaffold and thereby DNA origami denaturation.

Finally, the AFM-based measurement of DNA origami nanostructure stability were compared with melting temperature measurements.¹⁵⁸ While in most cases, the determined melting temperatures show similar trends as the relative integrity of the DNA origami nanostructures derived from AFM images, there are some notable exceptions. In such cases, the melting temperature measurements suggest more or less stable DNA origami nanostructures under the

evaluated conditions, whereas AFM images show strong to complete DNA origami denaturation. Such a behavior was observed only for certain DNA origami shapes in the presence of certain chaotropic salts.

These results exemplify the high complexity of DNA origami stability under denaturing conditions, which shows an interdependence of design parameters and environmental factors. In previous studies, mechanical properties and especially rigidity have been identified to strongly affect DNA origami stability under physiological conditions.^{23,24} The present work demonstrates that the same parameters are also controlling DNA origami stability in the presence of different chemical denaturants with different mechanisms of actions. Most remarkably, 3D designs that are more stable under low-Mg²⁺ conditions also show enhanced stability in the presence of Gdm⁺ and TPA⁺. It may thus become possible at some point to derive general design rules for the fabrication of DNA origami nanostructures with optimized stability in diverse chemical environments.

4.3.4 Materials and Methods

4.3.4.1 DNA origami assembly

The assembly of the DNA origami nanostructures, i.e., the Rothemund triangle⁴, the “tall” rectangle,⁴ the Z shape,²⁷ the 6HB 42-bpCS,²⁴ the 6HB 21-bpCS,²⁴ and the 24HB,²⁸ was performed as previously described,¹⁶¹ A 10:1 molar ratio of staples (Eurofins) to scaffold (Tilibit) was employed in 10 mM Tris buffer (Sigma-Aldrich) containing 10 mM MgAc₂ (Sigma-Aldrich). The pH of the buffer was adjusted to 8.0 with acetic acid. In the assembly of the DNA origami rectangles, all edge staples were omitted to avoid aggregation in liquid due to blunt-end stacking.⁴ The DNA origami nanostructures were either purified by spin filtering using Amicon Ultra-0.5 mL spin filters with 100 kDa molecular weight cut-off (Merck) or by PEG precipitation based on a previous protocol.¹³⁶ The concentrations of the purified DNA origami nanostructures were determined using an Implen Nanophotometer P330 and afterwards adjusted to 100 nM.

4.3.4.2 Sample preparation and AFM imaging

Gdm₂SO₄ salt (Sigma-Aldrich) and TPACl salt (Sigma-Aldrich) were dissolved in HPLC-grade water (VWR) to reach a concentration of 8 M and 2 M, respectively. GdmCl was purchased as an 8 M solution from Sigma-Aldrich. For each experiment, a 100 µl solution consists of 5 nM DNA origami in 10 mM Tris/MgAc₂ buffer containing different chaotropic salt concentrations was incubated for 1 h at 42 °C using a Primus 25 advanced thermocycler (PEQLAB). For the 6HBs without chaotropic salts, the DNA origami concentration in the sample was reduced to 2 nM because the higher concentrations resulted in larger surface coverage, which appeared as strong clustering in the AFM images. The addition of chaotropic salts, however, reduces DNA origami adsorption and thus leads to a lower surface coverage,¹³⁶ Therefore, the original concentration of 5 nM could be used under those conditions. After incubation, 1 µl of the sample was deposited on a freshly cleaved mica substrate, immediately covered with 100 µl of Tris/MgAc₂ buffer in order to dilute the relatively high concentrations of the used salts, and incubated for 5 min. Then, the sample was rinsed with about 12 mL of HPLC-grade water and blow-dried in a stream of Ar or ultra-pure air. AFM imaging was performed in air using a Bruker Dimension ICON in ScanAsyst PeakForce Tapping mode with ScanAsyst-Air cantilevers (Bruker). The images were recorded with a size of 3x3 µm², a resolution of 1024x1024 px, and a line rate of 1 Hz.

4.3.4.3 AFM image analysis

AFM image data processing and the grain analysis were done using the open-source software Gwyddion.¹⁴⁹ First, each individual image was flattened and height adjusted. In the next step, a height threshold was applied to mask the DNA origami in the image (see Figures 4.20 a) and b)). The distribution of the projected surface area of the masked DNA origami was determined using the grain analysis tool for at least 3 images. The distributions were then evaluated in OriginPro 2021 (OriginLab) by generating histograms of the projected surface area values in the range from 1 x 10³ to 15 x 10³ nm² using a bin size of 1 x 10³ nm², resulting in a total number of 14 bins (see Figure 4.20). The lower cut-off of the projected surface area was chosen to minimize the impact of artifacts from the remaining background and small debris. For the 24HB, however, the bin size was reduced to 0.5 x 10³ nm² (resulting in a total number of 28 bins) in order to better resolve denaturation-induced changes in the smaller projected surface area of this multilayer structure.

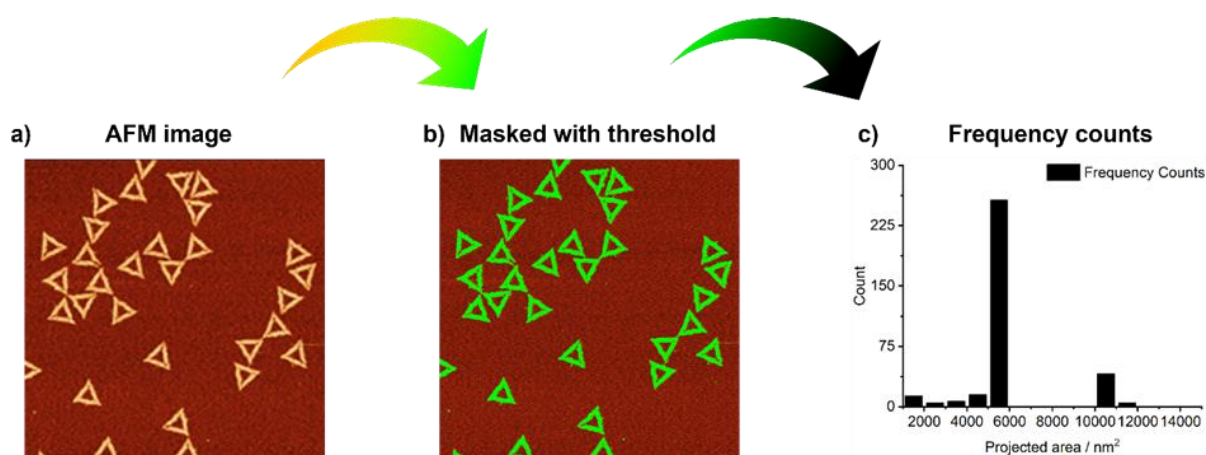


Figure 4.20. Illustration of AFM image data processing and grain analysis. a) Each individual image was flattened and height adjusted. b) DNA origami triangles in the image were masked using an appropriate height threshold. c) The histogram of the projected surface area values of the masked DNA origami was determined for at least 3 images and evaluated in the projected surface area range from 1×10^3 to 15×10^3 nm² using a bin size of 1×10^3 nm², resulting in a total number of 14 bins. Reproduced with permission.¹⁵⁸ Copyright © 2023, The Royal Society of Chemistry.

Finally, the relative integrity (RI) was calculated for all DNA origami shapes. This was first done for the reference samples in the absence of chaotropic salts by dividing the counts of the bins corresponding to intact DNA origami shapes by the total number of counts of all bins. Due to conformational changes and tip effects, the monomer peak has a finite width that may include also neighboring bins. Therefore, the counts of the two bins left and right of the central bin of the monomer peak were included in the calculation as well. Furthermore, also the counts of the dimer peak were included and considered as two intact DNA origami shapes. In the RI calculations for the samples exposed to the chaotropic salts, the same bins were used as for the reference samples, so that a decrease in RI upon salt addition is a measure of salt-induced denaturation.

5 Effect of Ionic Strength on the Thermal Stability of DNA Origami Nanostructures

5.1 Introduction

Due to the large variety of applications, DNA origami nanostructures encounter very different chemical environments, which may affect their shape, structural integrity, and mechanical properties in complex and so far almost unpredictable ways. In order to ensure and tailor DNA origami functionality under such diverse conditions, the effects that different environments exert on DNA origami structure and stability thus have become the focus of intense research.^{10–12,127}

One of the most important parameters in this regard is the ionic composition of the surrounding aqueous medium.¹⁰ Since the DNA duplexes of a DNA origami nanostructure are compacted into a very small volume, ionic screening of the electrostatic repulsion between the negatively charged phosphate groups in the backbones of neighboring duplexes is essential for maintaining DNA origami shape and structural integrity. The ionic strength and ionic composition of the electrolyte surrounding the DNA origami nanostructures thus have a strong influence on their stability,^{22,24,162,163} denaturation,^{26,136,150} aggregation,^{137,148} conformation,^{164,165} and mechanical properties,^{24,166} as well as their interactions with lipid bilayers,^{167,168} inorganic surfaces,^{169,170} and therapeutic molecules.^{28,86}

In this work, the thermal stability of different 2D and 3D DNA origami nanostructures in dependence of ionic strength has been investigated. Fluorimetry was used to record melting curves of different DNA origami nanostructures in the presence of different Mg^{2+} concentrations ranging from 0.2 to 100 mM. Atomic force microscopy was employed to complement the melting curve data and assess DNA origami melting not only on the duplex but also on the nanostructure level. The DNA origami melting temperatures T_m extracted from the melting curves are compared to calculated ensemble T_m values derived from the melting temperatures of all staples present in each DNA origami nanostructure. While the calculated staple ensemble T_m values show the expected logarithmic dependence on Mg^{2+} concentration,¹⁷¹ strong deviations from this behavior are observed in the experiments, in particular for high Mg^{2+} concentrations exceeding 10 mM. Under these conditions, T_m appears

to saturate and become independent of the ionic strength. Since the degree of deviation between the calculated and measured T_m values depends on DNA origami superstructure, it may be assumed that the T_m of a given DNA origami nanostructure at high ionic strength is governed no longer by electrostatic repulsion but mostly by mechanical strain. Consequently, this constitutes an intrinsic limit to the maximum T_m of a given DNA origami nanostructure that can be achieved by ionic stabilization. These results thus not only provide further insights into the complex interplay of environmental and design parameters that governs DNA origami stability but also demonstrate how strongly DNA origami nanostructures differ in their molecular interactions from normal duplex DNA.

5.2 Results and discussion

Figure 5.1 shows schematic representations of the DNA origami nanostructures investigated in this work, along with some key parameters. Five different shapes have been selected: the 2D “tall” rectangle,⁴ the 2D Rothemund triangle,⁴ two 3D six-helix bundles (6HBs) with different crossover spacings (42 vs. 21 bp),²⁴ and a 3D 24-helix bundle (24HB).²⁸ As can be seen in Figure 5.1, all five structures have comparable numbers of nucleotides (nt) and staples, comparable average staple lengths, and almost identical GC contents. They do differ, however, in the total numbers of crossovers. The rectangle, the triangle, and the 6HB with 42 bp crossover spacing (42-bpCS) have almost identical numbers of staple crossovers (~ 340), whereas the 6HB with 21 bp crossover spacing (21-bpCS) and the 24HB have at least twice as many. Furthermore, the 24HB also has a much higher number of scaffold crossovers. It was recently demonstrated that DNA origami nanostructures with higher numbers of crossovers are mechanically more rigid and at the same time more susceptible to denaturation under unfavorable ionic conditions.²⁴

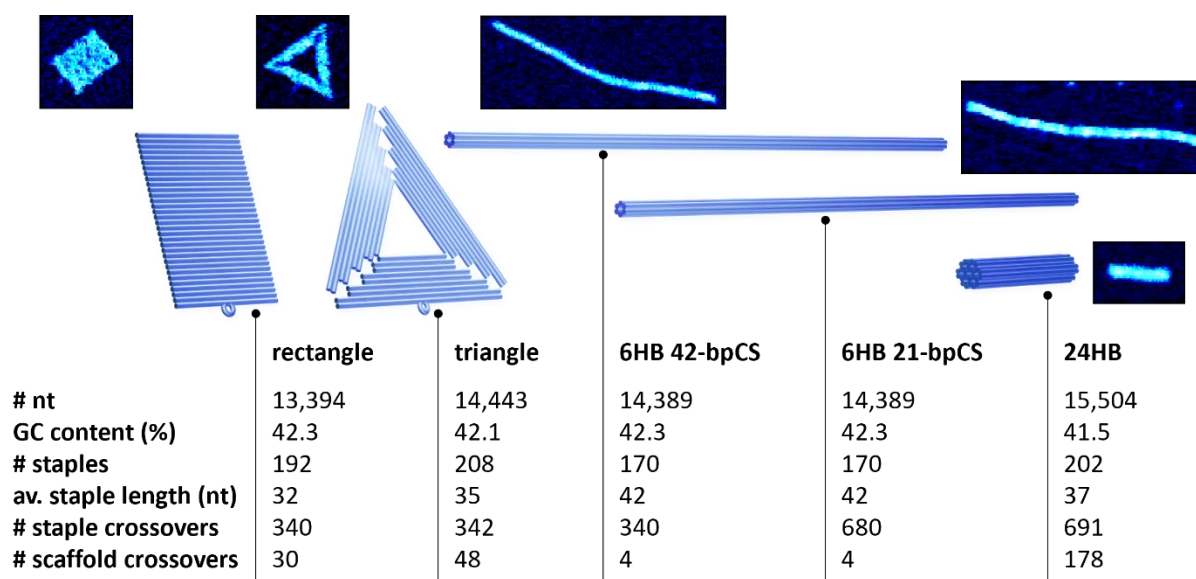


Figure 5.1 Schematic representations, representative AFM images, and key parameters of the DNA origami nanostructures investigated in this work. The AFM images have sizes of 150 x 150 nm² (rectangle, triangle), 400 x 150 nm² (6HBs), and 150 x 100 nm² (24HB), respectively.

It has been attempted to estimate the melting temperatures of the different DNA origami nanostructures shown in Figure 5.1 from the theoretical T_m distributions of their staple sets. For this, the melting temperature of each staple of each of the five staple sets was calculated at five different Mg²⁺ concentrations between 0.2 and 100 mM using the DINAMelt webserver.¹⁷² In these calculations, it was assumed that the staple hybridizes with a fully complementary oligonucleotide, with both strands having the same concentration. These assumptions are certainly not fulfilled in DNA origami melting where each staple strand undergoes multiple hybridization events with non-consecutive segments of the scaffold and experiences electrostatic repulsion from neighboring staples. Nevertheless, such calculations provide a straightforward estimate of the collective behavior of independent, non-interacting duplexes with the same nucleotide sequences as the DNA origami. Comparing the results to the experimentally determined melting curves will thus enable to identify deviations from pure ensemble statistics that result from the folding of the DNA into DNA origami nanostructures as well as specific effects of the different superstructures.

Figure 5.2 a) exemplarily shows the calculation results obtained for the DNA origami rectangle (see Figures 5.3-5.6 for the other DNA origami nanostructures). The obtained distribution is well approximated by a Gaussian and does not show any strong variation in shape at the

different Mg^{2+} concentrations. The width of the distribution does not seem to be affected by the increasing Mg^{2+} concentration. Its center, however, is shifting to higher temperatures. The strongest shift is observed between 0.2 and 10 mM Mg^{2+} , while a further increase in Mg^{2+} concentration results only in minor shifts. Therefore, the ensemble T_m represented by the center of the Gaussian distribution shows a similar dependence on ionic strengths as the T_m of a single DNA duplex.¹⁷¹ The same general behavior is also observed for the four other DNA origami nanostructures (see Figures 5.3-5.6).

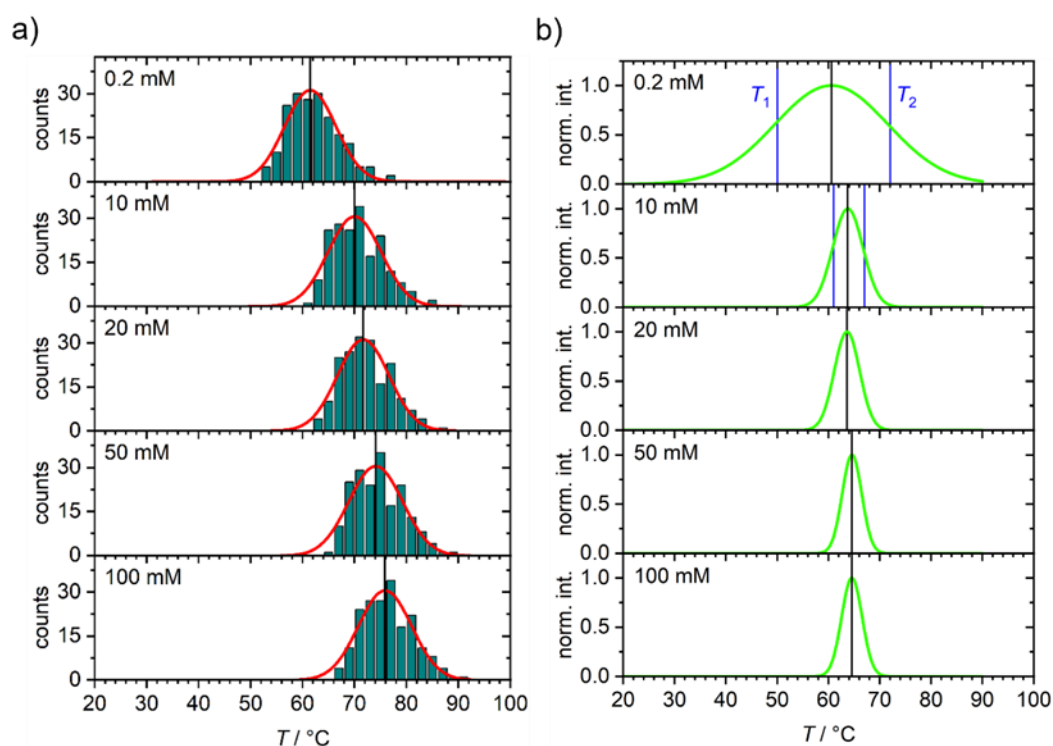


Figure 5.2 a) Calculated distribution of staple melting temperatures for the DNA origami rectangle at different Mg^{2+} concentrations. The red curves represent Gaussian fits to the distributions and the black vertical lines indicate the centers of the Gauss curves, corresponding to the ensemble T_m . b) Normalized melting transition of the DNA origami rectangle at different Mg^{2+} concentrations obtained by fitting the negative derivatives of the recorded melting curves with several Gaussians. The black vertical lines indicate the centers of the Gauss curves, corresponding to the DNA origami T_m . The blue vertical lines in b) indicate temperatures T_1 and T_2 at which the AFM images were recorded.

Melting curves of the different DNA origami nanostructures shown in Figure 5.1 were determined using a well-established fluorometric assay based on the intercalation of the

fluorescent dye SYBR Green. This assay relies on the higher affinity of SYBR Green for double-stranded compared to single-stranded DNA and is frequently employed to monitor DNA origami assembly^{173,174} and melting.^{25,175,176} However, in addition to intercalation between the base pairs, SYBR Green is also able to bind to the minor groove.¹⁷⁷ Finally, the binding of SYBR Green to duplex DNA is markedly reduced in the presence of high cation concentrations, with Mg^{2+} having a much stronger effect than Na^+ .¹⁷⁷ Consequently, the recorded melting curves are characterized by a rather strong background with additional secondary features and show a decrease in fluorescence intensity with increasing Mg^{2+} . Nevertheless, DNA origami melting temperatures at the different Mg^{2+} concentrations could be extracted by fitting the negative derivative of the melting curves with several Gaussians to account for the background features as well as the melting transition.

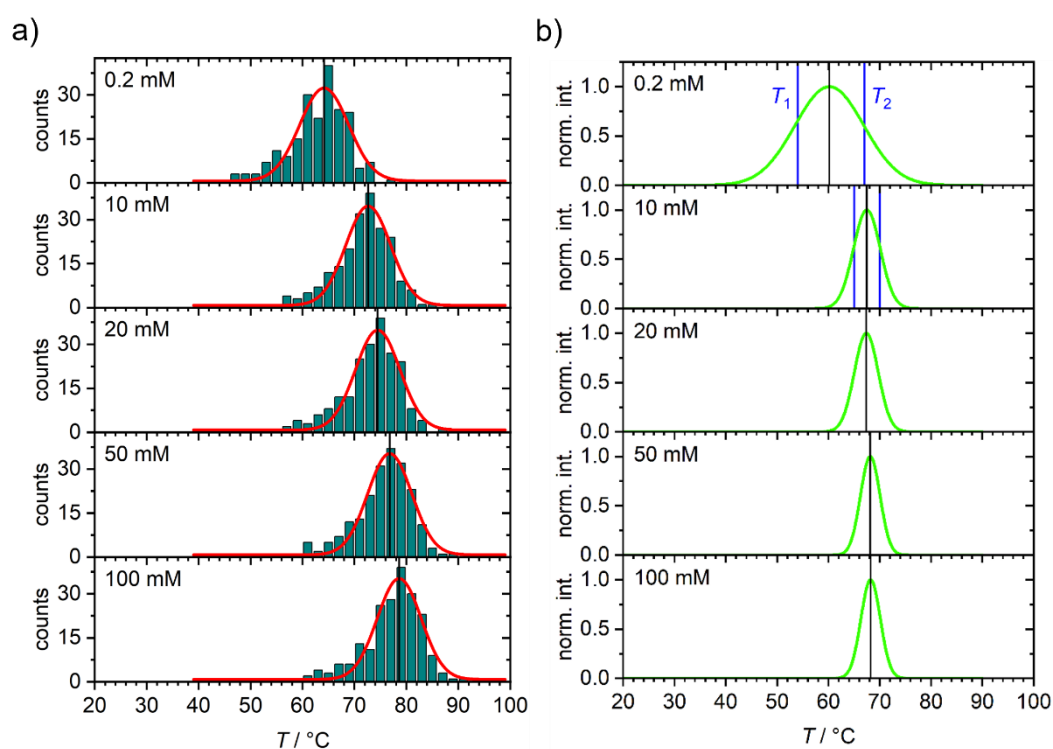


Figure 5.3 a) Calculated distribution of staple melting temperature for the DNA origami triangle at different Mg^{2+} concentrations. The red curves represent Gaussian fits to the distributions and the black vertical lines indicate the centers of the Gauss curves, corresponding to the ensemble T_m . b) Normalized melting transition of the DNA origami triangle at different Mg^{2+} concentrations obtained by fitting the negative derivatives of the recorded melting curves with several Gaussians. The black vertical lines indicate the centers of the Gauss curves, corresponding to the DNA origami T_m . The blue vertical lines in b) indicate temperatures T_1 and T_2 at which AFM images were recorded.

Figure 5.2 b) shows the so-obtained Gaussians that approximate the melting transitions of the DNA origami rectangle at the different Mg^{2+} concentrations. The most obvious difference to the calculated distributions shown in Figure 5.2 a) is the large width of the melting transition at 0.2 mM Mg^{2+} . Similarly broad melting transitions at this Mg^{2+} concentration are observed also for the other DNA origami nanostructures (see also Figures 5.3-5.6) and are most likely the result of insufficient electrostatic screening of inter-helix repulsion resulting in the structural collapse of the DNA origami. Several previous studies have demonstrated that 2D and 3D DNA origami nanostructures maintain their structural integrity at sub-mM Mg^{2+} concentrations, provided that no destabilizing components such as EDTA are present in solution.^{10,11,17,22,24,146,178–180}

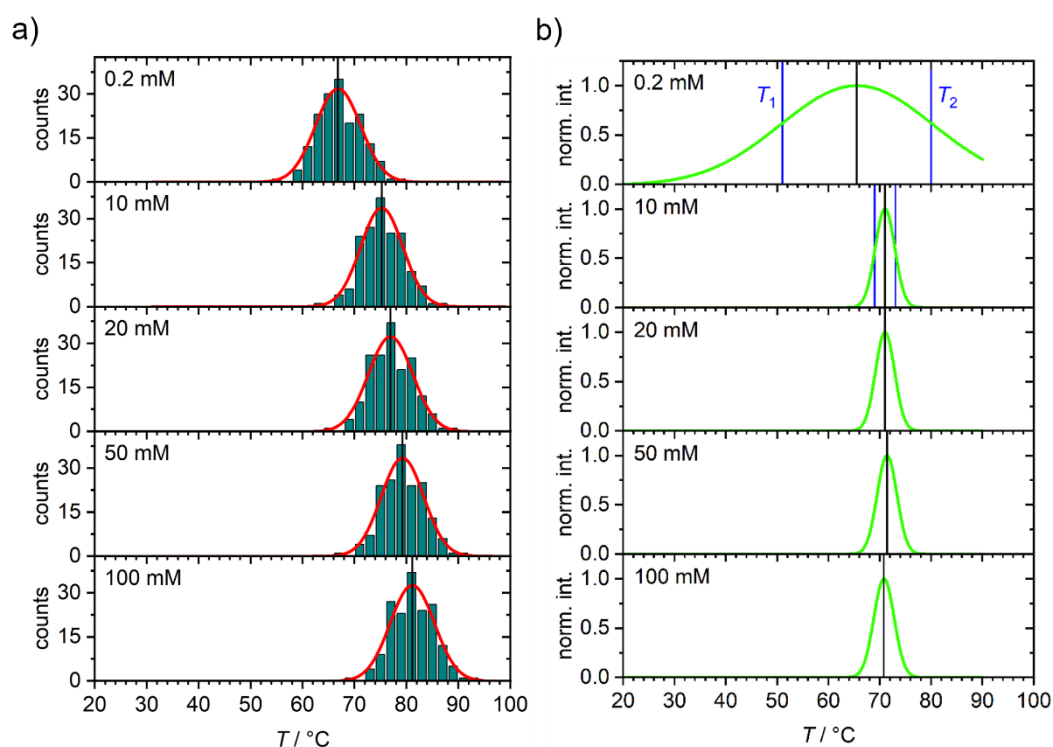


Figure 5.4 a) Calculated distribution of staple melting temperature for the DNA origami 6HB 42-bpCS at different Mg^{2+} concentrations. The red curves represent Gaussian fits to the distributions and the black vertical lines indicate the centers of the Gauss curves, corresponding to the ensemble T_m . b) Normalized melting transition of the DNA origami 6HB 42-bpCS at different Mg^{2+} concentrations obtained by fitting the negative derivatives of the recorded melting curves with several Gaussians. The black vertical lines indicate the centers of the Gauss curves, corresponding to the DNA origami T_m . The blue vertical lines in b) indicate temperatures T_1 and T_2 at which AFM images were recorded.

However, the observed broadening of the melting transitions suggest that some additional destabilization occurs nevertheless. Within the DNA origami, many staples experience mechanical strain as a result of electrostatic inter-helix repulsion. In the absence of a sufficient amount of stabilizing Mg^{2+} ions, such strained staples will melt earlier than other staples that have a similar T_m but experience less strain. The dehybridization and dissociation of the strained staples, however, renders the whole DNA origami structurally more flexible, so that it can more easily adjust its local and global conformations in order to accommodate electrostatic repulsion and relax most of the strain experienced by the remaining staples. This will lead to an increase in the apparent melting temperatures of the remaining staples and thus in a further broadening of the melting transition. At higher ionic strength, this effect is less pronounced because electrostatic inter-helix repulsion is mostly screened, so that the melting transition becomes narrower with increasing Mg^{2+} concentration. Interestingly, the width of the melting transition at 10 mM Mg^{2+} and above is notably smaller than the width of the calculated T_m distributions of the staples. A similar phenomenon is typically observed also for spherical nucleic acids and attributed to the high local salt concentration in the dense DNA monolayer surrounding the nanoparticle core, which changes during DNA melting.¹⁸¹ Such a cooperative effect is probably also responsible for the narrowing of the melting transition in the DNA origami nanostructures. When DNA melting sets in, dehybridization of the staples with the lowest individual T_m values leads to a simultaneous decrease in the local salt concentration, which in turn reduces the melting temperature of the remaining strands.

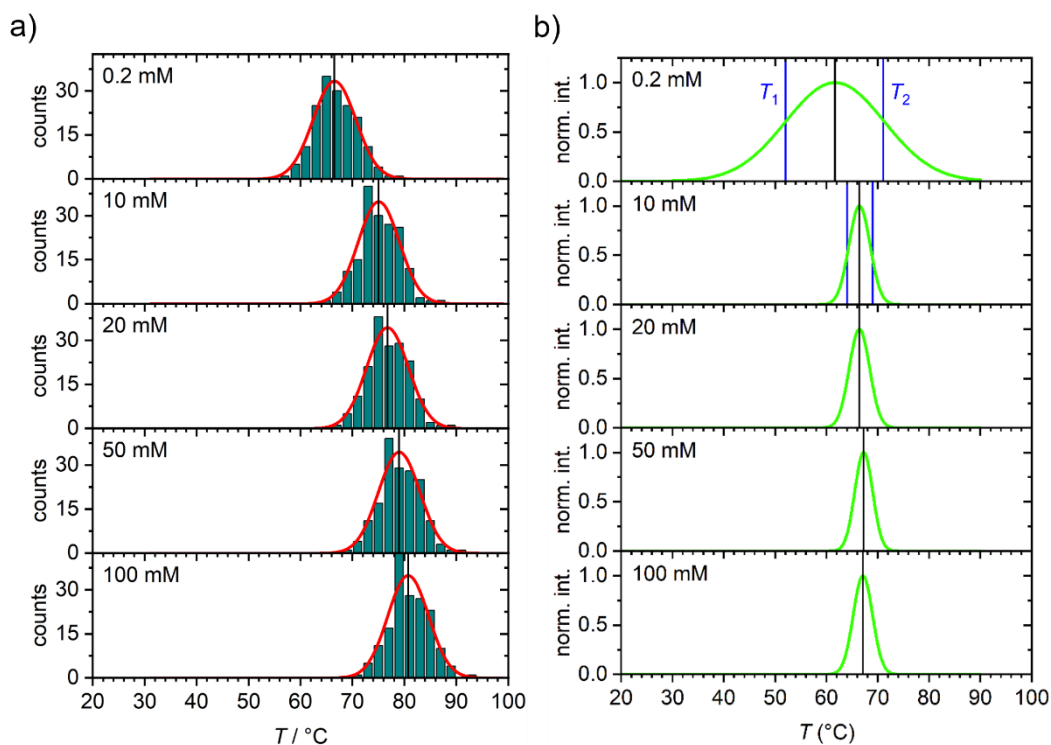


Figure 5.5 a) Calculated distribution of staple melting temperature for the DNA origami 6HB 21-bpCS at different Mg^{2+} concentrations. The red curves represent Gaussian fits to the distributions and the black vertical lines indicate the centers of the Gauss curves, corresponding to the ensemble T_m . b) Normalized melting transition of the DNA origami 6HB 21-bpCS at different Mg^{2+} concentrations obtained by fitting the negative derivatives of the recorded melting curves with several Gaussians. The black vertical lines indicate the centers of the Gauss curves, corresponding to the DNA origami T_m . The blue vertical lines in b) indicate temperatures T_1 and T_2 at which AFM images were recorded.

Another interesting difference between the calculated and the measured melting transitions in Figure 5.2 involves the T_m shift with increasing ionic strength. It appears that even though a similar shift to higher temperatures is observed in both cases upon increasing the Mg^{2+} concentration from 0.2 to 10 mM, the shift is somewhat smaller for the DNA origami T_m than for the staple ensemble T_m . At higher Mg^{2+} concentrations above 10 mM, barely any shift can be discerned in the melting transition of the DNA origami rectangle in Figure 5.2 b), whereas the calculated T_m distribution of the staples in Figure 5.2 a) continues to shift to higher temperatures, albeit at smaller increments than at lower concentrations.

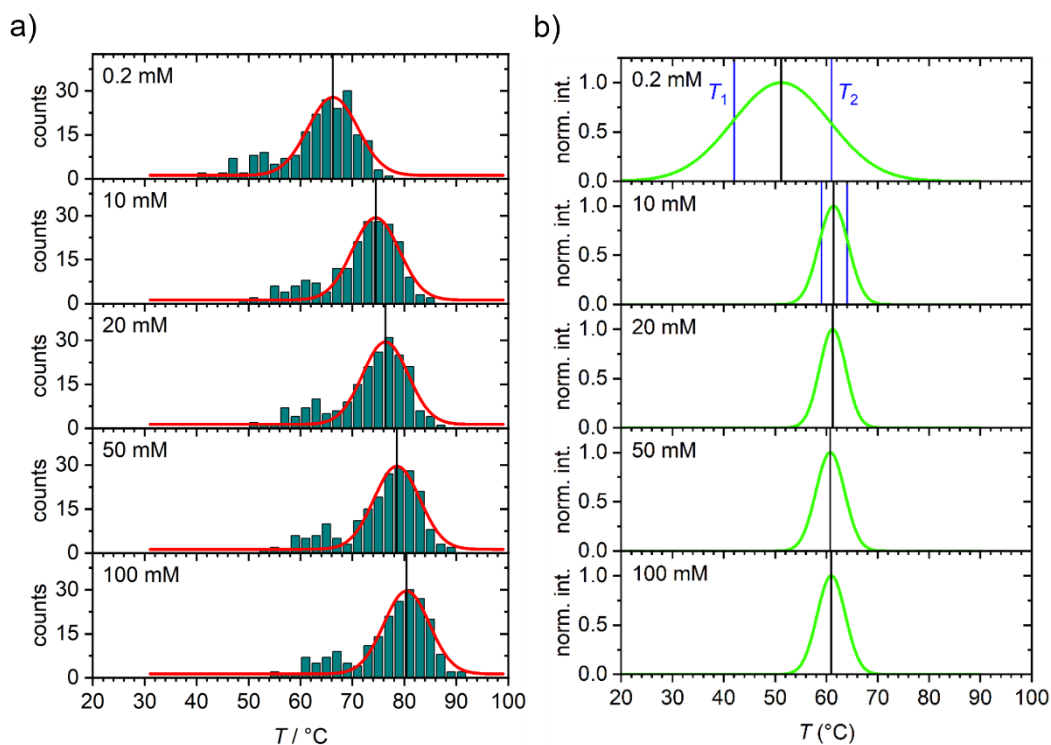


Figure 5.6 a) Calculated distribution of staple melting temperature for the DNA origami 24HB at different Mg^{2+} concentrations. The red curves represent Gaussian fits to the distributions and the black vertical lines indicate the centers of the Gauss curves, corresponding to the ensemble T_m . b) Normalized melting transition of the DNA origami 24HB at different Mg^{2+} concentrations obtained by fitting the negative derivatives of the recorded melting curves with several Gaussians. The black vertical lines indicate the centers of the Gauss curves, corresponding to the DNA origami T_m . The blue vertical lines in b) indicate temperatures T_1 and T_2 at which AFM images were recorded.

The calculated and measured T_m values at the different Mg^{2+} concentrations are quantitatively compared for all five DNA origami nanostructures in Figure 5.7. As can be seen, the calculated staple ensemble T_m values for all DNA origami increase linearly with the logarithm of the Mg^{2+} concentration. This kind of logarithmic scaling is regularly observed for duplex DNA and thus expected also for an ensemble of non-interacting duplexes.¹⁷¹ The measured DNA origami T_m values, however, do not follow this trend. For all five DNA origami nanostructures, a moderate increase in T_m is observed between 0.2 and 10 mM, after which the T_m saturates at a comparatively low value and becomes essentially independent of the Mg^{2+} concentration. This is a rather surprising observation, not only because the calculated ensemble melting temperatures predict a different behavior, but also because screening of electrostatic repulsion should play a more important role in the dense arrangements of duplexes within DNA origami

nanostructures. Therefore, one would rather expect a more pronounced effect of ionic strength on the melting temperature of a DNA origami nanostructure than on that of a single duplex.

Despite their T_m following similar trends, the plots in Figure 5.7 also reveal some differences between the five DNA origami nanostructures. In particular, there is an excellent agreement between the calculated and the measured T_m values at 0.2 mM Mg^{2+} for both the DNA origami rectangle and the 6HB 42-bpCS. For the triangle and the 6HB 21-bpCS, however, the measured T_m values are 4 to 5 °C lower than the calculated ones at this Mg^{2+} concentration. For the 24HB, this difference between both T_m values increases to about 15 °C. As already mentioned above, the two 6HB designs are identical in all aspects except the number of staple crossovers with the 21-bpCS design having twice as many as the 42-bpCS design. This increased number of staple crossovers was shown to result in an increased stiffness and a reduced stability at low ionic strength.²⁴ The latter is attributed to the high crossover density restricting ability the duplexes of the 6HB to undergo structural and conformational adjustments in response to increased electrostatic inter-helix repulsion. Therefore, an additional reduction in T_m at low Mg^{2+} concentrations compared to the calculated staple ensemble melting temperature as well as the 41-bpCS design is to be expected. The fact that a similar reduction in T_m compared to the corresponding ensemble T_m values is observed also for the DNA origami triangle suggests that this design has a similar rigidity despite its lower crossover density. Indeed, the Rothmund triangle is known to adopt a rigid cup-shaped conformation in solution,^{23,143} which may pose similar restrictions on conformational alterations as a high crossover density.

The 24HB displays the largest deviations from the calculated staple ensemble T_m values. This is in line with the above interpretation since the 24HB not only has a similar number of staple crossovers as the 6HB 21-bpCS design, but also the highest number of scaffold crossovers of all designs. Therefore, it can be assumed that the individual duplexes within the DNA origami are even more restricted in their ability to adjust to electrostatic repulsion, which leads to the observed further reduction in T_m . Remarkably, this large difference between the calculated and the measured T_m values at 0.2 mM Mg^{2+} generates an additional offset also at higher concentrations, so that at 100 mM Mg^{2+} a difference of about 20 °C is observed.

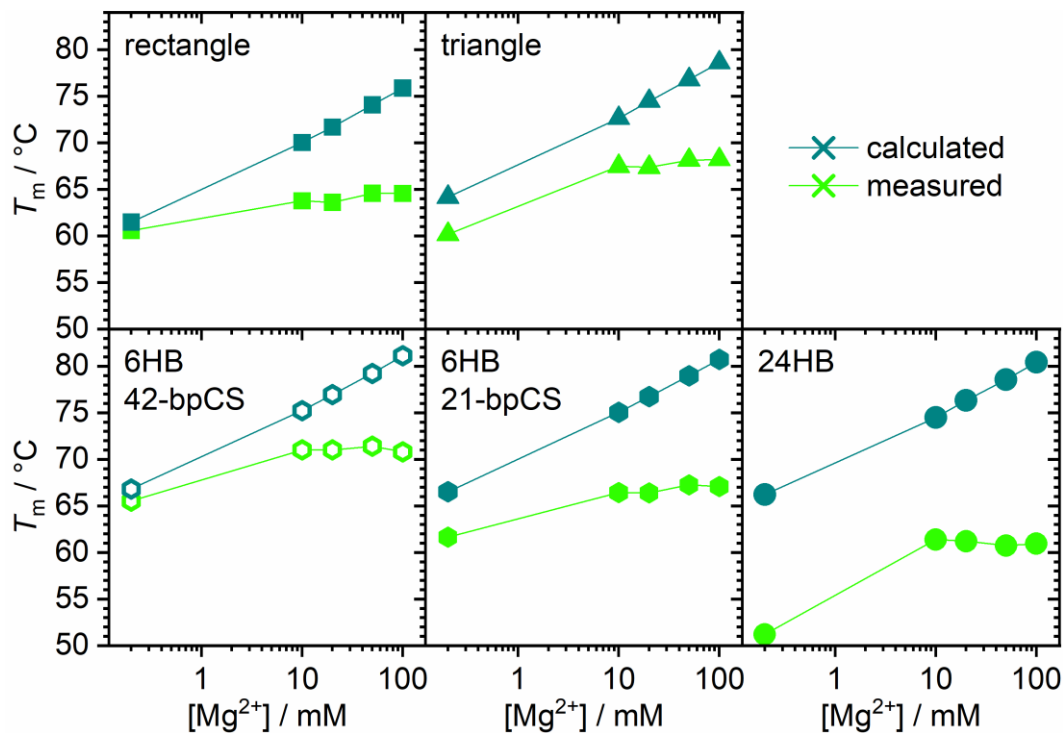


Figure 5.7 Calculated staple ensemble and measured DNA origami melting temperatures of all five DNA origami nanostructures in dependence of Mg^{2+} concentration. All melting temperatures are listed in table 5.1.

It was previously observed that fluorescence-based melting curves may underestimate the structural stability of DNA origami nanostructures at low temperatures because fluorometry is not sensitive enough to detect the dehybridization of individual staples with particularly low melting temperatures.²⁵ Nevertheless, the dissociation of only few staples may already lead to the structural collapse of the DNA origami nanostructure. Therefore, DNA origami melting was also assessed at the nanostructure level by AFM. For this, each of the five DNA origami nanostructures was incubated at constant temperature for 5 min in buffer containing 0.2 and 10 mM Mg^{2+} , respectively. For each condition, this was done at two selected temperatures $T_1 = T_m - w/2$ and $T_2 = T_m + w/2$, with w being the full width at half maximum (fwhm) of the Gaussian melting component (see Figures 5.2–5.6). As can be seen in the representative AFM images in Figure 5.8, denatured DNA origami are observed for all conditions. In most cases, however, the DNA origami nanostructures denatured at T_1 appear more compact or more structured than those denatured at T_2 , which mostly resemble pure scaffold. This is in line with the selected temperatures $T_1 < T_m < T_2$.

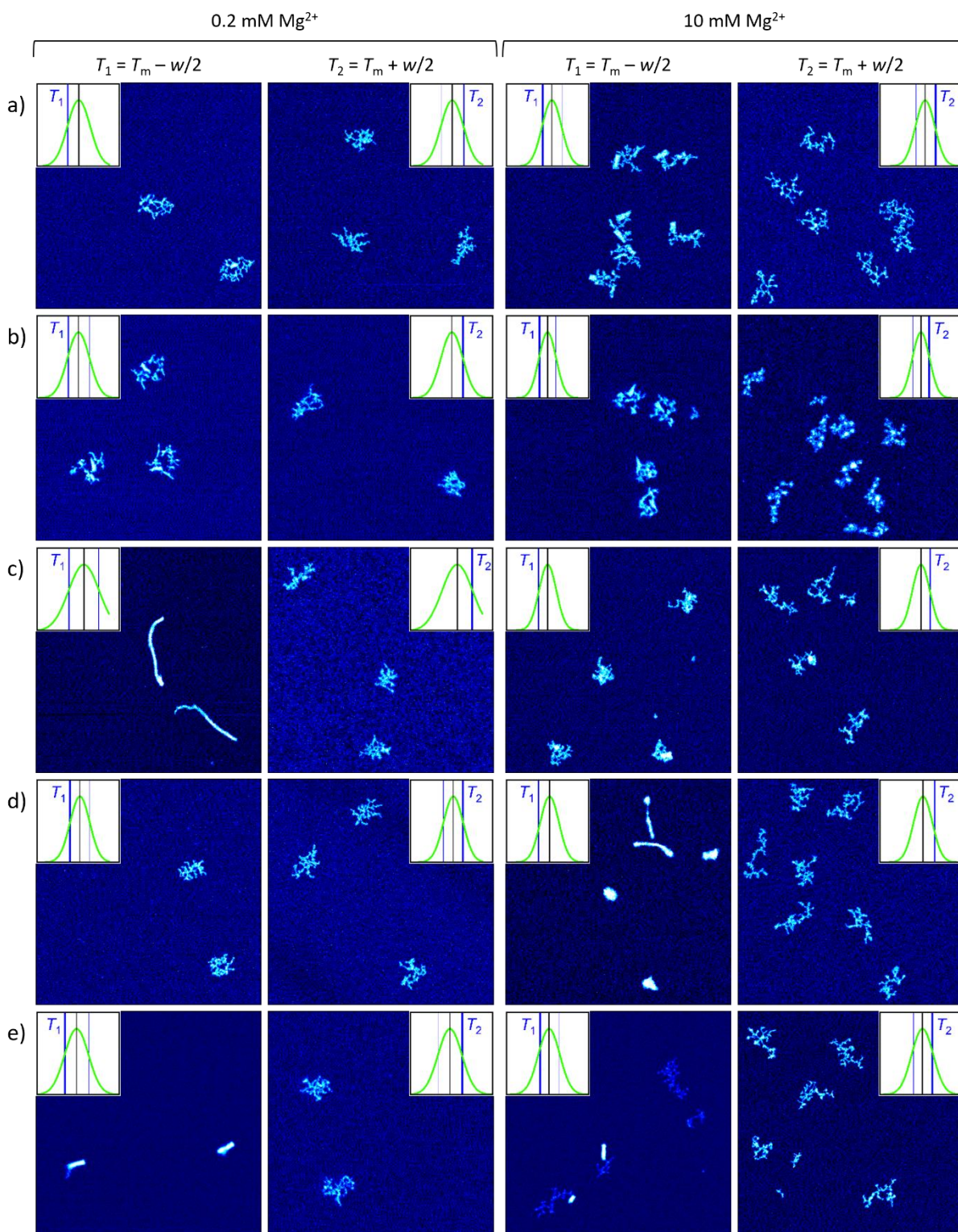


Figure 5.8 AFM images of DNA origami a) rectangles, b) triangles, c) 6HBs 42-bpCS, d) 6HBs 21-bpCS, and e) 24HBs recorded after incubation in 0.2 and 10 mM Mg²⁺ at selected temperatures T_1 and T_2 relative to the melting temperature T_m as indicated in the insets (see also Figures 5.2-5.6 and table

5.2). Height scales are 2.5 nm a)-d), and e) second and fourth row and 5 nm e) first and third row, respectively.

However, there are also some differences between the different DNA origami nanostructures. In particular, at T_1 , the rectangles, the triangles, and the 6HBs with 21-bpCS appear more compact and thus more intact in 10 mM Mg^{2+} than in 0.2 mM Mg^{2+} (Figure 5.8 a), b), and d)). This is rather surprising since T_1 and T_2 both are selected relative to the individual T_m observed under the respective conditions (see insets in Figure 5.8), so that the degree of denaturation observed at T_1 should be independent from the Mg^{2+} concentration. This counterintuitive observation can be explained by the large number of stabilizing Mg^{2+} salt bridges delaying the structural collapse of the DNA origami nanostructures even after a large number of staples have dehybridized. The exact opposite, however, is observed for the 6HBs with 42-bpCS, which remain mostly intact after incubation at T_1 in 0.2 mM Mg^{2+} (Figure 5.8 c)). In contrast, almost complete denaturation is observed in 10 mM Mg^{2+} . While the drastically enhanced stability at low Mg^{2+} concentration compared to the other shapes and designs is in line with previous observations and can be attributed to its high mechanical flexibility,^{22,24} it is not clear so far why this mechanism does not persist also at higher Mg^{2+} concentrations. It might be speculated that this counterintuitive behavior may be related to the sequence-dependence of the stabilizing effect of the Mg^{2+} ions, which will alter the pattern of staple dehybridization. This is also visible in the calculated staple T_m distribution shown in Figure 5.4, which displays slight changes upon increasing the Mg^{2+} concentration from 0.2 to 10 mM. This change in the staple melting pattern may result in some structurally important staples dehybridizing at T_1 in 10 mM Mg^{2+} but not in 0.2 mM Mg^{2+} . In the former case, this would lead to structural collapse, whereas in the latter case, the DNA origami may remain mostly intact as observed in Figure 5.8 c)). In order to support this assumption, the T_m distributions have been further analyzed by counting the staples with individual melting temperatures below T_1 for both Mg^{2+} concentrations. Indeed, at 0.2 mM Mg^{2+} , 23 staples fall in this category, while at 10 mM Mg^{2+} , the number increases to 26.

Table 5.1 Calculated staple ensemble (black) and measured DNA origami melting temperatures (green) in °C of all five DNA origami nanostructures in dependence of Mg^{2+} concentration.

	0.2 mM	10 mM	20 mM	50 mM	100 mM
rectangle	61.5	70.0	71.7	74.1	75.9
	60.6	63.8	63.6	64.6	64.6
triangle	64.2	72.6	74.5	76.8	78.6
	60.2	67.5	67.4	68.1	68.2
6HB 42-bpCS	66.8	75.3	76.9	79.2	81.1
	65.5	71.0	71.0	71.4	70.8
6HB 21-bpCS	66.5	75.1	76.7	79.0	80.7
	61.7	66.4	66.4	67.3	67.1
24HB	66.2	74.5	76.3	78.6	80.4
	51.2	61.4	61.2	60.7	60.9

Table 5.2. Measured DNA origami melting temperatures T_m and temperatures $T_1 = T_m - w/2$ and $T_2 = T_m + w/2$ (in °C) at which the samples in Figure 5.8 were incubated.¹⁸²

	0.2 mM Mg^{2+}			10 mM Mg^{2+}		
	T_1	T_m	T_2	T_1	T_m	T_2
rectangle	50.0	60.6	72.0	61.0	63.8	67.0
triangle	54.0	60.2	67.0	65.0	67.5	70.0
6HB 42-bpCS	51.0	65.5	80.0	69.0	71.0	73.0
6HB 21-bpCS	52.0	61.7	71.0	64.0	66.4	69.0
24HB	42.0	51.2	61.0	59.0	61.4	64.0

A similar yet slightly less pronounced behavior is observed also for the 24HB (see Figure 5.8 e)). This is rather surprising considering that such bulky 3D structures are typically even more sensitive toward low Mg^{2+} concentrations because of the high charge density requiring more efficient screening.²² As for the 6HB 42-bpCS, an explanation for this behavior may be found in the staple T_m distribution. However, in the case of the 24HB, the total number of staples with melting temperatures below T_1 does not change upon increasing the Mg^{2+} concentration from 0.2 to 10 mM. Nevertheless, there are small differences in the staple compositions of the respective subsets for each concentration. Such small variations may have a large impact on the

structural integrity of a DNA origami nanostructure under the given conditions, in particular as they may be further amplified by electrostatic inter-helix repulsion and mechanical strain.

5.3 Conclusion

In summary, the data presented in this work suggest that the thermal stability of DNA origami nanostructures is mostly determined by their mechanical properties with stiffer and more rigid designs in general having lower melting temperatures than more flexible ones. Nevertheless, even flexible DNA origami nanostructures have strongly reduced melting temperatures at high ionic strength compared to the calculated ensemble melting temperatures of their staple sets. In combination with the observation that T_m becomes independent of ionic strength under such conditions, this indicates that the design and mechanical properties of a given DNA origami nanostructure constitute a limit to its maximum T_m that can be achieved by increasing ionic strength. This is a rather remarkable finding since DNA origami stability at low ionic strength depends critically on the presence and availability of residual cations that screen electrostatic inter-helix repulsion.^{22,24,178} Once compensated by a sufficiently high concentration of cations, however, electrostatics do not seem to play a major role in DNA origami stability anymore.

The experiments have been complemented by AFM investigations in order to assess DNA origami melting also at the nanostructure level. For all DNA origami nanostructures at both high and low Mg^{2+} concentrations, AFM revealed stronger DNA origami denaturation at the end of the melting transition than at its start. However, while for three of the investigated DNA origami nanostructures (rectangle, triangle, 6HB 21-bpCS) increasing the Mg^{2+} concentrations appears to delay structural collapse during melting, the exact opposite was observed for two other DNA origami nanostructures (6HB 42-bpCS and 24HB). This is rather surprising since these two DNA origami designs are structurally and mechanically very different and should thus show different behaviors as well. It can only be speculated at this point that this is caused by that fact the stabilizing effect of ionic strength shows some sequence dependence, so that the pattern of staple dehybridization changes with increasing Mg^{2+} concentration.

The results provide further insights into the complex interplay of environmental factors and structural parameters that governs DNA origami stability. Most intriguingly, it has been presented evidence that the role of electrostatic repulsion in this context may not be as dominant as one would expect for structures with such a high charge density, at least not at moderate to

high ionic strength. Furthermore, the experiments also demonstrate how drastically even rather simple DNA origami designs such as 6HBs can deviate in their behavior from genomic duplex DNA because the duplexes within a given DNA origami nanostructure experience not only additional electrostatic inter-helix repulsion but also severe mechanical strain. Elucidating all the underlying correlations and contributing mechanisms will require further detailed biochemical and biophysical investigations with a special emphasis on DNA origami design factors.

5.4 Materials and Methods

5.4.1 Calculation of staple melting temperatures

Individual staple melting temperatures of all the staple strands of each DNA origami design were calculated using the “Hybridization of two Different Strands of DNA or RNA” application of the DINAMelt webserver.¹⁷² It is based on a statistical mechanical formalism that takes into account the whole ensemble of single- and double-strand species in solution and considers also mismatches, interior loops, bulges, and single-base stacking at the ends.¹⁸³ Each staple sequence was assumed to hybridize with its reverse complement at equal concentrations (2 nM). Sequence domains not hybridizing with the scaffold such as the poly-T overhangs of the 24HB²⁸ and the unpaired T spacers in the bridging staples of the triangle⁴ were omitted. The calculations were performed in oligomer mode for 10 mM Na⁺ and different concentrations of Mg²⁺ ranging from 0.2 to 100 mM.

5.4.2 DNA origami assembly

The DNA origami nanostructures (“tall” rectangle,⁴ Rothemund triangle,⁴ 6HB 42-bpCS,²⁴ 6HB 21-bpCS,²⁴ 24HB)²⁸ were assembled as previously described¹⁶¹ in 1xTAE buffer (Carl Roth) containing 10 mM MgCl₂ (Sigma-Aldrich) at tenfold excess of staples (Eurofins) to scaffold (Tilibit). In the assembly of the rectangle, all edge staples were omitted in order to avoid aggregation due to blunt-end stacking.⁴ The assembled DNA origami nanostructures were purified by spin filtering using Amicon Ultra-0.5 mL spin filters with 100 kDa molecular weight cut-off (Merck). Finally, the concentration of purified DNA origami was determined by

UV/vis absorption using an Implen Nanophotometer P330 and subsequently adjusted to a concentration of 100 nM.

5.4.3 Melting curve measurements and analyses

Melting curves were recorded using a JASCO fluorescence spectrometer FP-8200 with a water-cooled Peltier thermostatted cell holder. For this, the DNA origami samples in assembly buffer were diluted with TAE buffer containing different MgCl_2 concentrations to reach a DNA origami concentration of 2 nM in 1xTAE and the desired Mg^{2+} concentrations between 10 and 100 mM. For the experiments at 0.2 mM Mg^{2+} concentration, the samples were diluted in Tris buffer without EDTA to avoid complexation of the residual Mg^{2+} ions. The samples were further supplemented with SYBR Green (Jena Bioscience) at a final concentration of 1 μM , covered with aluminum foil to prevent photobleaching and incubated for 30 min at room temperature. Subsequently, 3 mL of the samples were transferred to a glass cuvette and fluorometric measurements were performed at 495 nm excitation and 522.5 nm emission with a bandwidth of 10 nm. The samples were heated from 20 °C to 90 °C with a temperature ramp of 1 °C/min. The fluorescence intensity was measured at temperature increments of 1 °C, resulting in a total number of 71 data points for each measurement. The thus recorded melting curves were analyzed using OriginPro 2023 (OriginLab) by calculating the negative derivative after smoothing with a fourth-order polynomial and an integration window of ten to twenty points, and fitting the resulting curves with multiple Gaussians.

5.4.4 AFM imaging

In order to visualize the degree of DNA origami denaturation by AFM, the different DNA origami nanostructures were incubated for 5 min at the desired temperatures and Mg^{2+} concentrations and subsequently cooled down to 20 °C using a Primus 25 advanced thermocycler (PEQLAB). Then, 2 μL of the solution was deposited on freshly cleaved mica and immediately covered with 100 μL of 1xTAE buffer containing 10 mM MgCl_2 . After 3 min of incubation, the sample was washed with about 5 mL of HPLC-grade water (VWR) and blow-dried with a stream of Ar. The dry sample was then imaged in air using a Bruker Dimension ICON AFM in ScanAsyst PeakForce Tapping mode with ScanAsyst-Air cantilevers. The

images were recorded with a size of $3 \times 3 \mu\text{m}^2$, a resolution of 1024×1024 px, and a line rate of 1 Hz.

6 Direct visualization of the drug loading of single DNA origami nanostructures by AFM-IR nanospectroscopy

6.1 Introduction

DNA nanostructure-based approaches have proven especially powerful in cancer therapy, where several studies have demonstrated successful tumor treatment *in vivo*.^{184–186} However, DNA nanocarriers are also increasingly explored with regard to applications in immunotherapy and in the treatment and prevention of infectious diseases.^{6,187,188} While numerous different therapeutic species can be transported by such nanostructures, including enzymes,¹⁸⁹ therapeutic nucleic acids,¹⁹⁰ and nanoparticles,¹⁹¹ DNA-based nanocarriers are mostly employed in the delivery of chemotherapeutic drug molecules.^{5,192} This is mainly because many of such chemotherapeutic drugs have a high affinity for DNA and can thus be easily loaded into the DNA nanostructures. This can be achieved using different non-covalent binding modes, including intercalation,^{81,193,194} groove-binding,^{84–86} or simple electrostatic binding.^{87,88,195}

Depending on the drug molecule in question, these rather straightforward drug loading approaches unfortunately often suffer from complications such as a competition of several different binding modes,^{28,86,196} limited accessibility of binding sites,^{86,197} and difficulties in the unambiguous detection of drug-DNA binding events. The latter is usually attempted by analyzing binding-specific UV-vis or fluorescence spectroscopic signatures, which may, however, be obscured by or sometimes even originate in other processes such as drug aggregation.²⁸ Unambiguous characterization of drug loading thus usually requires detailed analyses performed under different yet well-defined environmental conditions, often in combination with a variety of complementary analytical techniques.^{28,197}

In this work, the direct visualization of the drug loading of single DNA origami nanostructures is demonstrated for the first time. This is achieved by recording the characteristic infrared (IR) absorption of the DNA origami-bound drug molecules using AFM-IR nanospectroscopy.^{108,198} While this technique was previously used to analyze various polymers, proteins, viruses, and cells,^{108,198} its application to DNA nanostructures has not been reported yet. Using flat gold surfaces as substrates for immobilization, it was able to resolve the loading of single- and multilayer DNA origami nanostructures with the minor groove-binder methylene blue (MB),

which is a photosensitizer widely applied in anticancer, antimicrobial, and antiviral photodynamic therapy.¹⁹⁹ It has been furthermore shown that the intensity of a MB-specific IR absorption band increases with both MB concentration and the height of the DNA origami nanostructures, which in the present study ranged from about 1.5 to about 5 nm. The latter observation is attributed to an increase in the number of DNA-bound MB molecules located underneath the AFM tip and thus indicates that also DNA double helices located in the core of bulky 3D DNA origami nanostructures are accessible for MB loading.

6.2 Results and discussion

Because of the fragile nature of the DNA origami nanostructures investigated in this work, tapping-mode instead of contact-mode AFM-IR nanospectroscopy was employed. While this mode results in better topographic images and prevents the AFM tip to pick up molecules from the substrate surface, it is also less sensitive to the photothermal expansion of the sample. Therefore, we settled on using gold-coated substrates, which provide higher IR signals due to surface enhancement.²⁰⁰ However, typical gold films are comparably rough, which makes the identification of single-layer DNA origami nanostructures by AFM very challenging.²⁰¹ Thus, quasi-epitaxially grown template-stripped gold substrates have been employed,²⁰² which exhibit large atomically flat terraces and are sufficiently smooth to render adsorbed single-layer DNA origami visible in AFM images.²⁰¹ Figure 6.1 a) (left panel) shows an AFM image of blank DNA origami triangles⁴ adsorbed on a template-stripped gold surface. While the triangular shapes of most DNA origami can be resolved, many triangles are deformed and/or aggregated, so that the overall image quality is notably worse than for more common substrates for DNA origami immobilization such as mica. This can be attributed to the weaker interactions between the DNA origami and the gold surface and the larger surface roughness. Furthermore, the gold-coated AFM-IR tip has a larger tip radius than standard AFM probes, which leads to a further reduction in image quality. Nevertheless, the image quality is sufficient to identify individual DNA origami nanostructures. Therefore, IR spectra of the bare gold surface and a large DNA origami cluster were recorded (see Figure 6.1 a), central panel). Within the wavenumber range from 750 to 1900 cm^{-1} , both spectra are almost identical and show no DNA-specific bands, even though DNA should exhibit several strong IR absorption bands in this wavenumber range.²⁰³ The height profile across the DNA origami cluster whose IR spectrum was recorded is also shown in Figure 6.1 a) (right panel) and reveals that the cluster has an

average height of about 4 nm. In the dry state, this corresponds to a vertical stack of three to four double helices. The fact that even for this rather large number of contributing double helices no DNA-specific IR absorption bands are detected can most likely be attributed to the comparatively low sensitivity of tapping mode AFM-IR.

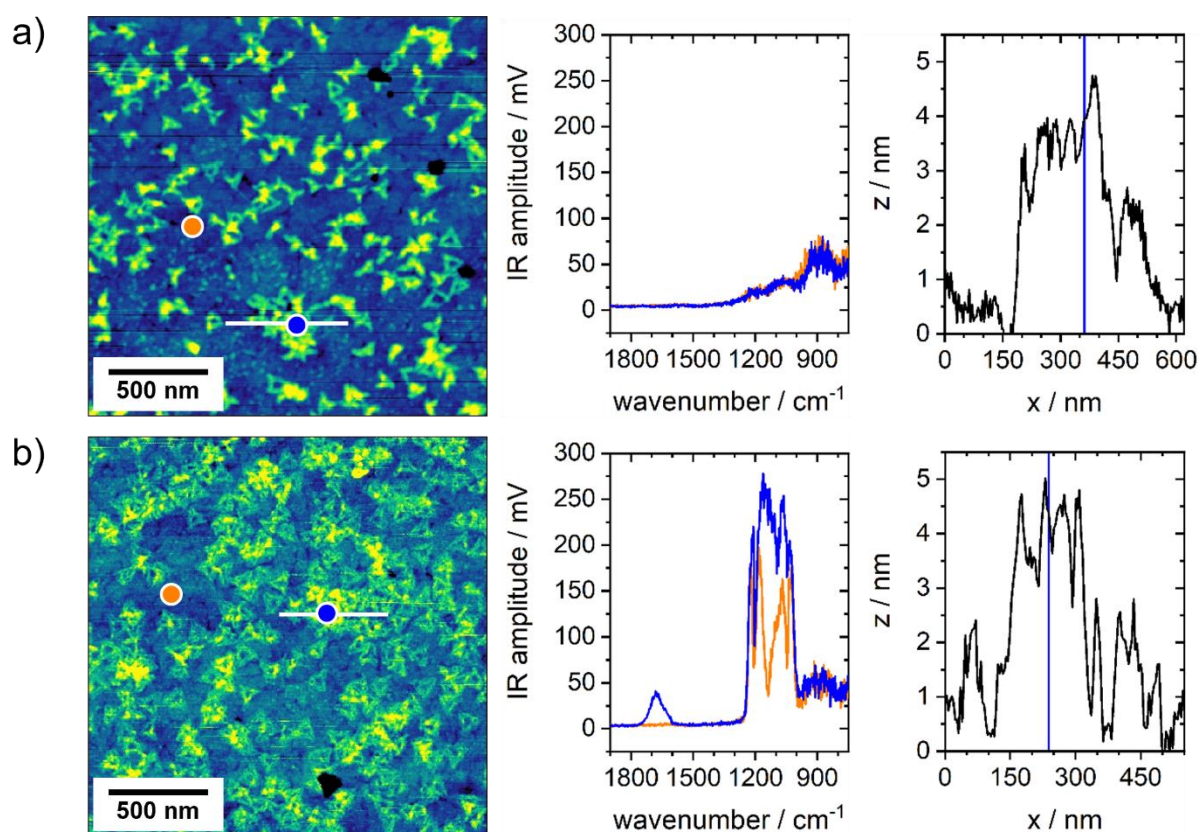


Figure 6.1 AFM-IR investigation of a) blank and b) MB-loaded DNA origami triangles adsorbed on template-stripped gold surfaces. Topographic AFM images are shown on the left. Height scales are 5 nm. IR spectra (center) of the bare gold substrates (orange) and the DNA origami nanostructures (blue) were recorded at the positions indicated in the corresponding AFM images. Height profiles (right) were extracted along the white lines in the topographic AFM images. The vertical lines in the height profiles indicate the points where the IR spectra were recorded. MB-loading was performed at a MB and a DNA origami concentration of 20 μM and 1 nM, respectively.

Then, MB-loaded DNA origami triangles were evaluated. Loading was achieved by mixing the assembled and purified DNA origami triangles (1 nM) with an excess of MB (20 μM) in standard assembly buffer (10 mM Tris supplemented with 10 mM MgAc_2). At such high Mg^{2+}

concentrations, MB is preferentially binding to the minor groove of the DNA instead of intercalating between the base pairs.⁸⁶ The MB-loaded DNA origami triangles were then adsorbed on a template-stripped gold surface. As can be seen in the topographic AFM image in Figure 6.1 b) (left panel), MB-loading does not have a pronounced effect on DNA origami adsorption at this surface. The corresponding IR spectra, however, differ clearly from those recorded in the absence of MB. Already for the bare gold surface, several, partially overlapping IR absorption bands can be observed in the spectral region from 1000 to 1250 cm^{-1} , which correspond to known MB absorption bands.²⁰⁴ This indicates that free MB from solution is adsorbing on the gold surface, which is a well-established phenomenon.^{205,206} The IR spectrum recorded on a DNA origami cluster of similar height as the one selected in Figure 6.1 a) shows similar IR absorption bands in this spectral region, which on average, however, have higher intensities (Figure 6.1 b), central panel). Furthermore, the spectrum also shows a faint absorption band between 1600 and 1700 cm^{-1} , which can be assigned to MB as well and corresponds to the C=C and C=N heterocycle stretching vibrations.²⁰⁴ It should be noted that while the absolute position of this particular absorption band depends on the environment and the binding state of MB, it is almost always observed with similar intensities in the wavenumber range from about 1600 to 1700 cm^{-1} and may thus serve as a MB-specific marker band also in the case of intercalative DNA binding.^{204,207-210} The observed increases in the intensities of the MB-specific absorption bands at the positions of the adsorbed DNA origami can be explained by local variations in the surface density of MB molecules due to their specific binding to the DNA origami triangles. The MB-specific bands between 1000 and 1250 cm^{-1} and between 1600 and 1700 cm^{-1} can also be resolved in the IR reflection absorption spectrum of the same sample investigated in Figure 6.1 b) as can be seen in Figure 6.2. However, the bands are less defined and overlaid with several DNA-specific peaks and a rather high level of noise.

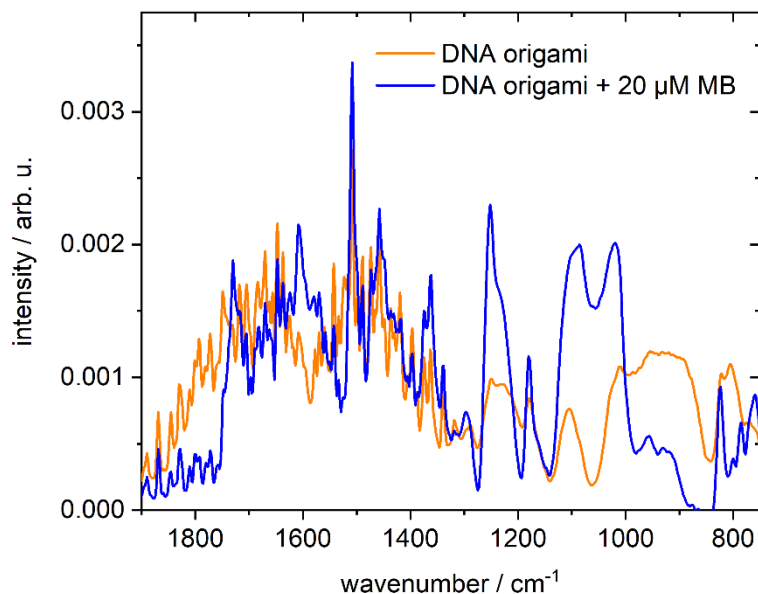


Figure 6.2 IR reflection absorption spectra of the a) blank and b) MB-loaded DNA origami samples investigated in Figure 6.1. The measurements were performed by using a Bruker Vertex 70 spectrometer with a LN-MCT detector. Reflection spectra were recorded at an incident angle of 45° with a spectral resolution of 4 cm⁻¹ and accumulated over 256 scans. A bare gold substrate was used as a reference.

Next, it was investigated whether DNA origami triangles loaded with different MB concentrations can be distinguished according to their IR signatures. To this end, DNA origami samples loaded at different MB concentrations of 5 μM, 10 μM, and 20 μM have been prepared. To ensure comparability of the measurements, all three samples were measured with the same AFM-IR probe and under identical scan conditions. In addition, to minimize the impact of artifacts originating from the AFM tip picking up MB molecules during scanning, we measured the lowest concentration first and the highest concentration last. As can be seen in the central panel of Figure 6.3 a), at a MB loading concentration of 5 μM, no MB-specific absorption bands can be identified in the IR spectrum. Nevertheless, an IR map of the surface area was also recorded shown in the topographic AFM in the left panel of Figure 6.3 a). For this, the IR absorption band of 1650 cm⁻¹ was chosen that was observed in Figure 6.1 b) to be specific for MB-loaded DNA origami. As can be seen in the right panel of Figure 6.3 a), this map shows mostly background noise, and no DNA origami can be identified. The only visible features are two bright spots in the lower right quadrant, which correspond to two large DNA origami aggregates (see white arrows in Figure 6.3 a)). This indicates that the DNA origami

triangles are loaded with MB, but to such a low extent that identification by AFM-IR is only possible when several DNA origami are stacked on top of each other.

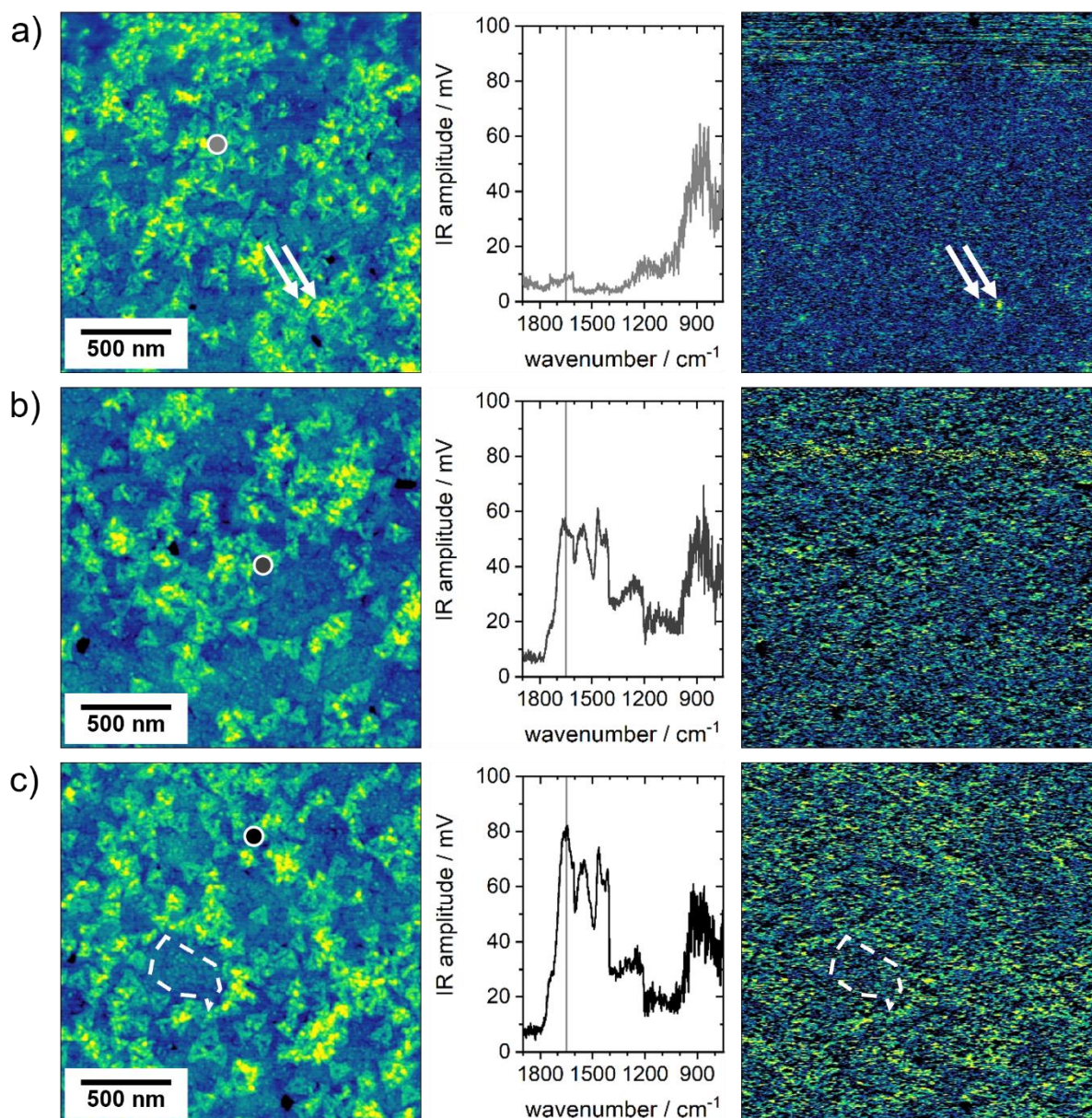


Figure 6.3 Topographic AFM images (left), IR spectra (center), and corresponding IR maps (right) of MB-loaded DNA origami triangles adsorbed on template-stripped gold surfaces. MB-loading was performed at a DNA origami concentration of 1 nM and a MB concentration of a) 5 μM , b) 10 μM , and c) 20 μM , respectively. The topographic AFM images have a height scale of 5 nm. The IR spectra were recorded at the positions indicated in the topographic AFM images. The IR maps have an IR amplitude scale of 1.5 mV and were recorded at a wavenumber of 1650 cm^{-1} as indicated by the vertical lines in the IR spectra. The white arrows in a) indicate the positions of two features that can be identified in the

IR map. The white broken lines in c) indicate a surface region devoid of any DNA origami that shows a lower IR signal than the surrounding DNA origami-covered regions.

At a MB concentration of 10 μM , absorption bands appear in the IR spectrum shown in Figure 6.3 b). These include the previously observed absorption band centered at about 1650 cm^{-1} , as well as some new bands in the range between 1200 and 1600 cm^{-1} . These lower-wavenumber bands could not be observed in the previous experiment (see Figure 6.1 b)), while the previously observed features in the range below 1200 cm^{-1} have disappeared. These discrepancies most likely originate in tip-to-tip variations in the employed cantilevers and highlight the importance of using the same AFM-IR probe when attempting to compare different samples. However, since surface enhancement is a plasmonic effect, also variations in surface topography and in particular surface roughness, for instance due to different grain sizes or terrace orientations, may contribute to the observed variability in the recorded IR spectra.²¹¹ The IR map at 1650 cm^{-1} in Figure 6.3 b) shows a stronger background signal than for 5 μM MB, which also appears more structured. Upon close comparison of the IR map and the corresponding topographic AFM images, it is possible to attribute regions of higher IR intensity to DNA origami aggregates, whereas those of lowest intensity correspond to surface areas devoid of adsorbed DNA origami. These features, albeit rather faint, are indicative of stronger MB-loading at a MB concentration of 10 μM .

At 20 μM MB, the MB-specific absorption bands already observed at a concentration of 10 μM become stronger in intensity (see Figure 6.3 c)). The number and position of spectral features remains the same, so that the recorded spectrum is still rather different from the one shown in Figure 6.1 b), even though the samples were prepared under identical conditions. This further supports the above interpretation that the employed AFM-IR probe has a strong impact on the actual shape of the recorded spectra. Because of the increased intensity of the 1650 cm^{-1} IR band, also the features in the corresponding IR map become more pronounced, so that it can now be clearly correlated with surface topography, with regions of larger IR signals corresponding to surface areas exhibiting adsorbed DNA origami. However, because of the comparatively large image size, it has not been able to resolve single DNA origami triangles in the IR map.

The AFM-IR measurements presented in Figure 6.3 clearly show that stronger IR signals are obtained from regions that exhibit a pile-up of DNA origami multilayers. This is not surprising,

considering that the DNA origami triangles have a thickness of only one double helix, which results in only a few MB molecules contributing to their thermal expansion upon resonant IR absorption. Therefore, next, different DNA origami shapes with different thicknesses have been investigated. For this, DNA origami six-helix bundles (6HBs) and 24-helix bundles (24HBs), in addition to the single-layer DNA origami triangles have been chosen. The nominal thicknesses of these DNA origami shapes in solution are 2 nm (triangles), 6 nm (6HBs), and 12 nm (24HBs).¹³⁷ Even though adsorption on the gold surface and subsequent drying will result in a partial collapse of the DNA origami nanostructures, the three shapes will still exhibit distinctly different heights.

To allow for a direct comparison between the different MB-loaded DNA origami shapes, all three samples were mixed and adsorbed together on one gold surface. Furthermore, to enable the clear distinction of the different DNA origami shapes, the scan size was reduced to 1 x 1 μm^2 . As can be seen in the corresponding topographic AFM image shown in Figure 6.4 a), the DNA origami triangles can be clearly resolved, even though their shapes are severely distorted by the roughness of the underlying gold surface. This surface-induced distortion is also evident for the filament-like 6HBs, which have a slightly larger height than the triangles and wind across grain boundaries. The shorter and thicker 24HBs, on the other hand, rather appear as rigid rods with barely any notable distortions. In the corresponding IR map in Figure 6.4 b), all three DNA origami shapes can be identified, albeit with very different signal intensities. While the triangles appear only as slight modulations of the background noise, the 6HBs can be distinguished more easily. The 24HBs have the highest IR signal and are visible as bright and well-defined rods.

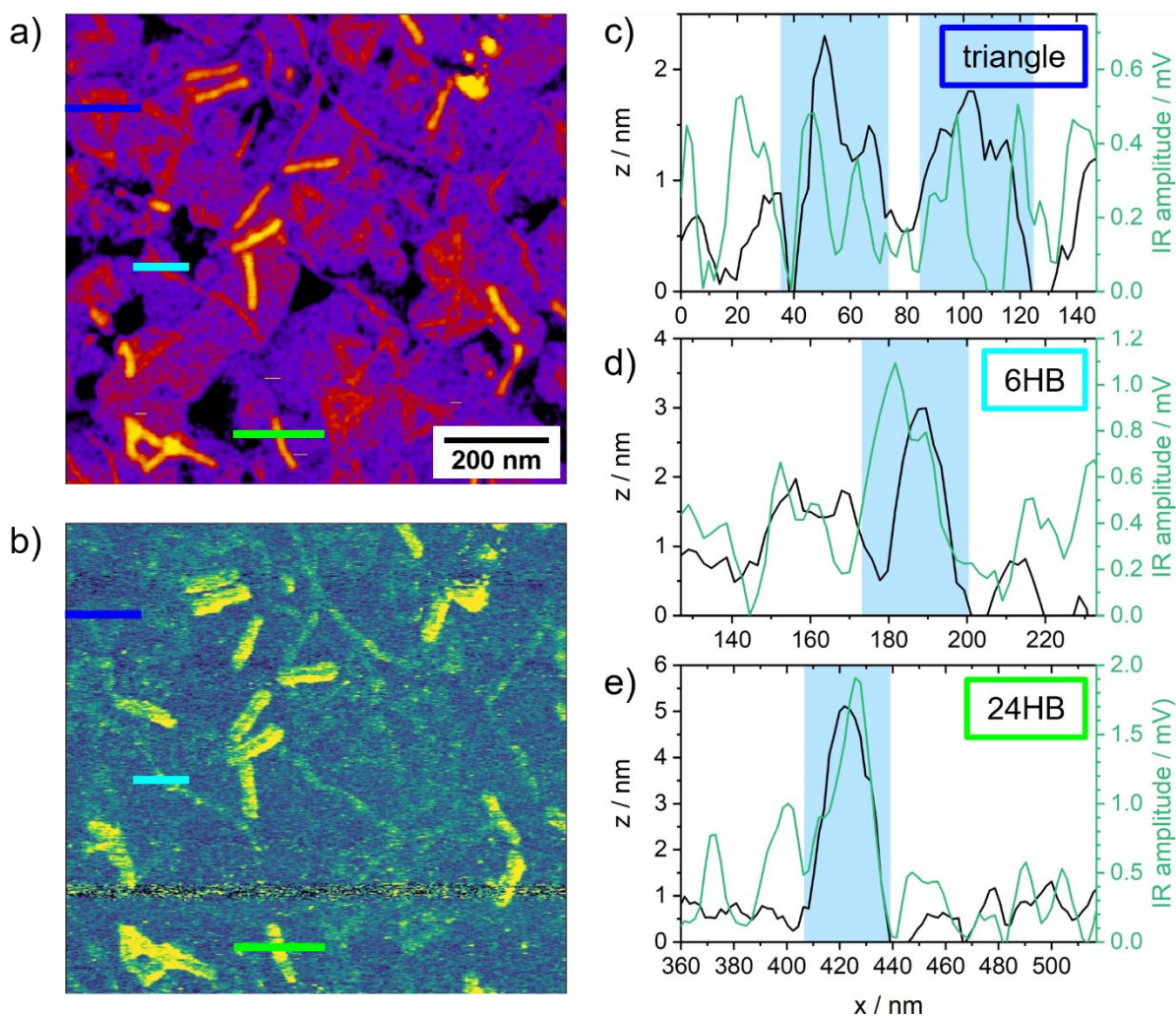


Figure 6.4 a) Topographic AFM image and b) corresponding IR map recorded at 1650 cm^{-1} showing MB-loaded DNA origami triangles, 6HBs, and 24HBs adsorbed on the same gold surface. The topographic AFM image has a height scale of 8 nm and the IR map has an IR amplitude scale of 1.5 mV. Height (black) and IR amplitude (green) profiles of selected DNA origami shapes (c-e)) have been extracted along the horizontal bars: c) blue – triangle, d) cyan – 6HB, e) green – 24HB. The features in the profiles attributed to the DNA origami are indicated by the shaded areas.

In order to assess the correlation between the surface topography and the IR map, height profiles of selected DNA origami nanostructures are plotted in Figure 6.4 c)-e) and overlaid with the corresponding IR amplitude profiles. For the DNA origami triangle (see Figure 6.4 c)), the two single-layer trapezoids in the height profile can be clearly seen, which have a height of about 1.5 nm. In the corresponding IR amplitude profile, similar features at roughly the same positions can be identified, which, however, have intensities comparable to the level of the

background noise. This is in agreement with the IR map in Figure 6.4 b), in which the DNA origami triangles are characterized only by a statistical accumulation of IR amplitude values slightly higher than the background. In contrast, the 6HBs have clearly higher IR amplitudes, which is also evident from the IR amplitude profile in Figure 6.4 d). Here, the intensity in the region associated with the 6HB in the height profile has an about two-fold higher IR amplitude than the background noise. This increase in the IR amplitude signal correlates fairly well with the increased height of the adsorbed 6HBs of 2.5 nm. For the 24HB (see Figure 6.4 e)), this is even more pronounced as both height and IR amplitude values are doubled again. The adsorbed 24HB has a height of about 5 nm and the corresponding IR amplitude profile has reached a peak value of almost 2 mV, compared to an average level of background noise of about 0.5 mV.

These observations clearly demonstrate that the height of the DNA origami nanostructures correlates with the intensity of the IR signal because more DNA double helices are located under the AFM tip that can contribute to the overall photothermal expansion. Since the data shown in Figure 6.4 b)-e) was obtained at 1650 cm^{-1} , i.e., for excitation of the loaded MB molecules, this is direct evidence that also double helices located in the core of the bulky 3D 24HBs are accessible for MB loading. This is in accordance with previous spectroscopic investigations, which revealed similar maximum MB loading densities of 0.45 to 0.48 MB molecules per nucleotide for the DNA origami triangle, the 6HB, and a bulky sixty-helix bundle under similar buffer conditions.⁸⁶ It should be mentioned at this point, however, that also the DNA itself may contribute to this overall signal because thymine and adenine also have absorption bands in the vicinity of 1650 cm^{-1} .²⁰³ Nevertheless, the IR spectrum of the MB-free DNA origami cluster shown in Figure 6.1 a) does not exhibit any peaks in this spectral range, even though it is of similar height as the 24HBs. Therefore, it can be assumed that MB is the major, if not sole, contributor to the IR band at 1650 cm^{-1} also for the multilayer 24HBs.

In this context, it is also interesting to note that in Figure 6.4 b), the 24HBs seem to display a less pronounced structure-to-structure variation in the overall IR signal intensity than the 6HBs and the triangles. This may be related to the fact that MB molecules bound at the outer surfaces of the DNA origami are always in direct contact with the gold substrate or the tapping AFM tip. Therefore, their IR absorption will be more sensitive to topographic and cantilever variations, whereas MB molecules bound to inner helices may yield less sensitive signals. This might result in multilayer DNA origami nanostructures providing more reliable and reproducible spectroscopic signatures.

6.3 Conclusion

In this work, the application of AFM-IR nanospectroscopy to directly visualize the loading of single- and multilayer DNA origami nanostructures with the minor groove-binding drug MB has been demonstrated. DNA origami immobilization on flat template-stripped gold substrates enabled the realization of tapping-mode AFM-IR with minimal sample interference. While any DNA-specific IR bands could not be resolved in this way, strong signals associated with MB were observed. Single MB-loaded DNA origami nanostructures could be clearly resolved in high-resolution IR maps and the occurrence of MB-specific IR absorption correlated well with the topographic signals of the DNA origami nanostructures.

Even though it has been observed that the number of absorption bands and their relative intensities in the recorded IR spectra may vary drastically from cantilever to cantilever and possibly substrate to substrate, their association with MB could be verified by adjusting the MB concentration used for drug loading, which was found to scale with the intensity of the respective absorption bands. By comparing single- (2D) and multilayer (3D) DNA origami nanostructures, it could further be shown that the IR signal intensity of the loaded MB increases with the thickness of the DNA origami nanostructures. This also indicates that DNA double helices located in the core of bulky 3D DNA origami nanostructures are accessible for MB loading.

Since AFM-IR provides true chemical information in the form of IR absorption spectra, this approach is not limited to MB but can be used to visualize the loading of DNA nanostructures with any drug molecule that exhibits specific and intense IR absorption bands. This in particular includes the intercalating chemotherapeutic agent doxorubicin (DOX),²¹² which has frequently been used in combination with DNA nanocarriers^{80,194,213–215} but undergoes numerous and highly environment-dependent interactions, so that the unambiguous verification of successful DOX loading is rather challenging.²⁸ However, it should be mentioned that DOX intercalation leads to lower maximum loading densities of only about 0.23 DOX molecules per nucleotide.²⁸ This is because intercalation requires structural alterations such as duplex unwinding, which limits the general accessibility of the base pairs. Lower loading densities in turn will result in lower intensities of the DOX-specific IR absorption bands. Even when selecting strong absorption bands of DNA-bound DOX such as the ones between 1000 and 1100 cm^{-1} or

between 1600 and 1700 cm^{-1} ,²¹⁶ the reduced loading densities will make the visualization of DOX loading in single-layer DNA origami nanostructures rather challenging. Because of the strongly increased signal intensities observed for the MB-loaded 24HBs in Figure 6.4, however, it can be assumed that multilayer DNA origami nanostructures will present less of a challenge.

A general limitation of the presented approach lies in the fact that imaging is not quantitative, so that the absolute loading density cannot be determined directly. Integrating the IR signal intensity over a complete DNA origami and comparing it to a reference sample with known loading density, for instance determined by UV/Vis or fluorescence spectroscopy, may provide some semi-quantitative loading information. This approach applied to different DNA origami nanostructures with different numbers of layers may even enable the generation of quantitative calibration curves that correlate IR absorption intensity with DNA origami thickness and loading density. For this, however, the effects of the cantilever and the substrate topography on the quality and intensity of the recorded spectra need to be better understood and ideally controlled. Only more detailed future investigations may verify whether this is indeed possible. Nevertheless, it can be concluded that AFM-IR has the potential to become an invaluable tool for verifying and possibly quantifying drug loading of DNA origami nanostructures and optimizing drug loading protocols.

6.4 Materials and Methods

6.4.1 DNA origami assembly and MB loading

The DNA origami nanostructures employed in this work were based on the original designs of Rothmund⁴ (triangle), Bui et al.²⁹ (6HB), and Ijäs et al.²⁸ (24HB). DNA origami assembly was performed as previously described¹³⁷ in 10 mM Tris buffer (Sigma-Aldrich) containing 10 mM MgAc_2 (Sigma-Aldrich) using scaffold and staple strands purchased from Tilibit and Eurofins, respectively. Triangular DNA origami were PEG purified²¹⁷ by diluting 200 μl of the DNA origami sample in 600 μl 10 mM Tris/ MgAc_2 and mixing it with 800 μl of PEG buffer containing 1xTAE, 15 % PEG-8000 (w/v) and 505 mM NaCl. Next, the solution was centrifuged at 14,000 rcf for 30 min at 18 °C. After removing the supernatant, the precipitate was re-dissolved in 35 μl of 10 mM Tris/ MgAc_2 overnight. 6HB and 24HB were purified by spin filtering using Amicon Ultra-0.5 mL spin filters with 100 kDa molecular weight cut-off (Merck). The DNA origami concentrations were determined by UV-vis absorption using an

Implen Nanophotometer P330 and adjusted to a concentration of 100 nM. MB loading was performed as previously described⁸⁶ by mixing the DNA origami triangles (1 nM) in assembly buffer supplemented with MB (Sigma-Aldrich) at a concentration of 5, 10, and 20 μ M, respectively. The experiment with the three mixed DNA origami shapes was performed using a concentration of 0.5 nM for the triangles and 6HBs and 1 nM for the 24HB. The MB concentration was again 20 μ M.

6.4.2 DNA origami immobilization on template-stripped gold substrates

Template-stripped gold substrates were prepared as previously described.²¹⁸ Right after stripping, 200 μ l of the DNA origami samples were deposited on the gold surfaces, incubated for 1.5 h, subsequently washed with water, and blow-dried in a stream of Ar.

6.4.3 AFM-IR nanospectroscopy

The so-prepared samples were analyzed by AFM-IR nanospectroscopy using a Bruker NanoIR3s system equipped with a tunable OPO/DFG Carmina laser (APE). AFM-IR was performed in tapping mode using gold-coated PR-EX-TNIR-A cantilevers (Bruker). The laser power of the IR source was set to a value of 24.45 % throughout all measurements. The images were recorded with a resolution of 512 x 512 px and a scan rate of 0.3 and 0.5 Hz, respectively. Spectra are averages of ten individual single-point spectra recorded at the same position.

7 Conclusion

In this work, the biophysical complexity of DNA origami nanostructures interactions in various molecular and ionic environments was investigated.

In chapter 4, stability studies of various DNA origami nanostructures under various chaotropic conditions have been performed.

First, it was found that the anionic species chloride Cl^- and sulfate SO_4^{2-} of the chaotropic agent Gdm^+ play a significant and thus differential role in the stability of DNA origami triangles at different temperature and concentration conditions. It was revealed that GdmCl promotes a Gdm^+ -induced DNA origami denaturation via significant heat capacity changes upon heating compared to Gdm_2SO_4 due to a more water-like and less charged hydration shell of GdmCl in solution. In contrast, Gdm_2SO_4 appears to form ion pairs in solution and consequently has much lower effect on heat capacity changes, i.e., Gdm -induced DNA origami denaturation.¹³⁶

In the next experiments, the anionic variety of Gdm -salt was further extended with GdmSCN and time dependent stability investigations on DNA origami triangles at different temperatures were performed. It could be shown that GdmSCN has the highest denaturing potency, followed by GdmCl and Gdm_2SO_4 , having the lowest activity. Interestingly, already within 15 min all DNA origami triangles were complete denatured for 2 M GdmSCN and 40 °C. In contrast, kinetic results of GdmCl and Gdm_2SO_4 have shown a significantly slower denaturation time at comparable concentrations and temperature conditions. Furthermore, while DNA origami triangles in GdmSCN and GdmCl were completely denatured at certain incubation time, the structural integrity of DNA origami were still existing in Gdm_2SO_4 after the maximum incubation time of 90 min at 50 °C.

Finally, in the same chapter, the stability of six different DNA origami designs, i.e., the 2D Rothemund triangle,⁴ the “tall” rectangle,⁴ a Z shape,²⁷ 6HB 42-bpCS and 6HB 21bp-CS,²⁴ and 24HB²⁸ in three different types to chaotropic salts, i.e., GdmCl and Gdm_2SO_4 as well as TPACl have been investigated. The incubation of all six different DNA origami designs in Gdm_2SO_4 up to 3 M has barely shown a structural effect. In contrast, already much lower concentrations of 1.5 M of TPACl completely denatured all different DNA origami shapes. The incubation of all DNA origami designs in GdmCl up to 6 M has shown a denaturation activity in between

TPACl and Gdm₂SO₄. Although the chaotropic activity of Gdm⁺ and TPA⁺ is adequately stated based on the Hofmeister series, it can be assumed that the different chemical properties between both cations lead to the significant alteration in Gdm⁺- and TPA⁺-induced DNA origami denaturation activity, respectively. Besides that, the different DNA origami nanostructures have shown a superstructure dependence with regard to chaotropic salt denaturation. The strongest difference could be observed for the 6HB with 42-bpCS, that evidently seemed to exhibit the highest stability. Here, incubation of these in 6 M GdmCl and 0.5 M TPACl resulted in almost completely intact 6HB with 42-bpCS, whereas all other five DNA origami designs have been denatured. The results indicate a high superstructure dependence of DNA origami nanostructures in chaotropic-induced denaturation, in which strain-promoted melting of staples might play a crucial role.

Overall, the work in chapter 4 remarkably illustrated the complexity of DNA origami nanostructures interaction under different chaotropic conditions. It could be shown that various factors, i.e., incubation temperature, and time, as well as the type of chaotropic agent, its counterions, and the DNA origami design itself have an interdependent effect on the stability of DNA origami nanostructures.

In chapter 5, the thermal stability of five different DNA origami nanostructure designs, i.e., the 2D “tall” rectangle,⁴ the 2D Rothmund triangle,⁴ 6HB 42-bpCS and 6HB 21bp-CS,²⁴ and 24HB²⁸ have been investigated under different Mg²⁺ concentrations and compared calculated melting temperatures values. It could be observed that while for very low Mg²⁺ concentrations of 0.2 mM most of the DNA origami designs besides 24HB have shown comparatively similar results in the melting temperatures T_m as the calculated ones, higher Mg²⁺ concentrations resulted in a quasi-plateau of T_m becoming independent of ionic strength with substantial deviations to theoretical calculated values. Furthermore, a shape dependent melting behavior in the range of the melting temperature could be observed leading to the assumption that, again, rigidity properties but also sequence dependence may play a role in thermal stability of DNA origami structures in different ionic environments.

In chapter 6, the drug loading of minor groove-binding methylene blue (MB) on single DNA origami nanostructures has been visualized by AFM-IR nanospectroscopy for the first time. Therefore, MB-loaded DNA origami triangles were adsorbed upon flat, surface enhanced template-stripped gold surfaces to increase the IR signal from photothermal excitation. IR spectra of the gold surface and drug-loaded DNA origami triangles with different MB

concentration were obtained revealing MB-associated IR peaks correlating with MB concentration. In addition, performing IR imaging at 1650 cm^{-1} resolved MB-loaded DNA origami triangles. Applying simultaneously three different DNA origami nanostructure designs, i.e., 2D Rothemund triangle,⁴ 6HB (42-bpCS),²⁹ and 24HB²⁸ for IR imaging at 1650 cm^{-1} revealed a shape dependence in IR signal, showing the highest signal intensity for the thickest DNA origami nanostructure, i.e., 24HB. This observation might lead to the assumption that MB loading also occurs in between the cored double strands of the 3D 24HB and thus increasing the signal. Overall, this work demonstrated the upcoming potential of AFM-IR based applications for quantitative and qualitative drug-loading measurements of DNA origami nanostructures.

8 References

- 1 T. D. Pollard, W. C. Earnshaw and J. Lippencott-Schwartz, *Cell biology*, Saunders / Elsevier, Philadelphia, Pa. u.a., 2nd edn., 2008.
- 2 J. D. Watson and F. H. CRICK, Molecular structure of nucleic acids; a structure for deoxyribose nucleic acid, *Nature*, 1953, **171**, 737–738.
- 3 N. C. Seeman, Nucleic acid junctions and lattices, *Journal of theoretical biology*, 1982, **99**, 237–247.
- 4 P. W. K. Rothmund, Folding DNA to create nanoscale shapes and patterns, *Nature*, 2006, **440**, 297–302.
- 5 A. Keller and V. Linko, Challenges and Perspectives of DNA Nanostructures in Biomedicine, *Angewandte Chemie (International ed. in English)*, 2020, **59**, 15818–15833.
- 6 D. M. Smith and A. Keller, DNA Nanostructures in the Fight Against Infectious Diseases, *Advanced nanobiomed research*, 2021, **1**, 2000049.
- 7 W. Engelen and H. Dietz, Advancing Biophysics Using DNA Origami, *Annual review of biophysics*, 2021, **50**, 469–492.
- 8 C. Pang, B. R. Aryal, D. R. Ranasinghe, T. R. Westover, A. E. F. Ehlert, J. N. Harb, R. C. Davis and A. T. Woolley, Bottom-Up Fabrication of DNA-Templated Electronic Nanomaterials and Their Characterization, *Nanomaterials*, 2021, **11**, 1655.
- 9 S. Julin, A. Keller and V. Linko, Dynamics of DNA Origami Lattices, *Bioconjugate chemistry*, 2023, **34**, 18–29.
- 10 V. Linko and A. Keller, Stability of DNA Origami Nanostructures in Physiological Media: The Role of Molecular Interactions, *Small (Weinheim an der Bergstrasse, Germany)*, 2023, **19**, e2301935.
- 11 S. Ramakrishnan, H. Ijäs, V. Linko and A. Keller, Structural stability of DNA origami nanostructures under application-specific conditions, *Computational and structural biotechnology journal*, 2018, **16**, 342–349.

- 12 S. Manuguri, M.-K. Nguyen, J. Loo, A. K. Natarajan and A. Kuzyk, Advancing the Utility of DNA Origami Technique through Enhanced Stability of DNA-Origami-Based Assemblies, *Bioconjugate chemistry*, 2023, **34**, 6–17.
- 13 Y. Chen, P. Wang, Y. Liu, T. Liu, Y. Xu, S. Zhu, J. Zhu, K. Ye, G. Huang and H. Dannong, Stability and recovery of DNA origami structure with cation concentration, *Nanotechnology*, 2018, **29**, 35102.
- 14 J. A. L. Roodhuizen, P. J. T. M. Hendrikx, P. A. J. Hilbers, T. F. A. de Greef and A. J. Markvoort, Counterion-Dependent Mechanisms of DNA Origami Nanostructure Stabilization Revealed by Atomistic Molecular Simulation, *ACS nano*, 2019, **13**, 10798–10809.
- 15 H. Kim, S. P. Surwade, A. Powell, C. O'Donnell and H. Liu, Stability of DNA Origami Nanostructure under Diverse Chemical Environments, *Chem. Mater.*, 2014, **26**, 5265–5273.
- 16 D. Wang, Z. Da, B. Zhang, M. A. Isbell, Y. Dong, X. Zhou, H. Liu, J. Y. Y. Heng and Z. Yang, Stability study of tubular DNA origami in the presence of protein crystallisation buffer, *RSC Adv.*, 2015, **5**, 58734–58737.
- 17 L. Sala, A. Zerolová, A. Rodriguez, D. Reimitz, M. Davidková, K. Ebel, I. Bald and J. Kočišek, Folding DNA into origami nanostructures enhances resistance to ionizing radiation, *Nanoscale*, 2021, **13**, 11197–11203.
- 18 B. Zhu, Y. Zhao, J. Dai, J. Wang, S. Xing, L. Guo, N. Chen, X. Qu, L. Li, J. Shen, J. Shi, J. Li and L. Wang, Preservation of DNA Nanostructure Carriers: Effects of Freeze-Thawing and Ionic Strength during Lyophilization and Storage, *ACS applied materials & interfaces*, 2017, **9**, 18434–18439.
- 19 Y. Xin, C. Kielar, S. Zhu, C. Sikeler, X. Xu, C. Möser, G. Grundmeier, T. Liedl, A. Heuer-Jungemann, D. M. Smith and A. Keller, Cryopreservation of DNA Origami Nanostructures, *Small (Weinheim an der Bergstrasse, Germany)*, 2020, **16**, e1905959.
- 20 M. A. Pillers and M. Lieberman, Thermal stability of DNA origami on mica, *Journal of Vacuum Science & Technology B, Nanotechnology and Microelectronics: Materials, Processing, Measurement, and Phenomena*, 2014, **32**, 40602.

- 21 J. Hahn, S. F. J. Wickham, W. M. Shih and S. D. Perrault, Addressing the instability of DNA nanostructures in tissue culture, *ACS nano*, 2014, **8**, 8765–8775.
- 22 C. Kielar, Y. Xin, B. Shen, M. A. Kostiainen, G. Grundmeier, V. Linko and A. Keller, On the Stability of DNA Origami Nanostructures in Low-Magnesium Buffers, *Angewandte Chemie (International ed. in English)*, 2018, **57**, 9470–9474.
- 23 S. Ramakrishnan, B. Shen, M. A. Kostiainen, G. Grundmeier, A. Keller and V. Linko, Real-Time Observation of Superstructure-Dependent DNA Origami Digestion by DNase I Using High-Speed Atomic Force Microscopy, *Chembiochem : a European journal of chemical biology*, 2019, **20**, 2818–2823.
- 24 Y. Xin, P. Piskunen, A. Suma, C. Li, H. Ijäs, S. Ojasalo, I. Seitz, M. A. Kostiainen, G. Grundmeier, V. Linko and A. Keller, Environment-Dependent Stability and Mechanical Properties of DNA Origami Six-Helix Bundles with Different Crossover Spacings, *Small (Weinheim an der Bergstrasse, Germany)*, 2022, **18**, e2107393.
- 25 S. Ramakrishnan, G. Krainer, G. Grundmeier, M. Schlierf and A. Keller, Structural stability of DNA origami nanostructures in the presence of chaotropic agents, *Nanoscale*, 2016, **8**, 10398–10405.
- 26 S. Ramakrishnan, G. Krainer, G. Grundmeier, M. Schlierf and A. Keller, Cation-Induced Stabilization and Denaturation of DNA Origami Nanostructures in Urea and Guanidinium Chloride, *Small (Weinheim an der Bergstrasse, Germany)*, 2017, **13**. DOI: 10.1002/sml.201702100.
- 27 B. Shen, V. Linko, K. Tapio, S. Pikker, T. Lemma, A. Gopinath, K. V. Gothelf, M. A. Kostiainen and J. J. Toppari, Plasmonic nanostructures through DNA-assisted lithography, *Science advances*, 2018, **4**, eaap8978.
- 28 H. Ijäs, B. Shen, A. Heuer-Jungemann, A. Keller, M. A. Kostiainen, T. Liedl, J. A. Ihalainen and V. Linko, Unraveling the interaction between doxorubicin and DNA origami nanostructures for customizable chemotherapeutic drug release, *Nucleic Acids Res.*, 2021, **49**, 3048–3062.
- 29 H. Bui, C. Onodera, C. Kidwell, Y. Tan, E. Graugnard, W. Kuang, J. Lee, W. B. Knowlton, B. Yurke and W. L. Hughes, Programmable periodicity of quantum dot arrays with DNA origami nanotubes, *Nano Lett.*, 2010, **10**, 3367–3372.

- 30 H. Lodish, *Molecular cell biology*, Freeman, New York, 5th edn., 2004.
- 31 F. H. C. Crick and J. D. Watson, The complementary structure of deoxyribonucleic acid, *Proc. R. Soc. Lond. A*, 1954, **223**, 80–96.
- 32 A. Travers and G. Muskhelishvili, DNA structure and function, *The FEBS journal*, 2015, **282**, 2279–2295.
- 33 A. Rich and S. Zhang, Timeline: Z-DNA: the long road to biological function, *Nature reviews. Genetics*, 2003, **4**, 566–572.
- 34 N. C. Seeman and H. F. Sleiman, DNA nanotechnology, *Nat Rev Mater*, 2018, **3**. DOI: 10.1038/natrevmats.2017.68.
- 35 N. C. Seeman and P. S. Lukeman, Nucleic Acid Nanostructures: Bottom-Up Control of Geometry on the Nanoscale, *Reports on progress in physics. Physical Society (Great Britain)*, 2005, **68**, 237–270.
- 36 S. Dey, C. Fan, K. V. Gothelf, J. Li, C. Lin, L. Liu, N. Liu, M. A. D. Nijenhuis, B. Saccà, F. C. Simmel, H. Yan and P. Zhan, DNA origami, *Nat. Rev. Methods Primers*, 2021, **1**. DOI: 10.1038/s43586-020-00009-8.
- 37 S. M. Douglas, H. Dietz, T. Liedl, B. Högberg, F. Graf and W. M. Shih, Self-assembly of DNA into nanoscale three-dimensional shapes, *Nature*, 2009, **459**, 414–418.
- 38 T. G. Martin and H. Dietz, Magnesium-free self-assembly of multi-layer DNA objects, *Nature communications*, 2012, **3**, 1103.
- 39 Y. Ke, J. Sharma, M. Liu, K. Jahn, Y. Liu and H. Yan, Scaffolded DNA origami of a DNA tetrahedron molecular container, *Nano letters*, 2009, **9**, 2445–2447.
- 40 E. Benson, A. Mohammed, J. Gardell, S. Masich, E. Czeizler, P. Orponen and B. Högberg, DNA rendering of polyhedral meshes at the nanoscale, *Nature*, 2015, **523**, 441–444.
- 41 T. Zhang, C. Hartl, K. Frank, A. Heuer-Jungemann, S. Fischer, P. C. Nickels, B. Nickel and T. Liedl, 3D DNA Origami Crystals, *Advanced materials (Deerfield Beach, Fla.)*, 2018, **30**, e1800273.
- 42 H. Auvinen, H. Zhang, Nonappa, A. Kopilow, E. H. Niemelä, S. Nummelin, A. Correia, H. A. Santos, V. Linko and M. A. Kostianen, Protein Coating of DNA Nanostructures for

- Enhanced Stability and Immunocompatibility, *Advanced healthcare materials*, 2017, **6**.
DOI: 10.1002/adhm.201700692.
- 43 S. Ramakrishnan, L. Schärffen, K. Hunold, S. Fricke, G. Grundmeier, M. Schlierf, A. Keller and G. Krainer, Enhancing the stability of DNA origami nanostructures: staple strand redesign versus enzymatic ligation, *Nanoscale*, 2019, **11**, 16270–16276.
- 44 M.-K. Nguyen, V. H. Nguyen, A. K. Natarajan, Y. Huang, J. Ryssy, B. Shen and A. Kuzyk, Ultrathin Silica Coating of DNA Origami Nanostructures, *Chem. Mater.*, 2020, **32**, 6657–6665.
- 45 Y. Chen, P. Wang, Y. Xu, X. Li, Y. Zhu, Y. Zhang, J. Zhu, G. Huang and D. He, Different Stability of DNA Origami Nanostructure between on Interface and in Bulk Solution, *ACS applied bio materials*, 2018, **1**, 1424–1429.
- 46 F. Hofmeister, Zur Lehre von der Wirkung der Salze, *Archiv f. experiment. Pathol. u. Pharmakol*, 1888, **24**, 247–260.
- 47 W. Kunz, J. Henle and B. W. Ninham, ‘Zur Lehre von der Wirkung der Salze’ (about the science of the effect of salts): Franz Hofmeister's historical papers, *Current Opinion in Colloid & Interface Science*, 2004, **9**, 19–37.
- 48 Y. Zhang and P. S. Cremer, Interactions between macromolecules and ions: The Hofmeister series, *Current opinion in chemical biology*, 2006, **10**, 658–663.
- 49 S. Moelbert, B. Normand and P. de Los Rios, Kosmotropes and chaotropes: modelling preferential exclusion, binding and aggregate stability, *Biophysical chemistry*, 2004, **112**, 45–57.
- 50 P. H. von Hippel and K. Y. Wong, Neutral Salts: The Generality of Their Effects on the Stability of Macromolecular Conformations, *Science (New York, N.Y.)*, 1964, **145**, 577–580.
- 51 Y. Zhang, S. Furyk, D. E. Bergbreiter and P. S. Cremer, Specific ion effects on the water solubility of macromolecules: PNIPAM and the Hofmeister series, *Journal of the American Chemical Society*, 2005, **127**, 14505–14510.

- 52 C. E. Dempsey, P. E. Mason and P. Jungwirth, Complex ion effects on polypeptide conformational stability: chloride and sulfate salts of guanidinium and tetrapropylammonium, *Journal of the American Chemical Society*, 2011, **133**, 7300–7303.
- 53 J. Heyda, H. I. Okur, J. Hladílková, K. B. Rembert, W. Hunn, T. Yang, J. Dzubiella, P. Jungwirth and P. S. Cremer, Guanidinium can both Cause and Prevent the Hydrophobic Collapse of Biomacromolecules, *Journal of the American Chemical Society*, 2017, **139**, 863–870.
- 54 Y. Zhang and P. S. Cremer, The inverse and direct Hofmeister series for lysozyme, *Proceedings of the National Academy of Sciences of the United States of America*, 2009, **106**, 15249–15253.
- 55 J. Paterová, K. B. Rembert, J. Heyda, Y. Kurra, H. I. Okur, W. R. Liu, C. Hilty, P. S. Cremer and P. Jungwirth, Reversal of the Hofmeister series: specific ion effects on peptides, *The journal of physical chemistry. B*, 2013, **117**, 8150–8158.
- 56 N. Schwierz, D. Horinek and R. R. Netz, Anionic and cationic Hofmeister effects on hydrophobic and hydrophilic surfaces, *Langmuir : the ACS journal of surfaces and colloids*, 2013, **29**, 2602–2614.
- 57 L. S. Taylor, P. York, A. C. Williams, H. G. Edwards, V. Mehta, G. S. Jackson, I. G. Badcoe and A. R. Clarke, Sucrose reduces the efficiency of protein denaturation by a chaotropic agent, *Biochimica et biophysica acta*, 1995, **1253**, 39–46.
- 58 J. L. Proc, M. A. Kuzyk, D. B. Hardie, J. Yang, D. S. Smith, A. M. Jackson, C. E. Parker and C. H. Borchers, A quantitative study of the effects of chaotropic agents, surfactants, and solvents on the digestion efficiency of human plasma proteins by trypsin, *Journal of proteome research*, 2010, **9**, 5422–5437.
- 59 H. Kim, J. U. Lee, S. Kim, S. Song and S. J. Sim, A Nanoplasmonic Biosensor for Ultrasensitive Detection of Alzheimer's Disease Biomarker Using a Chaotropic Agent, *ACS sensors*, 2019, **4**, 595–602.
- 60 X. Piao, V. Yadav, E. Wang, W. Chang, L. Tau, B. E. Lindenmuth and S. X. Wang, Double-stranded RNA reduction by chaotropic agents during in vitro transcription of messenger RNA, *Molecular therapy. Nucleic acids*, 2022, **29**, 618–624.

- 61 D. D. Bowtell, Rapid isolation of eukaryotic DNA, *Analytical biochemistry*, 1987, **162**, 463–465.
- 62 H. K. Nguyen, O. Fournier, U. Asseline, D. Dupret and N. T. Thuong, Smoothing of the thermal stability of DNA duplexes by using modified nucleosides and chaotropic agents, *Nucleic Acids Res.*, 1999, **27**, 1492–1498.
- 63 R. Jungmann, T. Liedl, T. L. Sobey, W. Shih and F. C. Simmel, Isothermal assembly of DNA origami structures using denaturing agents, *J. Am. Chem. Soc.*, 2008, **130**, 10062–10063.
- 64 Z. Zhang, J. Song, F. Besenbacher, M. Dong and K. V. Gothelf, Self-assembly of DNA origami and single-stranded tile structures at room temperature, *Angew. Chem. Int. Ed. Engl.*, 2013, **52**, 9219–9223.
- 65 B. Högberg, T. Liedl and W. M. Shih, Folding DNA origami from a double-stranded source of scaffold, *J. Am. Chem. Soc.*, 2009, **131**, 9154–9155.
- 66 P. C. Nickels, Y. Ke, R. Jungmann, D. M. Smith, M. Leichsenring, W. M. Shih, T. Liedl and B. Högberg, DNA origami structures directly assembled from intact bacteriophages, *Small*, 2014, **10**, 1765–1769.
- 67 P. E. Mason, G. W. Neilson, J. E. Enderby, M.-L. Saboungi, C. E. Dempsey, A. D. MacKerell and J. W. Brady, The structure of aqueous guanidinium chloride solutions, *Journal of the American Chemical Society*, 2004, **126**, 11462–11470.
- 68 P. E. Mason, C. E. Dempsey, L. Vrbka, J. Heyda, J. W. Brady and P. Jungwirth, Specificity of ion-protein interactions: complementary and competitive effects of tetrapropylammonium, guanidinium, sulfate, and chloride ions, *The journal of physical chemistry. B*, 2009, **113**, 3227–3234.
- 69 S. Sarkar and P. C. Singh, Alteration of the groove width of DNA induced by the multimodal hydrogen bonding of denaturants with DNA bases in its grooves affects their stability, *Biochimica et biophysica acta. General subjects*, 2020, **1864**, 129498.
- 70 S. Sarkar and P. C. Singh, Sequence specific hydrogen bond of DNA with denaturants affects its stability: Spectroscopic and simulation studies, *Biochimica et biophysica acta. General subjects*, 2021, **1865**, 129735.

- 71 B. Ding, D. Mukherjee, J. Chen and F. Gai, Do guanidinium and tetrapropylammonium ions specifically interact with aromatic amino acid side chains?, *Proceedings of the National Academy of Sciences of the United States of America*, 2017, **114**, 1003–1008.
- 72 Q. Fan, Z. He, J. Xiong and J. Chao, Smart Drug Delivery Systems Based on DNA Nanotechnology, *ChemPlusChem*, 2022, **87**, e202100548.
- 73 X. Shen, Q. Jiang, J. Wang, L. Dai, G. Zou, Z.-G. Wang, W.-Q. Chen, W. Jiang and B. Ding, Visualization of the intracellular location and stability of DNA origami with a label-free fluorescent probe, *Chemical communications (Cambridge, England)*, 2012, **48**, 11301–11303.
- 74 S. Ghosal, S. Bag and S. Bhowmik, Unravelling the Drug Encapsulation Ability of Functional DNA Origami Nanostructures: Current Understanding and Future Prospects on Targeted Drug Delivery, *Polymers*, 2023, **15**. DOI: 10.3390/polym15081850.
- 75 Z. Ge, Q. Li and C. Fan, Framework Nucleic Acids for Cell Imaging and Therapy, *Chem. Res. Chin. Univ.*, 2020, **36**, 1–9.
- 76 C. Angell, S. Xie, L. Zhang and Y. Chen, DNA Nanotechnology for Precise Control over Drug Delivery and Gene Therapy, *Small*, 2016, **12**, 1117–1132.
- 77 V. Kumar, S. Palazzolo, S. Bayda, G. Corona, G. Toffoli and F. Rizzolio, DNA Nanotechnology for Cancer Therapy, *Theranostics*, 2016, **6**, 710–725.
- 78 A. Mukherjee and W. D. Sasikala, Drug-DNA intercalation: from discovery to the molecular mechanism, *Advances in protein chemistry and structural biology*, 2013, **92**, 1–62.
- 79 K. Mišković, M. Bujak, M. Baus Lončar and L. Glavaš-Obrovac, Antineoplastic DNA-binding compounds: intercalating and minor groove binding drugs, *Arhiv za higijenu rada i toksikologiju*, 2013, **64**, 593–602.
- 80 Q. Jiang, C. Song, J. Nangreave, X. Liu, L. Lin, D. Qiu, Z.-G. Wang, G. Zou, X. Liang, H. Yan and B. Ding, DNA origami as a carrier for circumvention of drug resistance, *J. Am. Chem. Soc.*, 2012, **134**, 13396–13403.
- 81 P. D. Halley, C. R. Lucas, E. M. McWilliams, M. J. Webber, R. A. Patton, C. Kural, D. M. Lucas, J. C. Byrd and C. E. Castro, Daunorubicin-Loaded DNA Origami Nanostructures

- Circumvent Drug-Resistance Mechanisms in a Leukemia Model, *Small*, 2016, **12**, 308–320.
- 82 P. L. Hamilton and D. P. Arya, Natural product DNA major groove binders, *Natural product reports*, 2012, **29**, 134–143.
- 83 A. Lauria, A. Montalbano, P. Barraja, G. Dattolo and A. M. Almerico, DNA minor groove binders: an overview on molecular modeling and QSAR approaches, *Current medicinal chemistry*, 2007, **14**, 2136–2160.
- 84 D. Wang, M. Liu, Y. Wu, Y. Zhao, Q. Wang, T. Weng, L. Wang, H. Liu, Y. Ren and J. Han, Self-assembled DNA nanotrains for targeted delivery of mithramycin dimers coordinated by different metal ions: Effect of binding affinity on drug loading, release and cytotoxicity, *J. Mol. Liq.*, 2021, **339**, 116722.
- 85 H. Jeon, H. Nam and J. B. Lee, Sustained Release of Minor-Groove-Binding Antibiotic Netropsin from Calcium-Coated Groove-Rich DNA Particles, *Pharmaceutics*, 2019, **11**. DOI: 10.3390/pharmaceutics11080387.
- 86 F. Kollmann, S. Ramakrishnan, B. Shen, G. Grundmeier, M. A. Kostianen, V. Linko and A. Keller, Superstructure-Dependent Loading of DNA Origami Nanostructures with a Groove-Binding Drug, *ACS Omega*, 2018, **3**, 9441–9448.
- 87 S. Obuobi, V. Mayandi, N. A. M. Nor, B. J. Lee, R. Lakshminarayanan and P. L. R. Ee, Nucleic acid peptide nanogels for the treatment of bacterial keratitis, *Nanoscale*, 2020, **12**, 17411–17425.
- 88 S. Obuobi, K. Julin, E. G. A. Fredheim, M. Johannessen and N. Škalko-Basnet, Liposomal delivery of antibiotic loaded nucleic acid nanogels with enhanced drug loading and synergistic anti-inflammatory activity against *S. aureus* intracellular infections, *J. Control. Release*, 2020, **324**, 620–632.
- 89 C. Carvalho, R. X. Santos, S. Cardoso, S. Correia, P. J. Oliveira, M. S. Santos and P. I. Moreira, Doxorubicin: the good, the bad and the ugly effect, *Current medicinal chemistry*, 2009, **16**, 3267–3285.
- 90 X. Huang, N. T. Blum, J. Lin, J. Shi, C. Zhang and P. Huang, Chemotherapeutic drug-DNA hybrid nanostructures for anti-tumor therapy, *Materials horizons*, 2021, **8**, 78–101.

- 91 M. L. Kopka, C. Yoon, D. Goodsell, P. Pjura and R. E. Dickerson, The molecular origin of DNA-drug specificity in netropsin and distamycin, *Proceedings of the National Academy of Sciences of the United States of America*, 1985, **82**, 1376–1380.
- 92 C. Bailly and J. B. Chaires, Sequence-specific DNA minor groove binders. Design and synthesis of netropsin and distamycin analogues, *Bioconjugate chemistry*, 1998, **9**, 513–538.
- 93 E. M. Tuite and J. M. Kelly, Photochemical interactions of methylene blue and analogues with DNA and other biological substrates, *Journal of photochemistry and photobiology. B, Biology*, 1993, **21**, 103–124.
- 94 C. OhUigin, D. J. McConnell, J. M. Kelly and W. J. van der Putten, Methylene blue photosensitised strand cleavage of DNA: effects of dye binding and oxygen, *Nucleic Acids Res.*, 1987, **15**, 7411–7427.
- 95 D. P. Levine, Vancomycin: A history, *Clinical infectious diseases*, 2006, **42**, 5-12.
- 96 G. Binnig, C. F. Quate and C. Gerber, Atomic force microscope, *Physical review letters*, 1986, **56**, 930–933.
- 97 D. P. Allison, N. P. Mortensen, C. J. Sullivan and M. J. Doktycz, Atomic force microscopy of biological samples, *Wiley interdisciplinary reviews. Nanomedicine and nanobiotechnology*, 2010, **2**, 618–634.
- 98 N. Jalili and K. Laxminarayana, A review of atomic force microscopy imaging systems: application to molecular metrology and biological sciences, *Mechatronics*, 2004, **14**, 907–945.
- 99 D. J. Billingsley, W. A. Bonass, N. Crampton, J. Kirkham and N. H. Thomson, Single-molecule studies of DNA transcription using atomic force microscopy, *Physical biology*, 2012, **9**, 21001.
- 100 Y. Martin, C. C. Williams and H. K. Wickramasinghe, Atomic force microscope–force mapping and profiling on a sub 100-Å scale, *Journal of Applied Physics*, 1987, **61**, 4723–4729.

- 101 Q. Zhong, D. Inness, K. Kjoller and V. B. Elings, Fractured polymer/silica fiber surface studied by tapping mode atomic force microscopy, *Surface Science*, 1993, **290**, L688-L692.
- 102 R. García, Dynamic atomic force microscopy methods, *Surface Science Reports*, 2002, **47**, 197–301.
- 103 J. Adamcik, A. Berquand and R. Mezzenga, Single-step direct measurement of amyloid fibrils stiffness by peak force quantitative nanomechanical atomic force microscopy, *Applied Physics Letters*, 2011, **98**. DOI: 10.1063/1.3589369.
- 104 S. Hu, L. Mininni, Y. Hu, N. Erina, J. Kindt and C. Su, in *Metrology, Inspection, and Process Control for Microlithography XXVI*, ed. A. Starikov, SPIE, 2012, 83241O.
- 105 P. Trtik, J. Kaufmann and U. Volz, On the use of peak-force tapping atomic force microscopy for quantification of the local elastic modulus in hardened cement paste, *Cement and Concrete Research*, 2012, **42**, 215–221.
- 106 K. Xu, W. Sun, Y. Shao, F. Wei, X. Zhang, W. Wang and P. Li, Recent development of PeakForce Tapping mode atomic force microscopy and its applications on nanoscience, *Nanotechnology Reviews*, 2018, **7**, 605–621.
- 107 A. Dazzi, R. Prazeres, F. Glotin and J. M. Ortega, Local infrared microspectroscopy with subwavelength spatial resolution with an atomic force microscope tip used as a photothermal sensor, *Optics letters*, 2005, **30**, 2388–2390.
- 108 A. Dazzi and C. B. Prater, AFM-IR: Technology and Applications in Nanoscale Infrared Spectroscopy and Chemical Imaging, *Chemical reviews*, 2017, **117**, 5146–5173.
- 109 A. C. V D Dos Santos, N. Hondl, V. Ramos-Garcia, J. Kuligowski, B. Lendl and G. Ramer, AFM-IR for Nanoscale Chemical Characterization in Life Sciences: Recent Developments and Future Directions, *ACS Meas. Sci. Au*, 2023, **3**, 301–314.
- 110 J. J. Schwartz, D. S. Jakob and A. Centrone, A guide to nanoscale IR spectroscopy: resonance enhanced transduction in contact and tapping mode AFM-IR, *Chemical Society reviews*, 2022, **51**, 5248–5267.

- 111 Le Wang, H. Wang, M. Wagner, Y. Yan, D. S. Jakob and X. G. Xu, Nanoscale simultaneous chemical and mechanical imaging via peak force infrared microscopy, *Science advances*, 2017, **3**, e1700255.
- 112 Le Wang, H. Wang and X. G. Xu, Principle and applications of peak force infrared microscopy, *Chemical Society reviews*, 2022, **51**, 5268–5286.
- 113 S. Weiss, Fluorescence spectroscopy of single biomolecules, *Science (New York, N.Y.)*, 1999, **283**, 1676–1683.
- 114 B. Schuler, E. A. Lipman and W. A. Eaton, Probing the free-energy surface for protein folding with single-molecule fluorescence spectroscopy, *Nature*, 2002, **419**, 743–747.
- 115 B. Schuler, Single-molecule fluorescence spectroscopy of protein folding, *Chemphyschem : a European journal of chemical physics and physical chemistry*, 2005, **6**, 1206–1220.
- 116 J. R. Lakowicz, *Principles of fluorescence spectroscopy*, Springer, New York, NY, 3rd edn., 2006.
- 117 J. W. Lichtman and J.-A. Conchello, Fluorescence microscopy, *Nature methods*, 2005, **2**, 910–919.
- 118 C. Li and Y. Yue, Fluorescence spectroscopy of graphene quantum dots: temperature effect at different excitation wavelengths, *Nanotechnology*, 2014, **25**, 435703.
- 119 M. J. Sanderson, I. Smith, I. Parker and M. D. Bootman, Fluorescence microscopy, *Cold Spring Harbor protocols*, 2014, **2014**, pdb.top071795.
- 120 E. A. Jares-Erijman and T. M. Jovin, FRET imaging, *Nature biotechnology*, 2003, **21**, 1387–1395.
- 121 R. Roy, S. Hohng and T. Ha, A practical guide to single-molecule FRET, *Nature methods*, 2008, **5**, 507–516.
- 122 E.-C. Wamhoff, J. L. Banal, W. P. Bricker, T. R. Shepherd, M. F. Parsons, R. Veneziano, M. B. Stone, H. Jun, X. Wang and M. Bathe, Programming Structured DNA Assemblies to Probe Biophysical Processes, *Annu. Rev. Biophys.*, 2019, **48**, 395–419.
- 123 C. Kielar, F. V. Reddavid, S. Tubbenhauer, M. Cui, X. Xu, G. Grundmeier, Y. Zhang and A. Keller, Pharmacophore Nanoarrays on DNA Origami Substrates as a Single-

- Molecule Assay for Fragment-Based Drug Discovery, *Angew. Chem. Int. Ed. Engl.*, 2018, **57**, 14873–14877.
- 124 J. Huang, A. Suma, M. Cui, G. Grundmeier, V. Carnevale, Y. Zhang, C. Kielar and A. Keller, Arranging Small Molecules with Subnanometer Precision on DNA Origami Substrates for the Single-Molecule Investigation of Protein–Ligand Interactions, *Small Struct.*, 2020, **1**, 2000038.
- 125 A. Schoenit, E. A. Cavalcanti-Adam and K. Göpfrich, Functionalization of Cellular Membranes with DNA Nanotechnology, *Trends Biotechnol.*, 2021, **39**, 1208–1220.
- 126 K. Göpfrich, I. Platzman and J. P. Spatz, Mastering Complexity: Towards Bottom-up Construction of Multifunctional Eukaryotic Synthetic Cells, *Trends Biotechnol.*, 2018, **36**, 938–951.
- 127 H. Bila, E. E. Kurisinkal and M. M. C. Bastings, Engineering a stable future for DNA-origami as a biomaterial, *Biomater. Sci.*, 2019, **7**, 532–541.
- 128 J. A. Schellman, Fifty years of solvent denaturation, *Biophys. Chem.*, 2002, **96**, 91–101.
- 129 G. A. Knappe, E.-C. Wamhoff, B. J. Read, D. J. Irvine and M. Bathe, In Situ Covalent Functionalization of DNA Origami Virus-like Particles, *ACS Nano*, 2021, **15**, 14316–14322.
- 130 I. Gállego, B. Manning, J. D. Prades, M. Mir, J. Samitier and R. Eritja, DNA-Origami-Driven Lithography for Patterning on Gold Surfaces with Sub-10 nm Resolution, *Advanced materials (Deerfield Beach, Fla.)*, 2017, **29**. DOI: 10.1002/adma.201603233.
- 131 M. Sajfutdinow, K. Uhlig, A. Prager, C. Schneider, B. Abel and D. M. Smith, Nanoscale patterning of self-assembled monolayer (SAM)-functionalised substrates with single molecule contact printing, *Nanoscale*, 2017, **9**, 15098–15106.
- 132 R. Mancinelli, A. Botti, F. Bruni, M. A. Ricci and A. K. Soper, Hydration of sodium, potassium, and chloride ions in solution and the concept of structure maker/breaker, *J. Phys. Chem. B*, 2007, **111**, 13570–13577.

- 133 E. Thormann, On understanding of the Hofmeister effect: how addition of salt alters the stability of temperature responsive polymers in aqueous solutions, *RSC Adv.*, 2012, **2**, 8297.
- 134 C. F. Anderson and M. T. Record, Salt-nucleic acid interactions, *Annu. Rev. Phys. Chem.*, 1995, **46**, 657–700.
- 135 Y. Bai, M. Greenfeld, K. J. Travers, V. B. Chu, J. Lipfert, S. Doniach and D. Herschlag, Quantitative and comprehensive decomposition of the ion atmosphere around nucleic acids, *J. Am. Chem. Soc.*, 2007, **129**, 14981–14988.
- 136 M. Hanke, D. Dornbusch, C. Hadlich, A. Rossberg, N. Hansen, G. Grundmeier, S. Tsushima, A. Keller and K. Fahmy, Anion-specific structure and stability of guanidinium-bound DNA origami, *Comput. Struct. Biotechnol. J.*, 2022, **20**, 2611–2623.
- 137 M. Hanke, N. Hansen, R. Chen, G. Grundmeier, K. Fahmy and A. Keller, Salting-Out of DNA Origami Nanostructures by Ammonium Sulfate, *Int. J. Mol. Sci.*, 2022, **23**, 2817.
- 138 W. Fang, M. Xie, X. Hou, X. Liu, X. Zuo, J. Chao, L. Wang, C. Fan, H. Liu and L. Wang, DNA Origami Radiometers for Measuring Ultraviolet Exposure, *J. Am. Chem. Soc.*, 2020, **142**, 8782–8789.
- 139 A. Ray, K. Liosi, S. N. Ramakrishna, N. D. Spencer, A. Kuzuya and Y. Yamakoshi, Single-Molecule AFM Study of DNA Damage by 1O₂ Generated from Photoexcited C60, *J. Phys. Chem. Lett.*, 2020, **11**, 7819–7826.
- 140 C. Kielar, Y. Xin, X. Xu, S. Zhu, N. Gorin, G. Grundmeier, C. Möser, D. M. Smith and A. Keller, Effect of Staple Age on DNA Origami Nanostructure Assembly and Stability, *Molecules*, 2019, **24**. DOI: 10.3390/molecules24142577.
- 141 P. H. von Hippel and K.-Y. Wong, On the Conformational Stability of Globular Proteins, *J. Biol. Chem.*, 1965, **240**, 3909–3923.
- 142 A. Stopar, L. Coral, S. Di Giacomo, A. F. Adedeji and M. Castronovo, Binary control of enzymatic cleavage of DNA origami by structural antideterminants, *Nucleic Acids Res.*, 2018, **46**, 995–1006.

- 143 A. Suma, A. Stopar, A. W. Nicholson, M. Castronovo and V. Carnevale, Global and local mechanical properties control endonuclease reactivity of a DNA origami nanostructure, *Nucleic Acids Res.*, 2020, **48**, 4672–4680.
- 144 A. Matković, B. Vasić, J. Pešić, J. Prinz, I. Bald, A. R. Milosavljević and R. Gajić, Enhanced structural stability of DNA origami nanostructures by graphene encapsulation, *New J. Phys.*, 2016, **18**, 25016.
- 145 Q. Mei, X. Wei, F. Su, Y. Liu, C. Youngbull, R. Johnson, S. Lindsay, H. Yan and D. Meldrum, Stability of DNA origami nanoarrays in cell lysate, *Nano Lett.*, 2011, **11**, 1477–1482.
- 146 Y. Xin, A. A. Zargariantabrizi, G. Grundmeier and A. Keller, Magnesium-Free Immobilization of DNA Origami Nanostructures at Mica Surfaces for Atomic Force Microscopy, *Molecules*, 2021, **26**. DOI: 10.3390/molecules26164798.
- 147 P. E. Mason, G. W. Neilson, C. E. Dempsey, A. C. Barnes and J. M. Cruickshank, The hydration structure of guanidinium and thiocyanate ions: implications for protein stability in aqueous solution, *Proc. Nat. Acad. Sci. U.S.A.*, 2003, **100**, 4557–4561.
- 148 L. Opherden, J. Oertel, A. Barkleit, K. Fahmy and A. Keller, Paramagnetic decoration of DNA origami nanostructures by Eu^{3+} coordination, *Langmuir*, 2014, **30**, 8152–8159.
- 149 D. Nečas and P. Klapetek, Gwyddion: an open-source software for SPM data analysis, *Open Physics*, 2012, **10**, 181–188.
- 150 M. Hanke, N. Hansen, E. Tomm, G. Grundmeier and A. Keller, Time-Dependent DNA Origami Denaturation by Guanidinium Chloride, Guanidinium Sulfate, and Guanidinium Thiocyanate, *Int. J. Mol. Sci.*, 2022, **23**, 8547.
- 151 A. Kubičková, T. Křížek, P. Coufal, E. Wernersson, J. Heyda and P. Jungwirth, Guanidinium Cations Pair with Positively Charged Arginine Side Chains in Water, *J. Phys. Chem. Lett.*, 2011, **2**, 1387–1389.
- 152 H. I. Okur, J. Hladílková, K. B. Rembert, Y. Cho, J. Heyda, J. Dzubiella, P. S. Cremer and P. Jungwirth, Beyond the Hofmeister Series: Ion-Specific Effects on Proteins and Their Biological Functions, *J. Phys. Chem. B*, 2017, **121**, 1997–2014.

- 153 J. Lybaert, B. Maes, K. Abbaspour Tehrani and K. de Wael, The electrochemistry of tetrapropylammonium perruthenate, its role in the oxidation of primary alcohols and its potential for electrochemical recycling, *Electrochim. Acta*, 2015, **182**, 693–698.
- 154 P. Patnaik, B. C. Tripathy, I. N. Bhattacharya, R. K. Paramguru and B. K. Mishra, Effect of Tetra Propyl Ammonium Bromide During Cobalt Electrodeposition from Acidic Sulfate Solutions, *Metall. Mater. Trans. B*, 2015, **46**, 1252–1256.
- 155 I. Kurmanbayeva, L. Rakhymbay, K. Korzhynbayeva, A. Adi, D. Batyrbekuly, A. Mentbayeva and Z. Bakenov, Tetrapropylammonium Hydroxide as a Zinc Dendrite Growth Suppressor for Rechargeable Aqueous Battery, *Front. Energy Res.*, 2020, **8**. DOI: 10.3389/fenrg.2020.599009.
- 156 J. M. Collins and K. S. Rogers, Melting point depression of DNA by tetraalkylammonium bromides, *Chem.-Biol. Interact.*, 1977, **19**, 197–203.
- 157 W. B. Melchior and P. H. von Hippel, Alteration of the relative stability of dA-dT and dG-dC base pairs in DNA, *Proc. Natl. Acad. Sci. U. S. A.*, 1973, **70**, 298–302.
- 158 M. Hanke, D. Dornbusch, E. Tomm, G. Grundmeier, K. Fahmy and A. Keller, Superstructure-dependent stability of DNA origami nanostructures in the presence of chaotropic denaturants, *Nanoscale*, 2023, **15**, 16590–16600.
- 159 I. Kanesaka and K. Mizuguchi, Vibrational study of hydrogen bonds and structure of tris(hydroxymethyl)aminomethane, *J. Raman Spectrosc.*, 1998, **29**, 813–817.
- 160 L. Zhu, X.-J. Zhang, L.-Y. Wang, J.-M. Zhou and S. Perrett, Relationship between stability of folding intermediates and amyloid formation for the yeast prion Ure2p: a quantitative analysis of the effects of pH and buffer system, *J. Mol. Biol.*, 2003, **328**, 235–254.
- 161 M. Hanke, G. Grundmeier and A. Keller, Direct visualization of the drug loading of single DNA origami nanostructures by AFM-IR nanospectroscopy, *Nanoscale*, 2022, **14**, 11552–11560.
- 162 A. Chopra, S. Krishnan and F. C. Simmel, Electrotransfection of Polyamine Folded DNA Origami Structures, *Nano Lett.*, 2016, **16**, 6683–6690.

- 163 A. Bednarz, S. M. Sønderskov, M. Dong and V. Birkedal, Ion-mediated control of structural integrity and reconfigurability of DNA nanostructures, *Nanoscale*, 2023, **15**, 1317–1326.
- 164 K. Hübner, M. Raab, J. Bohlen, J. Bauer and P. Tinnefeld, Salt-induced conformational switching of a flat rectangular DNA origami structure, *Nanoscale*, 2022, **14**, 7898–7905.
- 165 S. Fischer, C. Hartl, K. Frank, J. O. Rädler, T. Liedl and B. Nickel, Shape and Interhelical Spacing of DNA Origami Nanostructures Studied by Small-Angle X-ray Scattering, *Nano Lett.*, 2016, **16**, 4282–4287.
- 166 E. Benson, A. Mohammed, D. Rayneau-Kirkhope, A. Gådin, P. Orponen and B. Högberg, Effects of Design Choices on the Stiffness of Wireframe DNA Origami Structures, *ACS Nano*, 2018, **12**, 9291–9299.
- 167 D. Morzy, C. Tekin, V. Caroprese, R. Rubio-Sánchez, L. Di Michele and M. M. C. Bastings, Interplay of the mechanical and structural properties of DNA nanostructures determines their electrostatic interactions with lipid membranes, *Nanoscale*, 2023, **15**, 2849–2859.
- 168 Y. Sato, M. Endo, M. Morita, M. Takinoue, H. Sugiyama, S. Murata, S. M. Nomura and Y. Suzuki, Environment-Dependent Self-Assembly of DNA Origami Lattices on Phase-Separated Lipid Membranes, *Adv. Mater. Interfaces*, 2018, **5**, 1800437.
- 169 Y. Xin, S. Martinez Rivadeneira, G. Grundmeier, M. Castro and A. Keller, Self-assembly of highly ordered DNA origami lattices at solid-liquid interfaces by controlling cation binding and exchange, *Nano Res.*, 2020, **13**, 3142–3150.
- 170 C. Kielar, S. Ramakrishnan, S. Fricke, G. Grundmeier and A. Keller, Dynamics of DNA Origami Lattice Formation at Solid-Liquid Interfaces, *ACS Appl. Mater. Interfaces*, 2018, **10**, 44844–44853.
- 171 W. F. Dove and N. Davidson, Cation effects on the denaturation of DNA, *J. Mol. Biol.*, 1962, **5**, 467–478.
- 172 N. R. Markham and M. Zuker, DINAMelt web server for nucleic acid melting prediction, *Nucleic Acids Res.*, 2005, **33**, W577-81.

- 173 J. M. Majikes, J. A. Nash and T. H. LaBean, Competitive annealing of multiple DNA origami: formation of chimeric origami, *New J. Phys.*, 2016, **18**, 115001.
- 174 J.-P. J. Sobczak, T. G. Martin, T. Gerling and H. Dietz, Rapid folding of DNA into nanoscale shapes at constant temperature, *Science*, 2012, **338**, 1458–1461.
- 175 C. E. Castro, F. Kilchherr, D.-N. Kim, E. L. Shiao, T. Wauer, P. Wortmann, M. Bathe and H. Dietz, A primer to scaffolded DNA origami, *Nat. Methods.*, 2011, **8**, 221–229.
- 176 J. L. T. Wah, C. David, S. Rudiuk, D. Baigl and A. Estevez-Torres, Observing and Controlling the Folding Pathway of DNA Origami at the Nanoscale, *ACS Nano*, 2016, **10**, 1978–1987.
- 177 H. Zipper, H. Brunner, J. Bernhagen and F. Vitzthum, Investigations on DNA intercalation and surface binding by SYBR Green I, its structure determination and methodological implications, *Nucleic Acids Res.*, 2004, **32**, e103.
- 178 V. Linko, B. Shen, K. Tapio, J. J. Toppari, M. A. Kostianen and S. Tuukkanen, One-step large-scale deposition of salt-free DNA origami nanostructures, *Sci. Rep.*, 2015, **5**, 15634.
- 179 L. Nguyen, M. Döblinger, T. Liedl and A. Heuer-Jungemann, DNA-Origami-Templated Silica Growth by Sol-Gel Chemistry, *Angew. Chem. Int. Ed. Engl.*, 2019, **58**, 912–916.
- 180 H. Ijäs, I. Hakaste, B. Shen, M. A. Kostianen and V. Linko, Reconfigurable DNA Origami Nanocapsule for pH-Controlled Encapsulation and Display of Cargo, *ACS Nano*, 2019, **13**, 5959–5967.
- 181 J. I. Cutler, E. Auyeung and C. A. Mirkin, Spherical nucleic acids, *J. Am. Chem. Soc.*, 2012, **134**, 1376–1391.
- 182 M. Hanke, E. Tomm, G. Grundmeier and A. Keller, Effect of Ionic Strength on the Thermal Stability of DNA Origami Nanostructures, *Chembiochem : a European journal of chemical biology*, 2023, **24**, e202300338.
- 183 R. A. Dimitrov and M. Zuker, Prediction of hybridization and melting for double-stranded nucleic acids, *Biophys. J.*, 2004, **87**, 215–226.

- 184 I. Seitz, A. Shaukat, K. Nurmi, H. Ijäs, J. Hirvonen, H. A. Santos, M. A. Kostiainen and V. Linko, Prospective Cancer Therapies Using Stimuli-Responsive DNA Nanostructures, *Macromol. Biosci.*, 2021, **21**, e2100272.
- 185 Q. Sun, Y. Han, Y. Yang, J. M. de La Fuente, D. Cui and X. Wang, Application of DNA nanostructures in cancer therapy, *Appl. Mater. Today*, 2020, **21**, 100861.
- 186 B. Chen, L. Mei, Y. Wang and G. Guo, Advances in intelligent DNA nanomachines for targeted cancer therapy, *Drug Discov. Today*, 2021, **26**, 1018–1029.
- 187 Y. Wang, T.-J. Chen-Mayfield, Z. Li, M. H. Younis, W. Cai and Q. Hu, Harnessing DNA for immunotherapy: Cancer, infectious diseases, and beyond, *Adv. Funct. Mater.*, 2022, **32**, 2112273.
- 188 C. Y. Tseng, W. X. Wang, T. R. Douglas and L. Y. T. Chou, Engineering DNA Nanostructures to Manipulate Immune Receptor Signaling and Immune Cell Fates, *Adv. Healthcare Mater.*, 2022, **11**, e2101844.
- 189 I. Mela, P. P. Vallejo-Ramirez, S. Makarchuk, G. Christie, D. Bailey, R. M. Henderson, H. Sugiyama, M. Endo and C. F. Kaminski, DNA Nanostructures for Targeted Antimicrobial Delivery, *Angew. Chem. Int. Ed. Engl.*, 2020, **59**, 12698–12702.
- 190 H. Dong, G. Song, D. Ma, T. Wang, S. Jing, H. Yang, Y. Tao, Y. Tang, Y. Shi, Z. Dai, J.-M. Zhu, T. Liu, B. Wang, X. Leng, X. Shen, C. Zhu and Y. Zhao, Improved Antiviral Activity of Classical Swine Fever Virus-Targeted siRNA by Tetrahedral Framework Nucleic Acid-Enhanced Delivery, *ACS Appl. Mater. Interfaces*, 2021, **13**, 29416–29423.
- 191 Y. Du, Q. Jiang, N. Beziere, L. Song, Q. Zhang, D. Peng, C. Chi, X. Yang, H. Guo, G. Diot, V. Ntziachristos, B. Ding and J. Tian, DNA-Nanostructure-Gold-Nanorod Hybrids for Enhanced In Vivo Optoacoustic Imaging and Photothermal Therapy, *Adv. Mater.*, 2016, **28**, 10000–10007.
- 192 A. Lacroix and H. F. Sleiman, DNA Nanostructures: Current Challenges and Opportunities for Cellular Delivery, *ACS nano*, 2021, **15**, 3631–3645.
- 193 M. I. Setyawati, R. V. Kutty, C. Y. Tay, X. Yuan, J. Xie and D. T. Leong, Novel theranostic DNA nanoscaffolds for the simultaneous detection and killing of *Escherichia coli* and *Staphylococcus aureus*, *ACS Appl. Mater. Interfaces*, 2014, **6**, 21822–21831.

- 194 Y.-X. Zhao, A. Shaw, X. Zeng, E. Benson, A. M. Nyström and B. Högberg, DNA origami delivery system for cancer therapy with tunable release properties, *ACS Nano*, 2012, **6**, 8684–8691.
- 195 X. Xie, X. Shao, W. Ma, D. Zhao, S. Shi, Q. Li and Y. Lin, Overcoming drug-resistant lung cancer by paclitaxel loaded tetrahedral DNA nanostructures, *Nanoscale*, 2018, **10**, 5457–5465.
- 196 Y. Xu, S. Huang, Y. Ma and H. Ding, Loading of DOX into a tetrahedral DNA nanostructure: the corner does matter, *Nanoscale Adv.*, 2022, **4**, 754–760.
- 197 H. L. Miller, S. Contera, A. J. M. Wollman, A. Hirst, K. E. Dunn, S. Schröter, D. O'Connell and M. C. Leake, Biophysical characterisation of DNA origami nanostructures reveals inaccessibility to intercalation binding sites, *Nanotechnology*, 2020, **31**, 235605.
- 198 J. Mathurin, A. Deniset-Besseau, D. Bazin, E. Dartois, M. Wagner and A. Dazzi, Photothermal AFM-IR spectroscopy and imaging: Status, challenges, and trends, *J. Appl. Phys.*, 2022, **131**, 10901.
- 199 J. P. Tardivo, A. Del Giglio, C. S. de Oliveira, D. S. Gabrielli, H. C. Junqueira, D. B. Tada, D. Severino, R. de Fátima Turchiello and M. S. Baptista, Methylene blue in photodynamic therapy: From basic mechanisms to clinical applications, *Photodiagn. Photodyn. Ther.*, 2005, **2**, 175–191.
- 200 S. Rizevsky, K. Zhaliyazka, T. Dou, M. Matveyenka and D. Kurouski, Characterization of Substrates and Surface-Enhancement in Atomic Force Microscopy Infrared Analysis of Amyloid Aggregates, *J. Phys. Chem. C*, 2022, **126**, 4157–4162.
- 201 K. Brassat, S. Ramakrishnan, J. Bürger, M. Hanke, M. Doostdar, J. K. N. Lindner, G. Grundmeier and A. Keller, On the Adsorption of DNA Origami Nanostructures in Nanohole Arrays, *Langmuir*, 2018, **34**, 14757–14765.
- 202 M. Hegner, P. Wagner and G. Semenza, Ultralarge atomically flat template-stripped Au surfaces for scanning probe microscopy, *Surf. Sci.*, 1993, **291**, 39–46.
- 203 M. L. S. Mello and B. C. Vidal, Changes in the infrared microspectroscopic characteristics of DNA caused by cationic elements, different base richness and single-stranded form, *PLoS One*, 2012, **7**, e43169.

- 204 O. V. Ovchinnikov, A. V. Evtukhova, T. S. Kondratenko, M. S. Smirnov, V. Y. Khokhlov and O. V. Erina, Manifestation of intermolecular interactions in FTIR spectra of methylene blue molecules, *Vib. Spectrosc.*, 2016, **86**, 181–189.
- 205 J. Li, F. Zhao, J. Zhao and B. Zeng, Adsorptive and stripping behavior of methylene blue at gold electrodes in the presence of cationic gemini surfactants, *Electrochim. Acta*, 2005, **51**, 297–303.
- 206 V. Žutić, V. Svetličić, J. Clavilier and J. Chevalet, Supramolecular phenomena in organic redox films at electrodes, *J. Electroanal. Chem. Interfacial Electrochem.*, 1987, **219**, 183–195.
- 207 S. Nafisi, A. A. Saboury, N. Keramat, J.-F. Neault and H.-A. Tajmir-Riahi, Stability and structural features of DNA intercalation with ethidium bromide, acridine orange and methylene blue, *J. Mol. Struct.*, 2007, **827**, 35–43.
- 208 R. R. Naujok, R. V. Duevel and R. M. Corn, Fluorescence and Fourier Transform surface-enhanced Raman scattering measurements of methylene blue adsorbed onto a sulfur-modified gold electrode, *Langmuir*, 1993, **9**, 1771–1774.
- 209 C. T. Cesco, A. J. M. Valente and A. T. Paulino, Methylene Blue Release from Chitosan/Pectin and Chitosan/DNA Blend Hydrogels, *Pharmaceutics*, 2021, **13**. DOI: 10.3390/pharmaceutics13060842.
- 210 N. G. Tognalli, A. Fainstein, C. Vericat, M. E. Vela and R. C. Salvarezza, Exploring three-dimensional nanosystems with Raman spectroscopy: methylene blue adsorbed on thiol and sulfur monolayers on gold, *J. Phys. Chem. B*, 2006, **110**, 354–360.
- 211 C. Ciraci, F. Vidal-Codina, D. Yoo, J. Peraire, S.-H. Oh and D. R. Smith, Impact of Surface Roughness in Nanogap Plasmonic Systems, *ACS Photonics*, 2020, **7**, 908–913.
- 212 R. Bansal, R. Singh and K. Kaur, Quantitative analysis of doxorubicin hydrochloride and arterolane maleate by mid IR spectroscopy using transmission and reflectance modes, *BMC Chem.*, 2021, **15**, 27.
- 213 J. Liu, L. Song, S. Liu, Q. Jiang, Q. Liu, N. Li, Z.-G. Wang and B. Ding, A DNA-Based Nanocarrier for Efficient Gene Delivery and Combined Cancer Therapy, *Nano Lett.*, 2018, **18**, 3328–3334.

- 214 C. Wiraja, Y. Zhu, D. C. S. Lio, D. C. Yeo, M. Xie, W. Fang, Q. Li, M. Zheng, M. van Steensel, L. Wang, C. Fan and C. Xu, Framework nucleic acids as programmable carrier for transdermal drug delivery, *Nat. Commun.*, 2019, **10**, 1147.
- 215 Q. Zhang, Q. Jiang, N. Li, L. Dai, Q. Liu, L. Song, J. Wang, Y. Li, J. Tian, B. Ding and Y. Du, DNA origami as an in vivo drug delivery vehicle for cancer therapy, *ACS nano*, 2014, **8**, 6633–6643.
- 216 D. Agudelo, P. Bourassa, G. Bérubé and H.-A. Tajmir-Riahi, Intercalation of antitumor drug doxorubicin and its analogue by DNA duplex: structural features and biological implications, *Int. J. Biol. Macromol.*, 2014, **66**, 144–150.
- 217 E. Stahl, T. G. Martin, F. Praetorius and H. Dietz, Facile and scalable preparation of pure and dense DNA origami solutions, *Angew. Chem. Int. Ed. Engl.*, 2014, **53**, 12735–12740.
- 218 B. Mosebach, F. M. Bayer, C.-C. Fels, M. Voigt, B. Oezkaya, A. Pomorska, B. Torun, A. Keller and G. Grundmeier, Adsorption and adhesion studies of PdSn-nanoparticles on protonated amine and carboxylic acid-terminated surfaces, *Surf. Interface Anal.*, 2016, **48**, 1017–1025.

Declaration of Authorship

I hereby declare that I have authored this thesis independently, that I have not used other than the declared sources/resources, and that I have explicitly marked all material which has been quoted either literally or by content from the used sources.

Paderborn, 2023

Acknowledgement

I would like to thank Prof. Dr. Guido Grundmeier for giving me the opportunity to work in this great group for so many years.

I would like to thank my thesis advisor Dr. Adrian Keller for so many years of great teamwork and guidance through my PhD. The way you lead and teach your group is very pleasant. I wish you all the best for the future.

I would like to thank Prof. Dr. Veikko Linko for being my second reviewer of my thesis.

I would like to thank Prof. Dr. Karim Fahmy and his working group for the fruitful collaboration we had together.

I would like to especially thank my working group for the time during the work and the awesome free times we spent together. We are not only colleagues, we are more than that.

I would like to thank my family for their support.